Leibniz-Institut für Astrophysik Potsdam

Ground-based transmission spectroscopy of three inflated Hot Jupiter exoplanets

Dissertation
zur Erlangung des akademischen Grades
“doctor rerum naturalium”
(Dr. rer. nat.)
in der Wissenschaftsdisziplin Astrophysik

eingereicht an der
Mathematisch-Naturwissenschaftlichen Fakultät
der Universität Potsdam

von
Matthias Mallonn

Potsdam, den 30. September 2014

Abstract

The characterization of exoplanets is a young and rapidly expanding field in astronomy. It includes a method called *transmission spectroscopy* that searches for planetary spectral fingerprints in the light received from the host star during the event of a transit. This techniques allows for conclusions on the atmospheric composition at the terminator region, the boundary between the day and night side of the planet. Observationally a big challenge, first attempts in the community have been successful in the detection of several absorption features in the optical wavelength range. These are for example a Rayleigh-scattering slope and absorption by sodium and potassium. However, other objects show a featureless spectrum indicative for a cloud or haze layer of condensates masking the probable atmospheric layers.

In this work, we performed transmission spectroscopy by spectrophotometry of three Hot Jupiter exoplanets. When we began the work on this thesis, optical transmission spectra have been available for two exoplanets. Our main goal was to advance the current sample of probed objects to learn by comparative exoplanetology whether certain absorption features are common. We selected the targets HAT-P-12b, HAT-P-19b and HAT-P-32b, for which the detection of atmospheric signatures is feasible with current ground-based instrumentation. In addition, we monitored the host stars of all three objects photometrically to correct for influences of stellar activity if necessary.

The obtained measurements of the three objects all favor featureless spectra. A variety of atmospheric compositions can explain the lack of a wavelength dependent absorption. But the broad trend of featureless spectra in planets of a wide range of temperatures, found in this work and in similar studies recently published in the literature, favors an explanation based on the presence of condensates even at very low concentrations in the atmospheres of these close-in gas giants. This result points towards the general conclusion that the capability of transmission spectroscopy to determine the atmospheric composition is limited, at least for measurements at low spectral resolution.

In addition, we refined the transit parameters and ephemerides of HAT-P-12b and HAT-P-19b. Our monitoring campaigns allowed for the detection of the stellar rotation period of HAT-P-19 and a refined age estimate. For HAT-P-12 and HAT-P-32, we derived upper limits on their potential variability. The calculated upper limits of systematic effects of starspots on the derived transmission spectra were found to be negligible for all three targets.

Finally, we discussed the observational challenges in the characterization of exoplanet atmospheres, the importance of correlated noise in the measurements and formulated suggestions on how to improve on the robustness of results in future work.

Zusammenfassung

Die Charakterisierung von Exoplaneten ist ein junger und sich schnell entwickelnder Zweig der Astronomie. Eine ihrer Methoden ist die Transmissionsspektroskopie, welche nach spektralen Abdrücken der Planetenatmosphäre im Licht des Muttersterns sucht. Diese Technik macht sich den Umstand zunutze, dass Planeten mit niedriger Bahnneigung einmal pro Umlauf vor ihrem Stern vorbeiziehen, wobei das Sternlicht Teile der Planetenatmosphäre durchläuft. Durch die Auswertung solcher Transitbeobachtungen lässt sich auf die chemische Zusammensetzung der Planetenatmosphäre schließen. Trotz der großen Herausforderung an die benötigte Messgenauigkeit konnten bereits erste vielversprechende Ergebnisse erzielt werden und Entdeckungen wie zum Beispiel Rayleighstreuung und Absorption von Natrium und Kalium vermeldet werden. Andere Beobachtungen zeigten aber auch gänzlich flache Spektren ohne wellenlängenabhängige Absorption, welche auf eine Wolkenschicht oder Dunst in den Atmosphären hinweisen.

In dieser Arbeit führten wir Transmissionsspektroskopie für drei extrasolare Planeten aus der Klasse der heißen Jupiter-artigen Gasriesen durch. Als wir mit unserer Studie begannen, waren erst zwei derartige Objekte erfolgreich auf ihr Spektrum im optischen Wellenlängenbereich untersucht worden. Unser Ziel war es, diese Anzahl zu erhöhen, um herauszufinden, welche spektralen Eigenschaften typisch für diese Exoplaneten sind. Wir wählten drei Objekte aus, für welche die zu erwartenden Messgenauigkeiten ausreichend für signifikante Ergebnisse sind: HAT-P-12b, HAT-P-19b und HAT-P-32b. Zusätzlich unternahmen wir Langzeitbeobachtungen der Muttersterne dieser Planeten, um die Transitbeobachtungen auf einen möglichen Einfluss von Sternaktivität zu korrigieren.

Die erzielten Messungen der drei Planeten deuten alle auf Spektren ohne Absorptionslinien hin. Das Fehlen dieser Linien kann durch verschiedene Möglichkeiten zustande kommen, welche für die einzelnen Objekte individuell variieren können. Der Umstand jedoch, dass allen Objekten diese Linien fehlen und dass ähnliche Ergebnisse für weitere Objekte kürzlich in der Literatur publiziert wurden, deutet darauf hin, dass für einen bedeutenden Teil der Exoplaneten die Atmosphären nicht transparent, sondern durch kondensiertes Material optisch undurchlässig sind. Sollte sich dieses Ergebnis durch zukünftige Beobachtungen bestätigen, bedeutet es, dass die Transmissionsspektroskopie als Beobachtungstechnik nur sehr begrenzt für die Charakterisierung dieser Planetenatmosphären nützlich ist. Nur Beobachtungen hochaufgelöster Spektroskopie könnten dann verwertbare Informationen liefern.

Weiterhin konnten wir in unserer Arbeit die Transitparameter und Ephemeriden von HAT-P-12b und HAT-P-19b genauer vermessen als es vorherigen Analysen möglich war. Durch unsere Langzeitbeobachtungen konnte die Rotationsperiode von HAT-P-19 bestimmt, sowie das Alter dieses Muttersterns neu berechnet werden. Ebenso leiteten wir Höchstwerte für eine mögliche Veränderlichkeit von HAT-P-12 und HAT-P-32 ab. Wir errechneten die Korrekturen der Transitparameter auf die Einflüsse von Sternaktivität und stellten fest, dass diese die Messergebnisse nicht wesentlich beeinflussen.

Unsere Arbeit erlaubte tiefe Einblicke in die technischen Herausforderungen, welche diese Wissenschaft an die Sternbeobachtungen stellt. Wir diskutierten den Einfluss von systematischen Fehlern in den Messreihen und erarbeiteten Empfehlungen, wie die Messergebnisse weiter verbessert werden können.

Contents

Abstract i

Zusammenfassung iii

List of Figures vii

List of Tables ix

1 Introduction 1
- 1.1 History of the search for extrasolar planets . . . 1
- 1.2 Sensitivity of exoplanet search programs . . . 2
- 1.3 Characterization of extrasolar planets . . . 6
- 1.4 Open questions and our contribution . . . 8
- 1.5 Structure of the thesis . . . 9
- 1.6 Remarks on the authorship . . . 9

2 Methodology 11
- 2.1 Target selection and accepted observing proposals . . . 12
- 2.2 Transit light curve fit and error analyses . . . 15
- 2.3 Stellar limb darkening . . . 18
- 2.4 Correction for starspots . . . 20
- 2.5 Model predictions of theoretical spectra . . . 23
- 2.6 Literature review of observations . . . 24
  - 2.6.1 HD209458b . . . 25
  - 2.6.2 HD189733b . . . 26
  - 2.6.3 GJ1214b . . . 27
  - 2.6.4 Other Hot Jupiters . . . 28

3 Transmission spectroscopy of HAT-P-19b 31
- 3.1 Introduction . . . 31
- 3.2 Observations and data reduction . . . 31
  - 3.2.1 Spectroscopic GTC OSIRIS observation . . . 31
  - 3.2.2 Photometric STELLA WiFSIP monitoring . . . 34
- 3.3 Analysis and results . . . 36
  - 3.3.1 Detrending and white light curve analysis . . . 36
  - 3.3.2 Error estimation of the transit parameters . . . 39
  - 3.3.3 Ephemeris . . . 39
  - 3.3.4 Transit depth as a function of wavelength . . . 41
  - 3.3.5 Photometric variability of HAT-P-19 . . . 44
  - 3.3.6 Correction for starspots . . . 45
- 3.4 Discussion . . . 47
  - 3.4.1 Discrepancy in the transit parameter . . . 47
  - 3.4.2 The transmission spectrum . . . 47
  - 3.4.3 The long term photometric variability . . . 50

4 Broad-band spectrophotometry of HAT-P-12b 53
4.1 Introduction . . . 53
4.2 Observations . . . 54
4.2.1 The transit observations . . . 55
4.2.2 Observations of the monitoring program . . . 58
4.3 Data reduction . . . 58
4.3.1 Transit data . . . 58
4.3.2 Monitoring data . . . 60
4.4 Re-analysis of literature data . . . 61
4.5 The potential starspot crossing event on March 28, 2014 . . . 61
4.6 Transit modeling and results . . . 63
4.6.1 Detrending of the light curves . . . 63
4.6.2 Global transit parameters . . . 64
4.6.3 Ephemeris and O-C diagram . . . 69
4.6.4 Planetary radius over wavelength . . . 71
4.7 Results of the monitoring program and starspot correction . . . 75
4.8 Discussion . . . 76
4.8.1 Transmission spectrum . . . 76
4.8.2 Other broad-band spectrophotometry studies . . . 79
4.8.3 Periodicity in the monitoring light curves . . . 80

5 Transmission spectroscopy of HAT-P-12b and HAT-P-32b 83
5.1 Introduction . . . 83
5.2 Transit observations with MODS . . . 84
5.3 Data reduction of the MODS data . . . 85
5.4 Monitoring of HAT-P-32 . . . 86
5.5 HAT-P-32: Correction for starspots and M dwarf companion . . . 90
5.6 Analysis of transit light curves . . . 91
5.7 Discussion . . . 93
5.7.1 Transmission spectrum of HAT-P-12b . . . 93
5.7.2 Transmission spectrum of HAT-P-32b . . . 94

6 Conclusions and Outlook 101

Bibliography 105

List of Figures

1.1 The planets of the Solar System in comparison to detected exoplanets . . . 4
1.2 Schematic illustration of a transiting exoplanet with primary eclipse and secondary eclipse . . . 6

2.1 Illustration of exoplanet transmission spectroscopy . . . 12
2.2 The potential transit signal Δ_{depth} over the apparent magnitude . . . 14
2.3 Illustration of a transit light curve showing the geometric quantities T, τ and δ . . . 15
2.4 Two examples for the estimation of the β factor . . . 18
2.5 Illustration of the effect of limb darkening on the transit light curves . . . 19
2.6 Illustration of the effect of stellar spots on exoplanet transit light curves . . 21
2.7 Theoretical transmission spectra for Hot Jupiter exoplanets of from 500 to 2500 K . . . 24
2.8 Observed transmission spectrum of HD209458b . . . 26
2.9 Observed transmission spectrum of HD189733b . . . 27
2.10 Observed transmission spectrum of GJ1214b . . . 29

3.1 Evolution of observational parameters over the time series of the HAT-P-19b GTC transit . . . 33
3.2 Spectra of HAT-P-19 and the comparison star of the first exposure . . . 35
3.3 White light curve of the GTC transit of HAT-P-19b . . . 37
3.4 Transit timing residuals versus the linear ephemeris of HAT-P-19b . . . 42
3.5 Chromatic set of transit light curves of HAT-P-19b . . . 43
3.6 Transmission spectrum of HAT-P-19b . . . 44
3.7 Monitoring light curves of HAT-P-19 in V and I . . . 45
3.8 Lomb Scargle periodogram for the monitoring light curves . . . 46
3.9 Transmission spectrum in comparison to a theoretical spectrum . . . 48
3.10 Transmission spectrum of HAT-P-19b when the detrending of the light curve is linked to adjacent wavelength channels . . . 50

4.1 Light curves of the new transit observations of HAT-P-12b . . . 59
4.2 Light curve of the March 28, 2014 with asymmetric feature. . . . 62
4.3 Light curves of the epoch of the potential starspot crossing event . . . 63
4.4 Example of the long term trend in differential magnitude probably caused by atmospheric effects . . . 64
4.5 Simulation to investigate the underestimation of transit parameter uncertainties when the detrending uncertainty is ignored . . . 67
4.6 Transit timing residuals versus the linear ephemeris of HAT-P-12b . . . 71
4.7 Lomb-Scargle periodogram of the transit timing residuals of HAT-P-12b . . 72
4.8 The planet star radius ratio k for the indiviual transit light curves of HAT-P-12b . . . 74
4.9 Monitoring light curves of HAT-P-12 in V and I . . . 76
4.10 Broad-band transmission spectrum of HAT-P-12b . . . 78

4.11 Transmission spectrum of HAT-P-12b combining the measurements of this work with the HST measurements of Line et al. (2013) 78
4.12 Comparison of the achieved uncertainty of the transit depth given in the literature of broad-band transmission spectroscopy 79

5.1 Spectra of HAT-P-12 and the comparison star of a single exposure 86
5.2 Spectra of HAT-P-32 and the two comparison stars of a single exposure . . 87
5.3 Simultaneously taken transit light curves of HAT-P-12b extracted from the MODS spectra 88
5.4 Simultaneously taken transit light curves of HAT-P-32b extracted from the MODS spectra 89
5.5 Monitoring light curves of HAT-P-32 in Johnson B and Sloan r' 90
5.6 Lomb-Scargle periodogram of the monitoring light curves of HAT-P-32 . . . 91
5.7 Third light contribution of the M dwarf near-by star to the integrated light of HAT-P-32 92
5.8 Transmission spectrum of HAT-P-12b derived from the MODS transit measurement 93
5.9 Transmission spectrum of HAT-P-32b derived from the MODS transit measurement 94

List of Tables

1.1 Number of confirmed planets per detection method 2

2.1 Comparison of the potential transmission signal Δ_{depth} per scale height of selected exoplanets and Jupiter and Earth. 13

3.1 Dependence of the derived transit parameters of HAT-P-19b on the model function used for detrending 37
3.2 Transit fit parameter of the white light curve. 39
3.3 Characteristics of the extracted transit light curves. 40
3.3 continued 41
3.4 Transit midtimes of HAT-P-19b and their residuals versus the linear ephemeris 42

4.1 Overview about new transit observations of HAT-P-12b 57
4.2 Overview about published transit observations of HAT-P-12, which were re-analysed in this work 61
4.3 The derived transit parameters of this work in comparison to literature values for HAT-P-12b. 69
4.4 Observed transit times of HAT-P-12b 70
4.5 The derived planet-star radius ratio k per transit observation 73

5.1 Characteristics of the extracted transit light curves of HAT-P-12b. 97
5.1 continued 98
5.2 Characteristics of the extracted transit light curves of HAT-P-32b. 98

1 Introduction

1.1 History of the search for extrasolar planets

The origins of the question whether the Earth and life like ours is unique in the Universe go back to the roots of natural science itself. In the fourth century BC, the Greek philosopher Epicurus wrote in a letter to Herodotus: “There are infinite worlds both like and unlike this world of ours” and “that in all worlds there are living creatures and plants and other things we see in this world.” His point of view contradicted that of the philosophical school of Plato and Aristotle, who taught that the Earth was placed at the center of the universe and therefore must be unique. Aristotle’s geo-centric view was elaborated further by the philosopher Ptolemy, later known as the Ptolemaic System. Due to its good agreement with the teaching of the Roman Catholic Church about God and the place of man in the universe, the Ptolemaic System dominated astronomical thinking for more than 1500 years.

In the early 16th century, the Polish mathematician Nicolas Copernicus developed a theory in which the Sun was positioned at the center of the universe. About one century later, this so-called Copernican System was observationally supported by the Italian mathematician Galileo Galilei, who discovered that Venus and Mercury exhibit phases like the Moon. This observation was inconsistent with the Ptolemaic System, but in agreement with the Copernican System. While Galilei bowed down to the pressure of the Catholic church and recanted, another Italian philosopher refused to recant and was sentenced to be burned at the stake: Giordano Bruno, the “patron saint of planet-finders” (Kasting 2010), wrote in his book *De L’infinito Universo E Mondi* (1584):

> “There are countless suns and countless earths all rotating round their suns in exactly the same way as the seven planets of our system. We see only the suns because they are the largest bodies and are luminous, but their planets remain invisible to us because they are smaller and non-luminous. The countless worlds in the universe are no worse and no less inhabited than our Earth.”

In his famous *Principia* from 1713, Isaac Newton speculated about the same possibility of planets around other stars:

> “And if the fixed stars are the centers of similar systems, they will all be constructed according to a similar design and subject to the dominion of *One*.”

One of the very first attempts to explain how extrasolar planets might be revealed by observational measurements came from Dionysius Lardner. In his book *Hand-Books of Natural Philosophy and Astronomy* (1858) he mentions planetary transits as one reason for periodic variability of stars. 80 years later, Belorizky (1938) describes how the detection of a 1% brightness drop caused by a transiting exo-Jupiter would be possible with a photoelectric cell, whereas the radial velocity shift caused by the stellar reflex motion and a direct photographic detection are still out of technical reach. The increased signal strength, and therefore enhanced detectability, of close-in giant planets was discussed by Struve (1952). The existence of these close-in planets, 50 years later called *Hot Jupiters*, could only be speculated about at this time.

The huge observational challenge to detect an extrasolar planet repeatedly led to discoveries, which could not be confirmed and turned out to be spurious. A famous example is the long debate about one Jupiter-sized companion around Barnards star (van de Kamp 1963, 1969). Just a few years later, van de Kamp (1982) announced the presence of a second gas giant. Soon, follow-up studies appeared, but they were not able to confirm the discovery (Gatewood & Eichhorn 1973; Hershey 1973) and attributed the "signal" to adjustments and modifications of the telescopes optical system. A state-of-the-art investigation described the existence of the van-de-Kamp planets as "extremely unlikely" (Choi et al. 2013).

The title of "the first exoplanet detection" is often given to the work of Wolszczan & Frail (1992), who found two planets belonging to the pulsar PSR 1257+12. However, in retrospect there is another work that also desired this title: Campbell et al. (1988) studied γ Cephei and found a radial velocity signal interpretable as a planetary object of ~ 1.7 $\mathrm{M_{Jupiter}}$ with a ~ 2.7 years period. However, the authors were cautious about claiming a detection due to their rather large measurement uncertainties. Fifteen years later, the exoplanet could be confirmed by Hatzes et al. (2003) to have a minimum mass $M \sin i = 1.70 \pm 0.13$ $\mathrm{M_{Jupiter}}$ and an orbital period of 2.48 ± 0.01 years.

The first exoplanet detection around a Sun-like star was achieved by Mayor & Queloz (1995), who discovered a giant planet in a close-in orbit around the Sun-like star 51 Peg. Since then the numbers of detected planets has exploded, rising to 1828 confirmed planets (exoplanet.eu, Schneider et al. 2011). Table 1.1 gives an overview about the numbers of detections made with the most important detection methods. Recently, the transit method has replaced the radial velocity method as the most successful one in terms of number of detections (Rowe et al. 2014).

detection method		number
confirmed planets		1828
Transit		1156
	satellite	990
	ground-based	166
Radial velocity		574
Imaging		51
Microlensing		32
Timing		15
additional candidates		3276

Table 1.1. Number of confirmed planets and exoplanet candidates (status September 29, 2014) taken from exoplanet.eu (Schneider et al. 2011) and the NASA exoplanet archive accessible at exoplanetarchive.ipac.caltech.edu.

1.2 Sensitivity of exoplanet search programs and occurrence rate

Almost 20 years have past since the discovery of Mayor & Queloz (1995) and the number of detected planets per year is still rising. What is the current sensitivity reached by the discovery programs? To illustrate the answer, we want to formulate the question a little bit differently: "What component of the Solar System would have been found when observed from the outside with current instrumentation?" Starting with the Transit method, the question is answered by looking at the distribution of Kepler candidates in the semi-major axis - radius diagram given in Figure 1.1. Kepler is a satellite mission which continuously monitored about 150 000 stars in the Cygnus star constellation for $\sim$3.5 years (Koch et al. 2010; Borucki et al. 2010). Frequently, lists of Kepler candidates were released (Borucki et al. 2011a,b; Batalha et al. 2013; Burke et al. 2014), which are expected to show a low false positive rate of below 10% (Morton & Johnson 2011). In the upper panel of Figure 1.1 we see that several exoplanet candidates have been found with parameters similar to Earth and Venus, while the majority of objects are larger than the Solar System's rocky planets and have shorter orbital periods. The record holder for the smallest (confirmed) planet size is Kepler-37b with a radius smaller than Mercury, $R = 0.303^{+0.053}_{-0.073}\,\mathrm{R}_\oplus$ (Barclay et al. 2013). Thus, a detection of a Mercury-, Venus- and Earth-like planet in the Kepler data is, in principle, possible, and just a matter of the photometric signal-to-noise ratio. However, the detection of a Mars-like exoplanet cannot be expected from the Kepler mission anymore: It ended after about 3.5 years of operation because of a satellite malfunction. Therefore, the general condition of at least three transit events for a firm detection could not be reached for Mars' orbital period of nearly two years. With its remaining technical capabilities, the Kepler spacecraft is still taking data, now called *K2* or *Second Light* mission. However, the telescope needs to change its pointing every $\sim$80 days and is therefore not sensitive to long-period exoplanets anymore (Howell et al. 2014).

The lower panel of Figure 1.1 illustrates that after more than two decades of data acquisition, the radial velocity (RV) surveys are filling the parameter space near Jupiter. Our heaviest Solar System planet causes a radial velocity reflex motion of the Sun of semi-amplitude $K \sim 12.7$ m/s over a period of $P_{\mathrm{Jupiter}} \sim 11.86$ yr. With the advent of time, the RV surveys were able to supply the needed RV accuracy over a length of many years to become sensitive to planets with similar $K - P$ values like HD220773b ($P \sim 10.2$ yr, $K = 20.0$ m/s, Robertson et al. 2012), HD154345b ($P \sim 9.2$ yr, $K = 14.0$ m/s, Wright et al. 2008) and HD134987c ($P \sim 13.7$ yr, $K = 9.3$ m/s, Jones et al. 2010). However, a planet like Saturn with $P \sim 30$ a and $K \sim 3$ m/s is not yet reachable.

Microlensing as a planet search technique probes regions further away from the host star than the transit and radial velocity method (Gould & Loeb 1992; Bennett & Rhie 1996). The most successful surveys in exoplanet detections are the Optical Gravitational Lensing Experiment (OGLE, Udalski et al. 1993) and the Microlensing Observations in Astrophysics (MOA, Bond et al. 2001). A statistical analysis of Cassan et al. (2012) describes their reached sensitivity to extend roughly from 0.5 AU to 10 AU for planetary orbits, and from 5 $\mathrm{M}_\oplus$ to 10 $\mathrm{M}_{\mathrm{Jupiter}}$. Hence, currently operating microlensing surveys could have found analogues to the two solar gas giants.

The technique of Direct Imaging did not find an analogue of any solar planet yet for the simple reason that the solar giant planets have already cooled down and are therefore too dim, compared to their host star, for any direct detection. Target stars for Direct Imaging surveys are mostly younger than 100 Myr (Chauvin et al. 2003; Biller et al. 2013b), the only directly imaged exoplanet around a main-sequence Sun-like star is GJ 504b (Kuzuhara et al. 2013). With its temperature of $\sim$ 500 K, mass of $\sim$ 4 $\mathrm{M}_{\mathrm{Jupiter}}$ and projected separation of $\sim$ 44 AU, it is still off the solar planets in parameter space. However, leaving the age aside, Direct Imaging surveys reach inner working angles and sensitivities approaching Jupiter and Saturn: Biller et al. (2013b) describes the limits of their survey to be 1–20 $\mathrm{M}_{\mathrm{Jupiter}}$ and 10–150 AU.

The Solar System contains more than the Sun and its planets. Do other stars also harbor asteroids, comets, Kuiper belt objects, etc.? Parts of this question were answered well before any extra-solar planet was found. In 1984, observations of the IRAS satellite revealed an infra-red excess around Vega, Formalhaut and beta Pic (Aumann et al. 1984; Aumann 1984). The authors concluded that the material responsible for the thermal emission "is a remnant of the cloud out of which α Lyr formed", a protoplanetary disk.

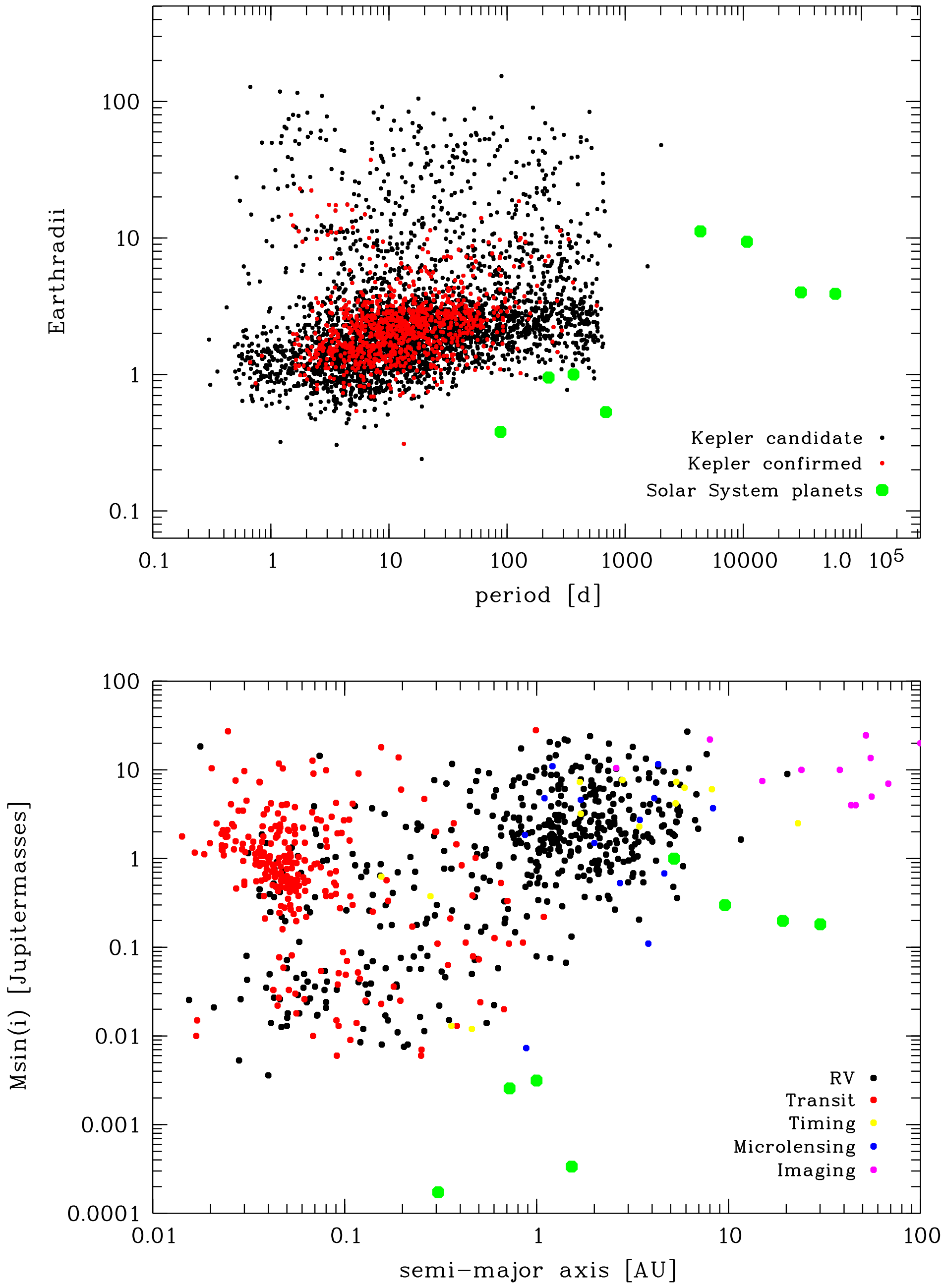

Fig. 1.1. The planets of the Solar System in comparison to the Kepler candidates (upper plot) and the confirmed planet detections (lower plot).

Shortly after, the disk of beta Pic could be imaged in the optical (Smith & Terrile 1984), some years later all three disk were imaged at sub-millimeter wavelengths (Holland et al. 1998). Because of the lack of gas in the disk and the age of Vega, Lagrange et al. (2000) concluded that here we do not see a planet system in its formation, instead the dust disk is produced continuously in a belt of planetesimals by collisions. Therefore, these disks are called debris disks and are similar in their nature to the solar Kuiper belt. The advent of new surveys with the Spitzer Space Telescope allowed for the discovery of hundreds of debris disk systems (Su et al. 2006; Hillenbrand et al. 2008; Trilling et al. 2008). The sensitivity reached by Spitzer is limited to fractional luminosities of $L_{\mathrm{dust}}/L_* > 10^{-5}$, i. e. more than 100 times the expected fractional luminosity of the Kuiper Belt in the Solar System of $\sim 10^{-7}$ (Jewitt et al. 2009). The ESA satellite Herschel refined these sensitivity limits to an average of $L_{\mathrm{dust}}/L_* \sim 10^{-6}$ for its debris disk surveys DEBRIS[1] (Matthews et al. 2014, in prep.) and DUNES[2] (Eiroa et al. 2013). It can be concluded that the Kuiper belt would not have been detected by the current instrumentations.

Warm debris disks as analogues to the Solar System's zodiacal dust cloud, so-called exozodiacal dust with temperatures of 120 to 200 K, have also been found, though in smaller numbers than the Kuiper-belt-analogues, the cold debris disks ($T < 100$ K) (Kennedy & Wyatt 2012; Cruz-Saenz de Miera et al. 2014; Patel et al. 2014). The achieved sensitivity levels of successful surveys using the WISE satellite are still more than 3 orders of magnitude above the fractional luminosity of the zodiacal dust emission in the Solar System. However, future generations of mid-IR interferometers like the Large Binocular Telescope Interferometer (LBTI, Hinz 2009) are predicted to approach the Solar System luminosity level to one order of magnitude (Kennedy & Wyatt 2013). Examples of systems with multiple dust belts and planets are the Sun, ϵ Eridani (Benedict et al. 2006; Backman et al. 2009) and HR8799 (Su et al. 2009; Marois et al. 2010).

The Solar System gas giants have large collections of moons, therefore it is reasonable to assume that exomoons are equally common. Despite multiple proposed detection techniques (e.g. Sartoretti & Schneider 1999; Kipping 2009; Heller 2014) and theoretical studies of exomoon habitability (e.g. Heller 2012; Heller & Barnes 2013), no definite exomoon detection could be accomplished yet.

The last decade of research in the field of exoplanets brought the conclusion, that planetary companions are a common feature of FGKM main sequence stars. Statistics of different detection techniques agree that the number of planets in the Milky Way is in the order of the number of stars or higher. A radial velocity study of Mayor et al. (2011) found about 75% occurrence rate for FGK stars, for M stars it is about 100% (Bonfils et al. 2013). The transit method revealed in average at least 0.87 planets per FGKM main-sequence star (Fressin et al. 2013). The statistical analysis of microlensing surveys yields about 1.6 planets per star (Cassan et al. 2012).

A closer look at these results reveals that the different techniques probe different regions in the planet parameter space. No study extrapolated the occurrence rate to masses or periods that they are not sensitive to. While the parameter space of the transit and the RV surveys overlap to some extent, there is just little overlap to the parameter space investigated by the Microlensing surveys. However, all the results have in common that smaller planets are more abundant than larger ones. Solar-type main sequence stars have ~ 0.52 Neptune-mass planets and ~ 0.62 planets with masses between Earth and Neptune per star in orbital distances between the orbit of Venus and Jupiter, while there are just ~ 0.17 planets of Saturn- and Jupiter-mass per star (Cassan et al. 2012). RV and transit studies agree that planets with masses of 2–10 $\mathrm{M}_\oplus$ or radii of 1.25–2 $\mathrm{R}_\oplus$, the so-called super-Earths, are the most abundant species also in short-period orbits regarding current detection limits (Howard et al. 2010; Mayor et al. 2011; Bonfils et al. 2013; Petigura et al. 2013a,b). Gas giants are less common in orbits inside the orbit of Mercury, their occurrence rate ranges from 3 to 14% in correlation to the mass of the host star (Johnson et al. 2010).

We conclude that the number of planets in the Milky Way is at least on the order of the number of stars. The planet to star number ratio in the Solar System is 8:1, however this pure number does not necessarily makes the Solar System something special in the Milky Way. The statistical analyses are so far just sensitive to either none (RV and transit statistics) or just two of our planets (Microlensing statistics). In the current view the Solar

---

[1] Disc Emission via a Bias-free Reconnaissance in the Infrared/Submillimeter

[2] DUst around NEarby Stars

System might deviate from the average in having two gas giants and no planet between the Earth and Neptune in mass.

1.3 Characterization of extrasolar planets

Once an exoplanet is found, we want to learn about its properties. Every detailed characterization starts with the parameters radius and mass. The planetary radius can currently just be derived for transiting planets. The mass, however, can be derived by several detection techniques like radial velocity, transit timing variation, microlensing or astrometry. Both parameters, radius and mass, yield the mean density of an exoplanet. In certain parameter ranges the mean density allows for the derivation of the planetary composition as it was done, for example in the case of Kepler-78b, the first Earth-sized exoplanet with an observationally established rocky composition (Pepe et al. 2013; Howard et al. 2013). In 2017, the European Space Agency will launch the CHaracterising ExOPlanets Satellite (CHEOPS) whose main goal is to refine the radius measurements of a large number of planets with known masses, to constrain their composition and learn about diversity in the exoplanet population (Broeg et al. 2013). However, there are regions in the mass-radius parameter space for which the mean density cannot yield unique composition solutions, a famous example is the super-Earth GJ1214b. Here, a variety of interior makeups would fit the size and mass measurements ranging from a terrestrial planet with an outgassed hydrogen-rich atmosphere to a small version of Neptune (Rogers & Seager 2010; Nettelmann et al. 2011, see Section 2.6 for details). This degeneracy can be broken by spectroscopy of the planetary atmospheres (Miller-Ricci & Fortney 2010; Bean et al. 2010). However, the direct spectroscopy in a rather classical meaning is hampered by the enormous brightness contrast between planet and host star and their small angular separation. It was was done successfully only in very few cases of directly imaged planets, where the planet and the stellar light contribution could be spatially separated (Chauvin et al. 2004; Barman et al. 2011; Oppenheimer et al. 2013).

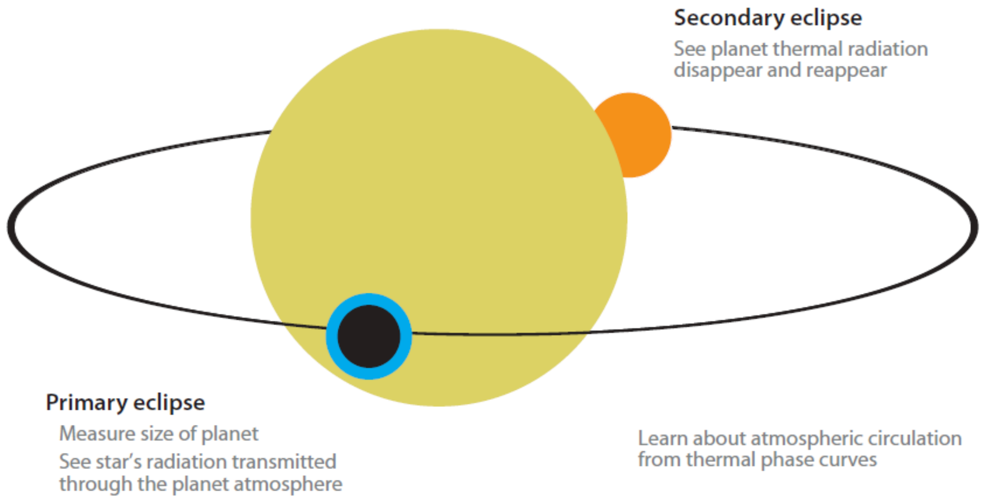

Fig. 1.2. Schematic illustration from Seager & Deming (2010) of a transiting exoplanet with primary eclipse and secondary eclipse and their potential follow-up measurements.

Currently, the major source of spectroscopic information for the exoplanets comes from the transiting objects. Once every orbit the planet moves in front of the host star from the perspective of the Earth observer and once it disappears behind (Figure 1.2). These events are called transit (or primary eclipse) and secondary eclipse. During a transit, a fraction of the starlight passes through the planetary atmosphere and becomes slightly modified by the planetary spectrum. During the secondary eclipse we see the star light alone, while shortly before and after the observer on Earth views the combined star-planet light. Knowing the luminosity of the host star, the depth of the eclipse is a direct measurement of the luminosity of the planet. It allows for the derivation of its reflectivity (albedo) at optical wavelengths. At near and mid-infrared wavelengths, the depth of the secondary eclipse reveals the thermal radiation coming from the planet itself which can be translated into the planet's brightness temperature.

The advent of the exoplanet characterization would not have been the same without the transiting Hot Jupiters. Their high temperature of 1000 to 2000 K or even higher and close stellar proximity (semi-major axis $\lesssim$ 0.05 AU, $P \lesssim 5$ days) combined with the observational potential of transits and secondary eclipses made them favorable for atmospheric detection and characterization (Seager & Sasselov 1998). At about the time when the first exoplanet transit had been observed (Henry et al. 2000; Charbonneau et al. 2000), first theoretical studies appeared on how to identify atomic and molecular features in exoplanet atmospheres using transit transmission spectra (Seager & Sasselov 2000). The dedicated ground-based transit search programs needed a few years to gain experience in false alarm rejections, but then the number of known transiting Hot Jupiters exploded due to for example TrES[3] (Alonso et al. 2004), SuperWASP[4] (Collier Cameron et al. 2007) and the HATNet project[5] (Bakos et al. 2007a).

The first measurement of a spectroscopic feature originating in a planetary atmosphere was done by Charbonneau et al. (2002), when they detected the sodium D line in HD209458b with the Hubble Space Telescope (HST). The first detection of light emitted by an extrasolar planet was achieved for HD209458b (Deming et al. 2005) and TrES-1b (Charbonneau et al. 2005) at 24 μm respectively 4.5 and 8.0 μm using the Spitzer Space Telescope.

Transmission and emission spectroscopy of Hot Jupiters already revealed spectroscopic atomic and molecular features of H, Na, K, H_2O, CO, and several more. The first decade of observational efforts provided a rich diversity of results: Na and K absorption features are present in some atmospheres, while they are absent in others. Some atmospheres show signs of Rayleigh-scattering, while others are indicative of dense cloud decks. Exoplanets also differ in their albedos, in the heat redistribution from the hot day side to the somewhat cooler night side (Hot Jupiters are tidally locked and possess a permanent day and night side) and in the existence and intensity of a temperature inversion. For very few planets, like HD209458b and HD189733b, very extensive datasets have been gathered over a wide range of wavelength with complementary transmission spectroscopy, emission spectroscopy and phase curves. The existing data allowed for abundance estimations of sodium and water, measurements of the temperature-pressure profile, measurements of wind speed and temperatures differences on the day and night side and much more. For the majority of the investigated targets, the atmospheric characterization relies on a limited number of data points in wavelength of limited signal-to-noise ratio. Therefore, most spectroscopic investigations concentrate on the classification of the planets in categories: Does the atmosphere show strong alkali absorption indicative for a clear atmosphere? Are there indications for TiO/VO absorption in the spectrum? Is the spectrum best approximated by a flat line indicating an opaque cloud deck? Is there a dominant Rayleigh slope detectable potentially caused by haze in the atmosphere?

---

[3] Trans-Atlantic Exoplanet Survey

[4] Wide Angle Search for Planets

[5] Hungarian Automated Telescope Network

An initial rough classification can already be done with only a few data points over wavelength. Examples are the investigation of temperature inversions for which the Spitzer Space Telescope broad band photometry channels at 3.6, 4.5, 5.8 and 8 μm have been used extensively (Machalek et al. 2008, 2009; Knutson et al. 2008, 2009; Todorov et al. 2010). When Spitzer run out of liquid helium, just the two shortest-wavelength modules of the IRAC camera remained operable, but these two points in wavelength at 3.6 and 4.5 μm still allowed for significant results on the presence of temperature inversions and heat redistribution in the exoplanets atmospheres (Todorov et al. 2012, 2013; Mahtani et al. 2013; Baskin et al. 2013). A similar approach was applied at optical wavelengths using just very few selected broad band channels to verify the presence of TiO absorption or Rayleigh scattering in the exoplanet atmospheres. Indeed, two filters can already provide meaningful results (Nascimbeni et al. 2013b; Bento et al. 2014).

1.4 Open questions and our contribution

The understanding of exoplanet atmospheres is still in its infancy. So far, we mainly know that exoplanet atmospheres are divers and many physical aspects play a role, for example energy sources from the planets interior, the stellar incident flux from the outside and energy redistribution from the hot day to the cooler night side including different types of dynamics in an atmosphere like winds and turbulent vertical mixing. How does photoionization changes the chemical abundance for such close-in planets, how does condensation act on it? Does the condensation of elements at the colder night side influence the abundance on the day side? If grains form by condensation, do they stay aloft or do they rain out?

Two complementary approaches to answer a few of such questions are currently taken in the exoplanet community: One is the detailed investigation of the most favorable targets like HD209458b and HD189733b for which high signal to noise observations are available from different observing techniques (see Section 2.6). The second approach is comparative exoplanetology, in which it is tried to invest a statistically meaningful number of exoplanets with similar observational settings to allow for comparisons and to reveal correlations among observed features and physical planetary or stellar properties.

If we look at recent literature on exoplanet spectroscopy (a comprehensive overview is given in Section 2.6), one feature is striking: The minority of exoplanets shows features as they are predicted by clear atmosphere models. For the vast majority either no features could have been detected or the features have been found with muted amplitudes. One interpretation is the presence of clouds or haze in the atmosphere making it opaque and not probable anymore. We know clouds from most of our Solar System planets and we know them from brown dwarfs (Biller et al. 2013a, and references therein), which possess temperature-pressure profiles in their atmospheres similar to Hot Jupiters. Therefore, the interpretation of clouds as the reason for the absence of expected spectral features seems plausible. However, the majority of Bond albedo[6] measurements found Hot Jupiters to be dark as coal (Cowan & Agol 2011; Esteves et al. 2013; Heng & Demory 2013), unambiguously indicating clear atmospheres as clouds would increase the albedo values. Is this contradiction real or maybe just caused by the investigation of different atmospheric regions (transmission spectroscopy probes the terminator, the bond albedo values were derived from measurements of the reflectivity of the day side)?

The presence of clouds or haze makes a characterization of an exoplanet atmosphere via transmission spectroscopy very hard: First, the observable features used for a charac-

---

[6] The Bond albedo is the fraction of power of the radiation incident on an astronomical body that is scattered back out into space.

terization are muted or totally diminished. And at second, the theoretical interpretation of observed spectra would be very limited, because cloud formation and its interaction with the abundance and temperature-pressure profile are barely included in the models. Depending on their thickness and opacities, clouds and hazes can cool or heat the upper atmosphere by their strong influence on the redistribution of insulation energy from the star (Heng et al. 2012).

We want to contribute to the question whether Hot Jupiters possess clouds at the probable altitudes by transmission spectroscopy of three different targets, HAT-P-19b, HAT-P-12b and HAT-P-32b. The first two targets have equilibrium temperatures of about 1000 K, a temperature regime for which cloud formation at pressure ranges probed by our observations is less likely (Brown 2001; Fortney et al. 2010). The third planet, HAT-P-32b, has a very different temperature of about 1800 K, allowing for comparisons with the cooler planets.

Next to this atmospheric questions, the exoplanet community still needs to learn how trustful their derived results are. Many achieved detections are at the $3\,\sigma$ level, but how reliable are the derived uncertainties? Can results be repeated by different groups and different instruments? If we feel confident with our measurements, what other mechanism can influence the result like host star variability due to for example magnetic activity or variability in the planetary atmosphere itself due to weather?

We want to contribute to the questions whether results can be repeated and how reliable are the derived results by the analysis of a high number of observations of a single planet, HAT-P-12b, and by the analysis of a new dataset of an object for which a comparable analysis was already presented in the literature, HAT-P-32b. We address the question about the influence of stellar activity on the derived results for all our northern targets by extensive photometric monitoring campaigns.

1.5 Structure of the thesis

This thesis is structured as follows: Chapter 2 gives details about the method of transmission spectroscopy in general, summarizes our target selection, explains how we fit the transit light curves and perform the correction for starspots. At the end, it reviews the predictions of atmospheric models and the current status of transmission spectroscopy in the literature. Chapter 3 presents the transmission spectroscopy of HAT-P-19b with the OSIRIS spectrograph at the Gran Telescopio de Canarias. Also the results of the HAT-P-19 monitoring are shown and discussed. Chapter 4 deals with the broad-band spectrophotometry of HAT-P-12b and the monitoring of its host star. In Chapter 5, we provide the transmission spectroscopy of HAT-P-12b and HAT-P-32b with the spectrograph MODS at the LBT together with the monitoring of HAT-P-12. In Chapter 6, we conclude and outline how we plan to continue with the observations of exoplanet atmospheres.

1.6 Remarks on the authorship

The analysis of HAT-P-19b presented in Chapter 3 is submitted for publication to the Journal *Astronomy & Astrophysics* with the author of this thesis being the first author on the manuscript. Co-authors are J. Weingrill, K.G. Strassmeier, I. Ribas, C. von Essen, T.A. Carroll, E. Herrero, T. Granzer, A. Claret and A. Schwope. J.W. was responsible for the age determination of HAT-P-19 by gyrochronology presented in Section 3.4.3, T.G. supplied technical support for STELLA, A.C. calculated the stellar limb darkening coefficients and A.S. provided ESO-MIDAS tools used to develop our longslit data reduction routines. I.R. was the P.I. of the observing proposal. J.W., K.G.S., C.v.E., T.A.C. and E.H. gave advice on the manuscript.

The analysis of HAT-P-12b presented in Chapter 4 is ready for submission to *Astronomy & Astrophysics*. Co-authors on the manuscript are V. Nascimbeni, J. Weingrill, C. von Essen, K.G. Strassmeier, G. Piotto, I. Pagano, G. Scandariato, Sz. Csizmadia, E. Herrero, P.V. Sada, A. Künstler, I. Bernt and T. Granzer. V.N., I.P. and E.H. were P.I. of observing proposals of data included here. C.E. gave advice on the TTV analysis. P.V.S. gave us the chance to re-analyze their transit data. A.K. provided the spectrum of HAT-P-12 of the SPECTRUM spectral synthesis code and gave many comments on the manuscript. I.B. was responsible for details of the imaging data reduction and T.G. supplied technical support with STELLA. J.W., C.v.E., K.G.S., G.P., G.S. and S.C. gave advice on the manuscript.

The analysis of HAT-P-12b and HAT-P-32b of Chapter 5 is not ready for submission and includes no contribution of co-authors.

2 Methodology of ground-based transit spectrophotometry

During a transit event, a planet moves across the visible hemisphere of its host star as seen from Earth. Monitoring this event photometrically, a light dimming of about 1% can be measured for a transit of a Jupiter-sized planet if the star is approximately of the size of the Sun. A Neptune-sized planet would cause a decrease of light of about 0.1%, and a planet of Earth size dims the stellar flux by $\sim 0.01\%$. The exoplanet might be surrounded by an atmosphere. For a rocky planet the atmosphere is clearly defined as the gas layer on top of the solid material, for a gas planet the atmosphere is typically defined as the region above the radiative-convective boundary. This atmosphere is translucent at its highest altitudes at low pressures of ~ 0.1–100 mbar. Absorption and scattering determines the planetary radius at which the condition of optical depth $\tau = 2/3$ is met, i. e. how big the observer measures the planet to be in relation to its host star. Therefore, it is the chemical composition that governs whether certain heights of the atmosphere are transparent or opaque at certain wavelengths. The effective size $R_{\text{eff}} = R_{\tau=2/3}$ of the exoplanet is dependent on wavelength and is highest at dominant absorption features. The effective planet size over wavelength is called the *transmission spectrum* of a planet. This concept is illustrated in Fig. 2.1.

Transmission spectroscopy probes the terminator region of a planet, i. e. the boundary region between the permanent day and night side. The stellar beam pointing at the observer is directed perpendicular to the radial direction of the planet. Hence, the relevant τ_{trans} is much larger than the radial τ_{radial} important for emission spectroscopy, which is the emission of the planet over wavelength measured at secondary eclipse. Therefore, emission spectroscopy probes deeper layers of the atmosphere at higher pressures, while the transmission spectrum is more sensitive to trace chemical species, an effect investigated in detail by Fortney (2005). The dependence of the effective planetary radius R_{eff} on wavelength can be expressed as

$$\frac{dR_{\text{eff}}}{d\ln\lambda} = H\frac{d\ln\sigma}{d\ln\lambda}\,, \tag{2.1}$$

where σ is the total species-weighted interaction cross-section and H is the atmospheric pressure scale height[1]. Note that, whereas emission spectra depend only upon absorption, transit spectra depend upon both scattering and absorption (Burrows 2013).

Transmission spectra are probes of the atmospheric scale heights H and the atmospheric abundances through σ (Equation 2.1). However, the dependence of R_{eff} on σ is logarithmic and therefore weak. The goal of current transmission spectroscopy projects is rather to detect molecular features than to analyze them quantitatively for their abundance.

Throughout this thesis we interpret the search for a wavelength dependent atmospheric absorption as the search for a wavelength-dependence of effective planetary radius and therefore of transit depth since we assume the stellar radius to be wavelength independent.

---

[1] The atmospheric pressure scale height, for the remainder just called "scale height", is the vertical distance by which the pressure changes by a factor of e.

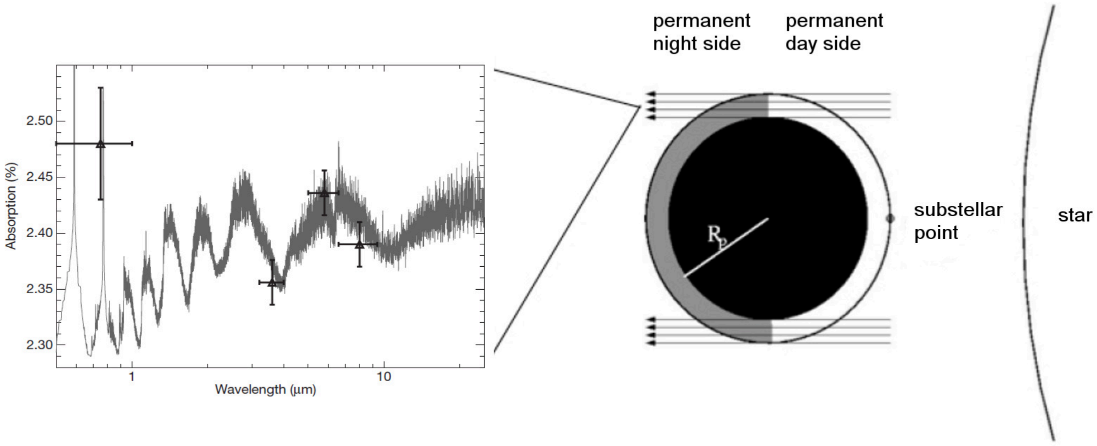

Fig. 2.1. Illustration of exoplanet transmission spectroscopy. During a planetary transit, a fraction of the star light crosses the atmosphere of the planet and is absorbed by the atmospheric elements. A plot of that extra absorption over wavelength is what we call a transmission spectrum of the exoplanet. Figure taken from Tinetti et al. (2007) and López-Morales (2011).

2.1 Target selection and accepted observing proposals

The amplitude of the absorption signal in transmission spectroscopy, i. e. the change in measured transit depth Δ_{depth} relates to the size of the probed atmospheric annulus compared to the stellar size:

$$\Delta_{\text{depth}} \sim \frac{R_p}{R_\star^2} H\,, \tag{2.2}$$

with the atmospheric pressure scale height H as

$$H = \frac{k\,T}{\mu\,g}\,. \tag{2.3}$$

Here, k is the Boltzman constant, T the mean atmospheric temperature, μ the mean molecular weight and g the surface acceleration due to gravity. We assume μ of a Hot Jupiter equals Jupiters value of 2.2 g/mol. Therefore, a low stellar radius, a high planetary temperature and radius and a low surface gravity will yield a higher transmission signal. The potential signal for a H_2-rich solar-metallicity atmosphere without a veiling haze/cloud layer amounts to 5–10 scale heights.

Most known transiting planets orbit solar type main-sequence stars. For these host stars of radii from about 0.8 to 1.5 $R_\odot$ just gas giant planets are able to produce transmission signals accessible by current instrumentations. In principle, the smaller the host star, the smaller the exoplanet could be for the same transmission signal. However, we still know just a few transiting planets around M stars, famous examples are GJ1214b (Charbonneau et al. 2009) and GJ3470b (Bonfils et al. 2012). The demand for smaller host stars to push the characterization of exoplanet to the super-Earth and Earth regime is well recognized in the community and transit surveys designed for M stars as the MEarth project (Berta et al. 2013) , the WFCAM Transit Survey (Kovács et al. 2013) and the PTF/M-dwarfs survey (Law et al. 2011) are collecting data.

But Jupiter-sized planets are not immediately favorable targets. Jupiter, with its scale height of 27 km, would cause a $\Delta_{\text{depth}} \sim 0.001\%$ per scale height. In other words, the transit depth of about 1% of the stellar light would show potential variations by 0.001% per scale height caused by the atmosphere, an amplitude barely within the reach of current instrumentations. However, Hot Jupiters are often found to possess inflated radii, WASP-17b being currently the extreme with a radius of 2 $\mathrm{R_{Jupiter}}$ (Anderson et al. 2011). The origin of these large radii are theoretically not completely understood. Observations show a clear trend of radius size with stellar incident flux (Demory & Seager 2011), however, heated atmosphere cannot account for the radii alone. Instead, additional energy needs to be deposited deeper in the interior. Theoretical approaches include e. g. tidal energy dissipation and ohmic heating from the dissipation of electric currents (Laughlin et al. 2011; Spiegel & Burrows 2013, and references therein). Such inflated planets are advantageous for transmission spectroscopy because of their large radius R_p and low surface acceleration g that increases H. The most exotic exoplanets have fluffy atmospheres of $H > 1000$ km, WASP-17b again being the extreme with H nearly 2000 km. A comparison of WASP-17b, two exoplanets investigated here and Jupiter and Earth in terms of H and Δ_{depth} is given in Table 2.1.

Table 2.1. Comparison of the potential transmission signal Δ_{depth} per scale height of selected exoplanets and Jupiter and Earth.

Planet	Scale height [km]	Transmission signal [% of stellar flux]
WASP-17b	1900	0.057
HAT-P-19b	630	0.031
HAT-P-12b	600	0.033
Jupiter	27	0.001
Earth	8	0.00002

The major criterion for our target selection was the detectability of a transmission signal, i. e. Δ_{depth}. Certainly, another important argument was the target brightness. However, it is easier to compensate for a lack in photons by the usage of larger telescopes or multiple transit observations than to compensate for low detectability. It is wrong to assume that for the detection of a smaller signal we just need a higher signal to noise ratio since somewhere at the level of $\Delta_{\mathrm{depth}} = 0.03\%$ ground-based observations reach a floor of correlated noise which can just be beat with unproportional higher effort.

The target selection for this PhD thesis was further determined by observational constraints like target visibility in general, target visibility at the moment of transits and the access to telescopes. Here, the access to telescopes on the northern hemisphere was more divers (LBT, GTC, Calar Alto, telescopes on the Canary Islands) than on the southern hemisphere (VLT). Furthermore, targets on the northern hemisphere were preferred due to the possibility of a monitoring with the AIP telescope STELLA on Tenerife.

The author of this thesis wrote in total ten proposals for observing time on 8m-class telescopes as PI, of which the majority was successful. Furthermore, a high number of proposals was sent to 1–4m telescopes for supplement observations. Here, we want to list the highlights:

- LBT proposals for spectroscopy of a transit of HAT-P-12b: In 2011A and 2012A we were granted observing time with the optical MOS spectrograph MODS. Unfortunately, only a partial transit was observed because of instrumental and weather problems. A similar observation of the same target was accepted with the 3.5m

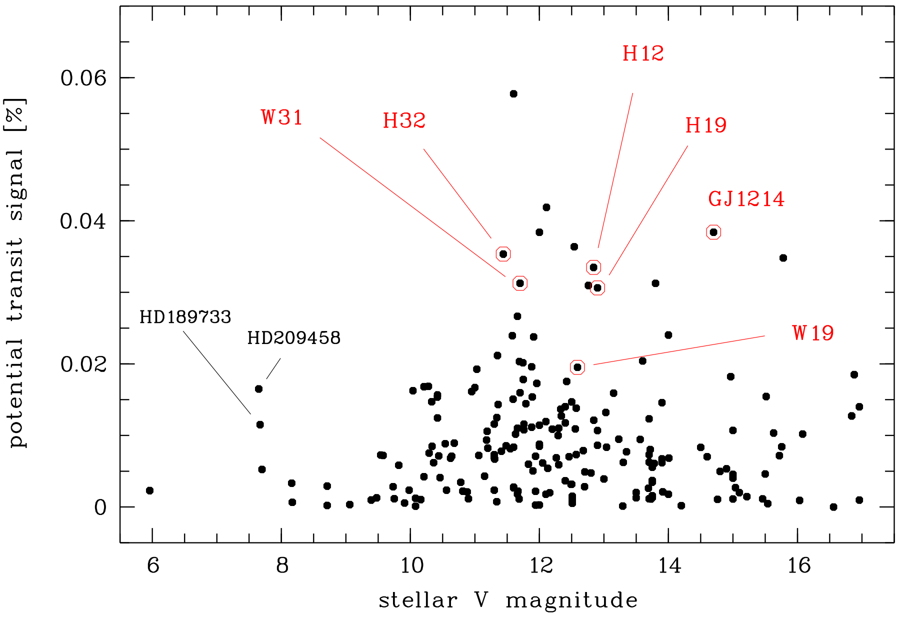

Fig. 2.2. The potential transit signal $\Delta_{\rm depth}$ over the apparent magnitude. The two quantities were among the main criteria for the target selection of this thesis. The chosen targets are marked with red circles, W31 stands for WASP-31, H32 for HAT-P-32.

telescope of Calar Alto, where data of two partial transits could be collected. The analysis of the LBT data is presented in Section 5.

- LBT proposals for spectroscopy of a transit of HAT-P-32b: In 2011B and 2012B we were awarded with telescope time for MODS to cover one transit. In the second season, a complete transit was successfully observed, an analysis is presented in Section 5.

- LBT proposals for spectroscopy of a secondary eclipse of WASP-33b: In three consecutive winter seasons 2010B, 2011B and 2012B we were granted observing time for an eclipse of WASP-33b with the NIR spectrograph LUCI and the optical camera LBC. In 2012B the event was successfully observed with LUCI+LBC in binocular mode. It constituted the first observation with the simultaneous usage of these two instruments. Unfortunately, the NIR data of LUCI turned out to be of too low quality, the very-near IR LBC data will be published in von Essen, Mallonn et al. (2014, submitted).

- LBT proposals for spectroscopy/spectrophotometry of a transit of GJ1214b: In three consecutive summer seasons 2011A, 2012A and 2013A we successfully proposed time for a transit either with the NIR spectrograph LUCI or the optical camera LBC. No data were obtained due to weather, technical or scheduling problems.

- DDT and Fast Track proposals for photometry of transits of HAT-P-12b: In 2014A we were awarded with observing time on the TNG, NOT and Calar Alto for one transit each of HAT-P-12b. The data are included in the analysis in Section 4.

- GTC proposal for spectroscopy of two transits of HAT-P-19b: We successfully proposed for time for two transit events with the optical spectrograph OSIRIS in 2011B.

PI was Ignasi Ribas, the author of this thesis was second author with major contributions. Just one transit observation was executed due to weather problems. Its analysis is presented in Section 3.

- VLT proposal for spectroscopy of transits of WASP-19b, WASP-25b, WASP-31b and WASP-39b: We were awarded with 28 hours of time on the optical spectrograph FORS2. Much time was lost because of weather. One complete transit of WASP-31b and one complete and one partial transit of WASP-19b was observed. The analysis is work in progress.

Figure 2.2 shows a comparison of all known transiting planets in a Δ_{depth} – V magnitude plane highlighting the targets for which we obtained data during the course of this PhD thesis.

2.2 Transit light curve fit and error analyses

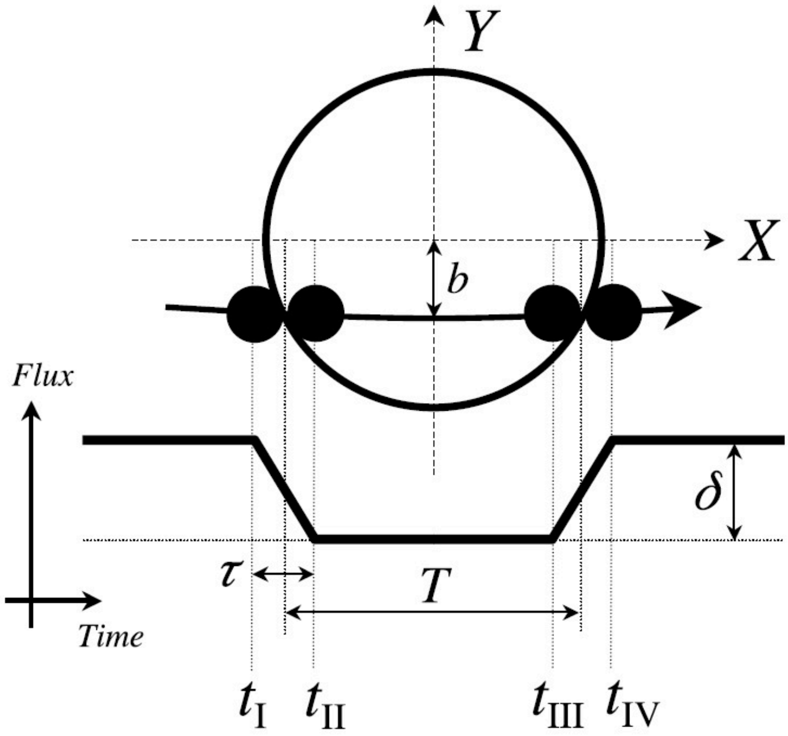

Fig. 2.3. Illustration of a transit light curve showing the geometric quantities T, τ and δ. Furthermore, the four contact times are indicated and the impact parameter b. Image taken from Winn (2010).

Three geometric quantities can be derived directly from the light curve of a planetary transit if we neglect stellar limb darkening for the moment: T, the interval between the halfway points of ingress and egress; τ, the duration of ingress or egress (which is the same under the assumption of a circular orbit with eccentricity $e = 0$) and δ, the drop in observed flux during transit. These quantities are illustrated in Figure 2.3 taken from Winn (2010). Additionally, a light curve provides the mid point of a transit T_0 and multiple transit measurements the orbital period P.

The three geometric quantities allow the determination of the three transit parameters $k = R_p/R_\star$, $R_\star/a$ and the orbital inclination i. R_p is the planetary radius, $R_\star$ the stellar radius and $R_\star/a$ the fractional stellar radius with a as the semi-major axis. Note that the transit light curves give no absolute radii of planet and star in kilometer. The radius ratio k is derived from δ by

$$\delta \approx k^2 \left(1 - \frac{I_p(t_{tra})}{I_\star}\right) , \tag{2.4}$$

with $I_p(t_{tra})$ as the disk-integrated intensity of the planet at the moment of the transit and $I_\star$ the disk-integrated intensity of the star (Winn 2010). The assumptions involved here are the neglect of stellar limb darkening, a homogeneous stellar surface without spots or bright regions and no variability of I_p and $I_\star$ on the time-scale of the transit duration. Since we can assume a spin-orbit synchronization for the Hot Jupiters investigated in this work, $I_p(t_{tra})$ is the intensity of the permanent night (dark) side of the planet and can be neglected for optical and NIR wavelengths (Kipping & Tinetti 2010). Therefore,

$$\delta \approx k^2 . \tag{2.5}$$

The inclination i is linked to the impact parameter b via $b = a \cos i/R_\star$, while b can be approximated by

$$b^2 \, = 1 - \sqrt{\delta}\, \frac{T}{\tau} , \tag{2.6}$$

under the assumption of non-grazing transits, $\tau \ll T$ and $R_p \ll R_\star \ll a$ (Winn 2010). A formula to solve for $R_\star/a$ is given by

$$\frac{R_\star}{a} \; = \; \frac{\pi}{\delta^{1/4}} \frac{\sqrt{T\tau}}{P} \left(\frac{1 + e \sin\omega}{\sqrt{1-e^2}}\right) , \tag{2.7}$$

with ω being the argument of periapsis.

Using Kepler's third law, a combination of the stellar mean density $\rho_\star$ and the planetary mean density ρ_p can be derived as a function of the fractional stellar radius:

$$\rho_\star \, + \, k^3 \rho_p \; = \; \frac{3\pi}{GP^2} \left(\frac{a}{R_\star}\right)^3 . \tag{2.8}$$

The second term on the left side is usually very close to zero since k^3 is very small, thus the formula reduces to a determination of $\rho_\star$ from pure transit photometry (Seager & Mallén-Ornelas 2003). Another useful quantity derived from photometry and radial velocity information is the planetary surface gravity g_p:

$$g_p \; = \; \frac{2\pi}{P} \frac{\sqrt{1-e^2}\, K_\star}{(R_p/a)^2 \sin i} , \tag{2.9}$$

with $K_\star$ as the radial velocity semi-amplitude of the star (Southworth et al. 2007b). Note that the derivation of g_p does not depend on any knowledge of the stellar properties.

For the determination of absolute dimensions, the planetary radius in kilometer and the planetary mass in kilogram, the transit photometry must be combined with the radial velocity orbit of the host star and external information about the star like its effective temperature, surface gravity and metallicity. Then, these information are typically related to the stellar mass, radius, composition and age by theoretical stellar evolutionary models. With the stellar radius in kilometers on hand, the planetary radius R_p follows from k, while the planetary mass M_p comes from Kepler's third law as

$$\frac{M_p}{(M_p + M_\star)^{2/3}} \; = \; \frac{K_\star \sqrt{1-e^2}}{\sin i} \left(\frac{P}{2\pi G}\right)^{1/3} . \tag{2.10}$$

Once a transit light curve is obtained, how do we practically derive the basic parameters δ, T, τ and T_0 and following i, k and $R_\star/a$? Mostly, a parametric model is fitted to the data which includes a calculation of the light curve as a function of the orbital and transit parameters. Then, this model is used in combination with some routine that optimizes the parameter values, typically by a minimization of the sum-of-squares statistic,

$$\chi^2 = \sum_{i=1}^{n} \left[\frac{f_i(\mathrm{obs}) - f_i(\mathrm{calc})}{\sigma_i} \right]^2 , \tag{2.11}$$

with f_i(obs) as the observed relative flux at the moment t_i, f_i(calc) as the calculated flux depending on the model parameters, and σ_i as the measurement uncertainty.

The parametric model and fitting routine we use throughout this work to derive the transit parameters is the publicly available software JKTEBOP[2] (Southworth et al. 2004). JKTEBOP is a heavily modified version of EBOP, a code used to model the light curves of detached eclipsing binaries (Popper & Etzel 1981). It is based on the Nelson-Davis-Etzel model (Nelson & Davis 1972; Etzel 1981) in which the discs of stars are approximated by biaxial ellipsoids. JKTEBOP applies the Levenberg-Marquardt minimization algorithm (Press et al. 1992) to find the least-squares best fit to a light curve.

We estimate the uncertainties of the transit parameters in this work with two different methods, a Monte Carlo (MC) simulation and a residual-permutation algorithm. As final error value we always adopt the higher value of both methods. In the MC approach a simulated light curve is generated by the addition of Gaussian noise to the best fit light curve model of the original data points. This simulated light curve is fitted identically to the original light curve and yields a new set of derived transit parameters. Typically, we use 5000 MC steps. From the distribution of these 5000 best fit parameters the $1\,\sigma$ uncertainties of the white light curve transit parameters are drawn as the 68.3% of highest probability.

The individual photometric error bars define the standard deviation of the Gaussian noise, therefore their reliability is of great importance for the reliability of the derived uncertainties. The original photometric uncertainties were obtained from SExtractor and include the photon noise of the source and sky background and the read-out noise. Hence, it forms a lower noise limit reachable under ideal condition. Errors of real measurements are usually slightly higher than that. Therefore, in a first step we always rescaled the individual errors with a common factor to give a reduced chi-square value of unity, $\chi^2_\nu = 1.0$, versus the fitted model. In a second step, we calculated the so-called β factor, a concept introduced by Gillon et al. (2006) and Winn et al. (2008) to include the contribution of correlated noise in the light curves. It describes the evolution of the standard deviation σ of the light curve residuals when they become binned in comparison to pure photon noise. For photon noise (which is Poisson distributed in the absence of correlated noise) we would expect

$$\sigma_N = \frac{\sigma_1}{\sqrt{N}} \sqrt{\frac{M}{M-1}} , \tag{2.12}$$

when the residuals are binned into M bins of N points each and σ_1 is the standard deviation of the original cadence. In the presence of correlated noise σ_N increases by the factor β. Two examples of the derivation are shown in Figure 2.4 using light curves from Section 4. The left panel shows a light curve without significant correlated noise. The standard deviation of the binned residuals follows in average the pendant from pure photon noise, i. e. $\beta = 1.0$. The right panel shows a light curve that suffers from correlated

---

[2] http://www.astro.keele.ac.uk/jkt/codes/jktebop.html

noise, the standard deviation of the measured data decreases slower than for white noise, i. e. $\beta > 1.0$. There is a dependence of this value on the bin size. Generally the duration of ingress/egress is used as a relevant time scale for transit photometry (e.g. Winn et al. 2008). It may occur that the derived β factor is smaller than 1 because of statistical fluctuations. Such cases were manually set to $\beta = 1.0$. We estimated the β factor of 10 000 randomly created datasets exhibiting Gaussian noise (β expected to be unity), averaged over binsizes typical for our light curves and found a statistical distribution of the β factors of standard deviation ~ 0.2. The derived β factor for each transit light curve was used as a factor to further enlarge the individual photometric error bars.

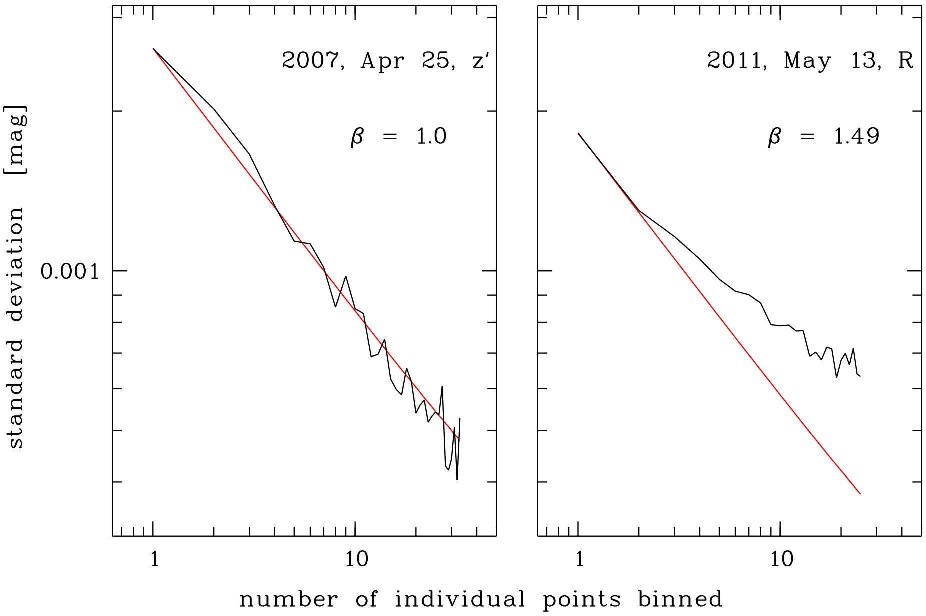

Fig. 2.4. Two examples for the estimation of the β factor by which the individual photometric errors get enlarged to account for correlated noise. Both light curves are transits of HAT-P-12b taken from Section 4. To the left, a transit is shown with no significant correlated noise on timescales of the ingress time and shorter, to the right a transit with a considerable correlated noise component is presented. In black we show the standard deviation of the binned residuals of observed data, in red the theoretical curve for pure photon noise.

Another way to include correlated noise into the analysis is a residual-permutation algorithm (Jenkins et al. 2002; Southworth 2008). It does not generate light curves adding white noise as the MC method, but generates new light curves adding the original residuals to the best fit model, just shifted by one data point in each step. The data point "falling off" at the end in each step gets wrapped around to the start of the data set. Each generated light curve, finally as many in number as there are individual data in the data set, is fitted identically to the original white light curve including the iteration loop of trend modeling and transit modeling. From the final distribution of transit parameters the $1\,\sigma$ uncertainties are drawn.

2.3 Stellar limb darkening

Stellar disks are brighter in the center than at the limb, an effect called *stellar limb darkening*. Its physical origin lies in the fact that an observer looks deeper in the stellar photosphere at the center of the disk than near its edge. The highly oblique viewing angle towards the edge causes the optical depth of unity to be reached at higher altitudes. And since the temperature and opacity depends on altitude in the photosphere, a deeper look in the atmosphere towards the center means a higher temperature and more intense radiation. Stellar limb darkening causes the transit to be deeper than k^2 when the planet blocks parts of the center of the stellar disk and transits shallower than k^2 with the planet near the stellar disk's edge. The effect is stronger at bluer wavelengths, giving the transit a very round shape in the blue optical region, whereas the bottom of the transit is nearly flat at NIR wavelengths. An illustration is presented in Figure 2.5.

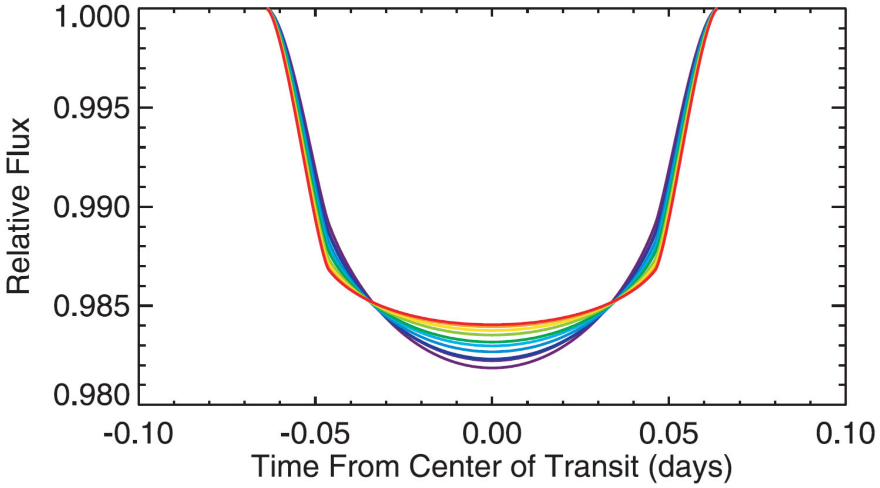

Fig. 2.5. Transit light curve models for the Hot Jupiter HD209458b from about 300 nm (purple line) to about 1000 nm (red line) illustrating the effect of stellar limb darkening on the light curve shape. Figure taken from Knutson et al. (2007).

The intensity distribution $I(\mu)$ over the stellar disk with $\mu = \cos\gamma$, γ being the angle between the line of sight and the emerging intensity, is typically described with

$$\frac{I(\mu)}{I(1)} = 1 - u(1-\mu) - v(1-\mu)^2\,, \tag{2.13}$$

which is the quadratic limb darkening law with the two limb darkening coefficients (LDC) u and v. Several other fitting formulas exist, e. g. the linear limb darkening law, a square root law or a logarithmic law. It is known that the intensity distribution over the stellar surface is a function of effective temperature and local gravity. While for hot stars the square root law provides an adequate fit, the quadratic law performs better for colder stars (Claret 2000). The best approximation independently of stellar type is given by a four parametric non-linear law introduced by Claret (2000). Southworth (2008) found no significant differences in the derived transit parameters for different choices of limb darkening laws when applied to typical ground-based transit light curves. Note the study of Kreidberg et al. (2014), who achieved one of the currently most precise transmission spectra of an exoplanet by the combined analysis of 12 HST transits. They used a linear law with the argument that the relative differences in transit depth among different wavelength channels is essentially unaffected by the choice of limb darkening law. Throughout this work we use the quadratic law of Equation 2.3, since it is appropriate for the temperature range of the investigated host stars and most commonly used in the literature of comparable investigations.

For most limb darkening laws the LDC can be retrieved from tabulated tables using a grid of stellar parameters (van Hamme 1993; Diaz-Cordoves et al. 1995; Claret et al. 1995; Claret 2000; Claret & Hauschildt 2003; Claret 2004; Sing 2010; Claret et al. 2012, 2013a). New calculations always followed up-to-date improvements in the stellar atmosphere modeling, e. g. improved line list, computation of condensate clouds or spherically symmetric vs. plane parallel models. However, theoretical LDC contain systematic uncertainties. They can be revealed by the comparison of calculations of different authors, of calculations using different stellar atmosphere models or of calculations applying different fitting approaches for the limb darkening laws. These uncertainties are often on the level of 0.1 (Csizmadia et al. 2013), which is significant because the LDC usually range from -0.1 to 0.8. High-accuracy transit light curves present the valuable chance to directly measure the LDC and thus test their theoretical prediction. Recent studies of this kind supplied divers results: High-accuracy light curves from HST for HD209458b reveal a significant discrepancy between measured and calculated LDC (Claret 2009), while light curves of similar high quality from HD189733b yield LDC that agree with their theoretical predictions (Hayek et al. 2012; Pont et al. 2013). Müller et al. (2013) tested the agreement for a sample of 38 Kepler targets using the quadratic limb darkening law and found in general good agreement for the linear LDC u, but a systematic difference on the order of 0.05 for the quadratic LDC v.

Thus, how do we treat the LDC in the transit fit? Csizmadia et al. (2013) recommends to fit the LDC whenever the quality of the light curves allows for it. However, Southworth (2012) showed that typical ground-based transit light curves cannot constrain both u and v because they are correlated. Often, fitting for both yields unphysical values with huge error bars. One possible solution regularly found in the literature is to fit for $u_+ = u + v$ and $u_- = u - v$ instead of u and v because of a reduced correlation of these two new parameters (Giménez 2006). The approach used throughout this thesis is to fit for just the linear LDC u, but to fix the other LDC v to its theoretical value. This ensures that the fits are not significantly biased by adopting a stellar atmospheric model and avoids the degeneracies between fitting multiple limb-darkening parameters. Here, v is perturbed by ± 0.1 during the error estimation to account for systematics in the theoretical calculation.

2.4 Correction for starspots

The modeling of exoplanet transit light curves and the derivation of transit parameters assumes that the host star is a homogeneous source of background light for the transit event. If the visible stellar surface shows spatial brightness variations for example caused by dark starspots or bright regions, faculae and plages (Strassmeier 2009), the measured transit parameters, especially the transit depth, can be modified significantly (Pont et al. 2008; Czesla et al. 2009).

An occultation of a starspot by the transiting planet causes a bump in the light curve on the timescale of the transit ingress/egress, which leads to a shallower transit and an underestimation of the planet size if uncorrected. Starspots unocculted by the planet cause the average brightness to be higher along the transit chord than on the rest of the stellar hemisphere, which leads to deeper transits and an overestimation of the planet size. Both effects are wavelength dependent because spots have a different temperature and spectral energy distribution than the unspotted photosphere. Generally, the effects are much stronger in the blue optical region than in the NIR. Therefore spots, whether occulted or unocculted, can modify the derived transit parameter and also significantly affect the transmission spectrum. Examples of active exoplanet host stars with frequently observed starspot crossings are HD189733 (see Pont et al. 2013 and references therein) and WASP-19 (Tregloan-Reed et al. 2013; Huitson et al. 2013).

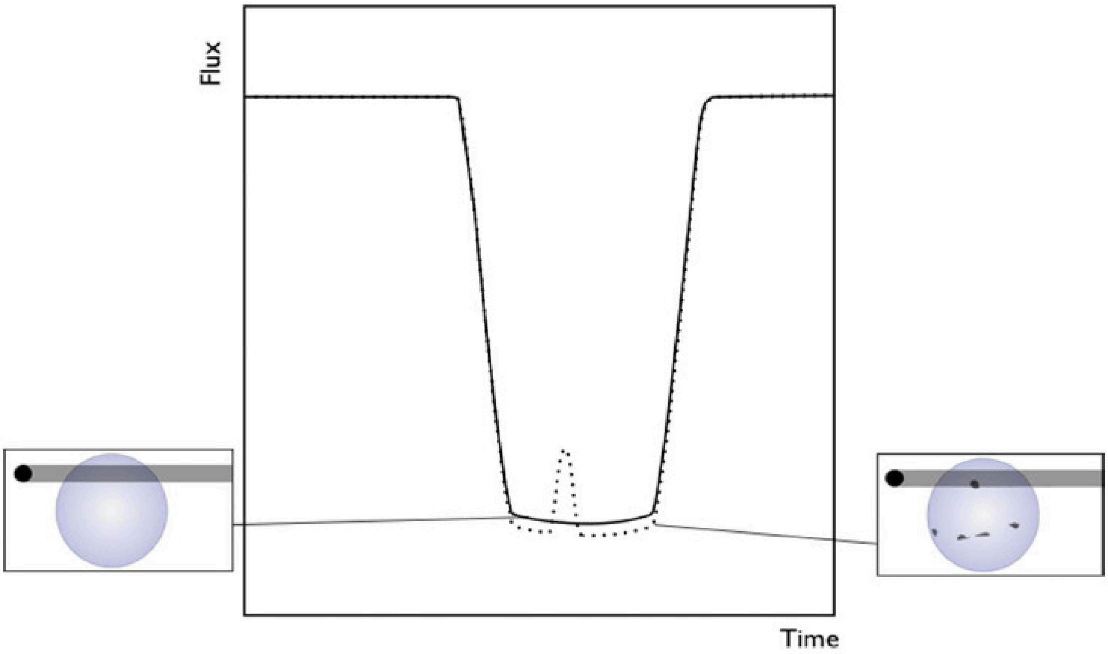

Fig. 2.6. Illustration of the effect of stellar spots on exoplanet transit light curves. The continuous line shows the transit curve when the host star has a homogeneous surface, the dotted line shows the transit curve in presence of spots. Spots occulted by the planet cause a bump in the light curve, while unocculted spots deepen the transit due to the reduction of the mean brightness of the photosphere outside the transit chord. Figure taken from Pont et al. (2013).

In the case of an unspotted host star, the transit depth d is proportional to the fraction of the stellar disc that is blocked by the disc of the planet.

$$d \propto \frac{\pi R_p^2}{\pi R_\star^2} = \left(\frac{R_p}{R_\star}\right)^2 . \tag{2.14}$$

If the star is spotted, the relation changes to

$$d \propto \frac{\alpha R_p^2}{\alpha' R_\star^2} , \tag{2.15}$$

with α as the mean brightness of the stellar surface crossed by the planet compared to its unspotted equivalent and α' as the same quantity for the surface region unocculted by the planet (Pont et al. 2013).

One way to derive a value for the quantity α/α' are transit measurements at well separated wavelengths for planets with a very low scale height. However, for planets with large scale heights (the preferred targets for transmission spectroscopy), the measured change in transit depth over wavelength caused by starspots and by an absorption in the planetary atmosphere are of the same order of magnitude for moderately active host stars. Therefore, an independent measurement of the stellar flux variation at the time of the transit is needed to estimate the spot influence on the transit parameters and break the degeneracy between a transit depth wavelength dependence modulated by spots or planetary atmosphere.

For this reason, a photometric monitoring can be found in the literature for the host stars HD189733 (Pont et al. 2013), WASP-19 (Huitson et al. 2013), WASP-12 (Sing et al.

2013), HAT-P-1 (Nikolov et al. 2014), GJ1214 (Berta et al. 2011) and GJ3470 (Biddle et al. 2014). For the same reason of starspot correction, part of this thesis was the initialization, supervision, reduction and analysis of monitoring campaigns for the host stars HAT-P-19 (described in Section 3), HAT-P-12 (see Section 4), HAT-P-32 (see Section 5), GJ1214 (Nascimbeni, Mallonn et al., submitted; Angerhausen, Dreyer et al. in prep.) and HAT-P-26 (not yet analyzed).

Two assumptions are involved in this description: The contribution of faculae and plage regions on the transit parameters is assumed to be negligible as well as the error in assuming one single set of limb darkening coefficients for spots and stellar photosphere. According to our understanding of cool stars and the Sun, dark spots are well-defined regions of lower flux. In contrast, faculae and plages are arranged more uniformly across the stellar surface and hence their effect tend to average out in the disc integrated flux. Furthermore, the facula contribution to the stellar flux variation in the optical weakens for stars more active than the Sun (Gondoin 2008; Lanza et al. 2009). Another argument to neglect the contribution of bright regions is that no space and ground-based transit observation of the active star HD189733 has revealed indications of the crossing of faculae, while starspot crossings were frequently observed.

For an estimation of the parameter α' we assume that the spots and their spectral energy distribution does not change over the time scale of a planetary transit, which is justified by the generally much longer rotation period of the star. Then, the estimation is given by

$$\alpha' = 1 - \Delta f(t, \lambda) \,, \tag{2.16}$$

with

$$\Delta f = \frac{f_{\mathrm{meas}} - f_{\mathrm{quiet}}}{f_{\mathrm{quiet}}} \,. \tag{2.17}$$

Hence, the change in transit depth $\Delta d/d$ equals the flux dimming Δf,

$$\Delta d/d = \frac{\Delta (R_p/R_\star)^2}{(R_p/R_\star)^2} = \Delta f \,, \tag{2.18}$$

an equation used in this or a similar form also by Berta et al. (2011), Sing et al. (2011b) and Huitson et al. (2013).

Thus, an estimation of Δf depends on three quantities: The stellar flux level f_{meas} at the time of the transit observation, the stellar flux level without spot dimming f_{quiet} and to account for the wavelength dependence of Δk the effective temperature of the spots T_{spot}. It is likely that spots are present at every moment of the monitoring, therefore f_{quiet} cannot be measured directly. Instead, it needs to be estimated. An approximation of the level of a permanent flux dimming is the level of the variance of the long term light curve, an approach undertaken by Pont et al. (2013) in the case of HD189733b based on the work of Aigrain et al. (2012).

An estimation of α, the mean brightness along the transit chord in ratio to the mean brightness of the unspotted photosphere, is difficult if not impossible because the monitoring photometry provides no information about the latitude of a spot. However, the uncertainty of the influence of occulted spots just causes problems if the bump cannot be photometrically resolved in the light curve. Once a bump is resolved, the corresponding data points can be either weighted with zero in the transit modeling or the starspot can be modeled (under certain assumptions) in size and temperature simultaneously to the transit (see e.g. Tregloan-Reed et al. 2013). If the photometric accuracy and time sampling does not allow for the resolution of the bump (maybe many small spots are distributed evenly along the transit chord), it is only possible to give an upper limit of the spot influence by the assumption that all the spots causing the measured flux dimming Δf are located along the transit chord:

$$\alpha = 1 - \Delta f(t,\lambda)\frac{A}{A_o}\,, \tag{2.19}$$

with A being the visible surface area of the entire star and A_o the area of the stellar surface occulted during transit.

2.5 Model predictions of theoretical spectra

One of the first theoretical prediction on exoplanet transmission spectra was given by Seager & Sasselov (2000). They made use of similarities of the expected temperature-pressure profile for Hot Jupiters and Brown dwarfs, especially L dwarfs. Both classes of objects have temperatures T_{eff} of roughly 1500 K, therefore the dominant opacity sources were expected to be the same. Seager & Sasselov (2000) found the alkali metals sodium and potassium to dominate the optical spectrum with a contribution of Rayleigh-scattering caused by H_2 molecules at the very blue wavelengths. Similar results were found by Brown (2001) and Hubbard et al. (2001). Sudarsky et al. (2003) investigated the effect of strong irradiation on exoplanet spectra.

TiO and VO produce strong absorption features in the spectra of cool stellar atmospheres and are also expected to play a role in the spectral appearance of Hot Jupiters above 2000 K (Burrows et al. 2006). Absorption by this molecules at high altitudes might be the source of temperature inversions measured with the Spitzer band passes for several exoplanets (e.g. Burrows et al. 2007). Fortney et al. (2008) suggested the classification of Hot Jupiters in two classes, the pM and the pL class in analogy to the M and L stellar type. The pM planets are hotter than their counterparts, show opacity of TiO and VO in their optical spectrum and possess a temperature inversion in their atmosphere at low pressure. The pL planets are somewhat cooler without absorption of TiO and VO and without a temperature inversion. The authors expected the boundary between the two classes to depend mainly in the incident flux that the planet receives from its host star, a fact that could not be confirmed by empirical data (Knutson et al. 2010). The role of TiO and VO is still not clear in the spectra of Hot Jupiters, since so far just a single tentative detection of corresponding absorption features in a transmission spectrum was reported (Désert et al. 2008). Spiegel et al. (2009) described how TiO might be lost out of the higher regions of the atmosphere by condensation. Very strong vertical mixing would be needed to lift TiO up into hotter parts of the atmosphere again.

Already Seager & Sasselov (2000) described how an opaque cloud deck blocks parts of the atmosphere and weakens spectral absorption features. Absorption features originating in deeper parts of the atmosphere cannot contribute and are “cut” from the spectrum. Hence, a detection of pressure-broadened wings of e. g. the alkali lines indicates a transmission spectrum that probed quite deep into layers of higher pressure and are therefore approximated with clear atmosphere models. On the other hand, the absence of such dominant features does not allow for a unique explanation at the current typical measurement precision: Such spectrum can be equally well explained by clouds blocking the deeper parts of the atmosphere and by a low abundance of the relevant chemical species.

A detection of a Rayleigh slope could be indicative for a clear atmosphere with scattering by H_2 molecules, or a haze layer or a structured cloud with a transparent layer of microscopic particles on top. The cloud models of Woitke & Helling (2003) and Helling et al. (2008) result in a cloud structure whose layers differ significantly in elemental composition, mean grain size and other physical parameters. Seed particles form from a super-saturated gas environment (nucleation) and serve as a surface to allow for the condensation of a variety of thermally stable chemical compounds (growth of the grains). Immediately after their formation the grains start to settle down gravitationally, grow further and eventually reach an altitude where they evaporate. Convective mixing carries the uncondensed material back to higher altitude where the cycle begins again. These models predict observable Rayleigh scattering similar to the spectrum of HD189733b (Section 2.6.2) caused by submicrometer-sized silicate haze in the upmost layer of the cloud, whose number densities are too small to form an opaque cloud deck. However, the altitude at which clouds form is temperature dependent: The clouds form too low to be measurable for planets colder than 1200 K. For planets hotter than 2200 K the lower opaque layers of the clouds will be present at higher altitudes and flatten the exoplanet transmission spectrum.

Since Seager & Sasselov (2000), the theoretical modeling improved by e. g. the inclusion of more opacity sources and effects such as thermal ionization and by the combination of radiative transfer with general circulation models (Fortney et al. 2010; Burrows et al. 2010). However, they still rely on 1D model temperature-pressure profiles and mostly assume solar metallicity and chemical equilibrium of neutral and ionic species. The effects of clouds or photoionization are hardly taken into account. Models with abundance ratios different from solar-type were calculated by Madhusudhan et al. (2011) and Madhusudhan (2012), which provide varying C/O ratios. Figure 2.7 gives model examples from Fortney et al. (2010) for Hot Jupiters with equilibrium temperature of 500 to 2500 K showing absorption features of Na, K, H_20, CH_4 and CO. Absorption in transmission spectra appears as increase in planetary radius.

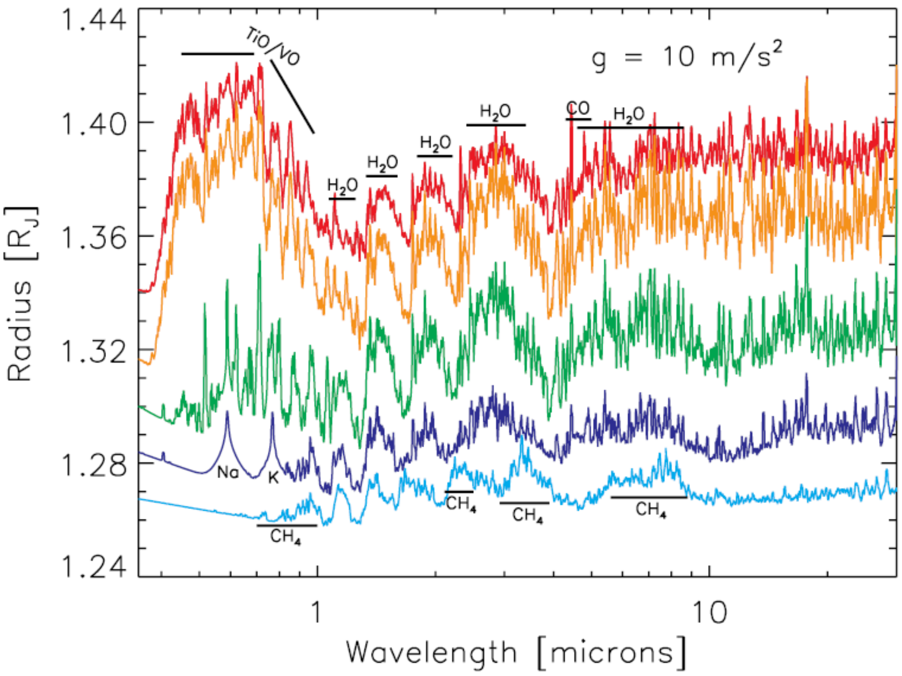

Fig. 2.7. Theoretical transmission spectra for Hot Jupiter exoplanets of T = 2500, 2000, 1500, 1000, and 500 K, from top to bottom. Prominent absorption features, which appear as increases in the planetary radii, are labeled. Figure is taken from Fortney et al. (2010).

2.6 Literature review of observations

Here, we want to give an overview about the current set of exoplanet observations. We concentrate on results obtained by transmission spectroscopy about the terminator region of the planets in contrast to emission spectroscopy that probes the day side. Furthermore, we focus on the available optical and NIR data sets and leave measurements in the UV and mid-IR mostly aside. For a more comprehensive review including transmission spectroscopy, emission spectroscopy and orbital phase curves we refer to Madhusudhan et al. (2014) and references therein.

The currently three best studied exoplanets are HD209458b, HD189733b and GJ1214b. The first two orbit bright host stars, V = 7.6 for HD209458 and V = 7.8 for HD189733. They are not among the most favorable objects in terms of signal strength per scale height, see Figure 2.2, but the high number of photons received per time interval allow for high precision measurements. The majority of atmospheric information for these two objects were gathered with space-based platforms because of the lack of equally-bright near-by comparison stars for the calibration of atmospheric effects and because systematic effects in the measurements are better understood for HST and Spitzer than for most ground-based observatories. GJ1214b is the only known transiting super-Earth with an atmosphere accessible by the current sensitivity limits. Although space-based measurements supplied the highest quality data for this object, ground-based observations contributed a lot to the current understanding of GJ1214b's atmosphere.

2.6.1 HD209458b

The measurement of sodium absorption in the atmosphere of HD209458b with HST by Charbonneau et al. (2002) formed the very first detection of an exoplanet atmosphere. This absorption at the sodium D line was later on confirmed and measured to higher sensitivity (Narita et al. 2005; Barman 2007; Snellen et al. 2008; Sing et al. 2008a,b). The sodium absorption is not only confined to the line core. Instead, the pressure broadened wings are also visible in the spectrum (Figure 2.8), indicative of absorption deep in the atmosphere, hence of a cloud-free atmosphere (Sing et al. 2008a,b). Furthermore, the sodium line shows an absorption plateau between the core and the wings, interpreted as evidence for a drop in sodium abundance at a certain altitude (Sing et al. 2008b). The measured profile of the sodium D line was also used for an empirical derivation of the temperature-pressure profile at the terminator (Vidal-Madjar et al. 2011). This study revealed a high-altitude temperature inversion, in agreement to the inversion measured on the day side (Knutson et al. 2008).

The extra absorption on the redward sodium wing could be a hint on TiO in the atmosphere (Désert et al. 2008), a potential reason for the temperature inversion as optical opacity source. In the UV region absorption of Lyman α was detected extending beyond the Roche lobe[3] (Vidal-Madjar et al. 2003), evidence for an atmospheric escape. In the optical, absorption by Hα was found (Jensen et al. 2012). Another feature of the optical spectrum is a blueward slope of additional absorption, most plausible explained by Rayleigh-scattering from H_2 molecules (Lecavelier Des Etangs et al. 2008b).

In the NIR, Snellen et al. (2010) detected the presence of CO. The same measurements also allowed for the first time for the derivation of the orbital velocity of an exoplanet, and therefore for a very accurate independent constrain on the planet mass. Furthermore, a strong wind was detected at the terminator from the hot day-side to the somewhat cooler night-side of the planet (Snellen et al. 2010). Deming et al. (2013) targeted the NIR water absorption band at ~ 1.4 μm with the HST and were able to detect it. However, the weakness of the water feature is discrepant to the measured extend of the water feature at 0.9 μm (Knutson et al. 2007; Barman 2007) and can be best explained by a source of additional opacity like clouds or haze in the atmosphere that weaken absorption features.

---

[3] The Roche lobe is the region of space around a body in a multi-component system (e. g. star-planet system) within which orbiting material is gravitationally bound to that body.

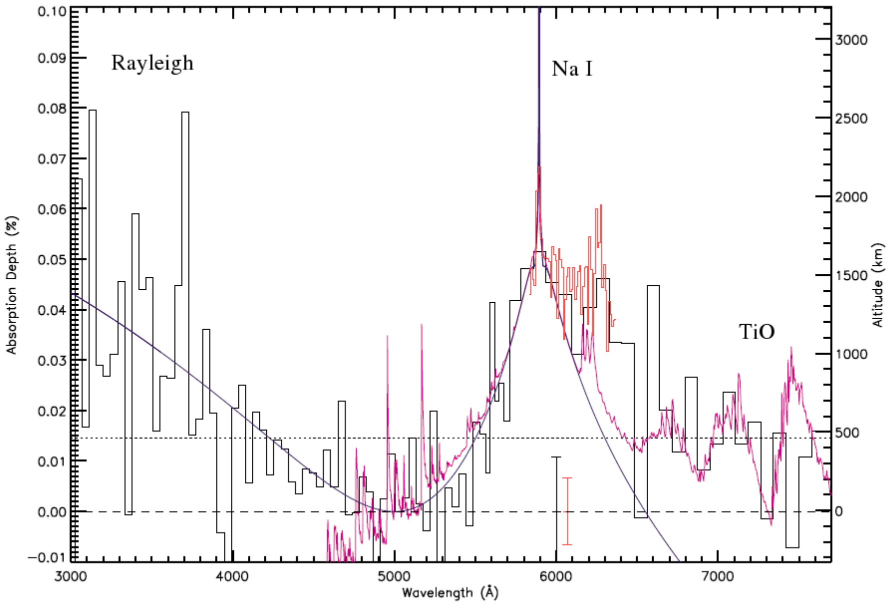

Fig. 2.8. Observed transmission spectrum of HD209458b. In black the low resolution data are shown, in red the medium resolution data from Sing et al. (2008a). Representative error bars are plotted. The dotted horizontal line denotes the mean planetary radius from Knutson et al. (2007). Plotted in blue is a transit absorption model which contains opacity from atomic Na, Rayleigh scattering, and includes upper-atmospheric Na depletion. The model in purple includes Na, TiO, and VO. Figure is taken from Sing et al. (2008b).

This, in turn, contradicts the interpretation of the measured broad sodium wings of a clear atmosphere.

2.6.2 HD189733b

The transmission spectrum of HD189733b looks very different from the one of HD209458b and is famous for its Rayleigh-scattering slope extending all the way from the near-UV till the very-near IR (Pont et al. 2008; Sing et al. 2011b; Pont et al. 2013). A possible source causing this scattering is a haze layer of MgSiO3 grains of sizes of 0.01–0.03 μm (Lecavelier Des Etangs et al. 2008a). In the optical, no other dominant spectral feature exist because the deeper atmospheric layers are blocked by the haze. Absorption from sodium is only measured in its core by Redfield et al. (2008), which formed the first ground-based detection of an exoplanet atmosphere. About an additional absorption of the potassium line core there are conflicting measurements: While Jensen et al. (2011) reported a Null-detection, Pont et al. (2013) reported a detection at the 2.5 σ level.

There is a controversy about spectral water features seen in transmission: Sing et al. (2009) could not confirm the water absorption found by Swain et al. (2008), both studies used the NICMOS instrument of HST. Gibson et al. (2011) re-analyzed the data and found significantly larger error bars for the Swain et al. (2008) measurements. Follow-up observations have shown that the influence of the haze extends into the NIR with no detection of molecular features (Gibson et al. 2012; Pont et al. 2013, see Figure 2.9). However, McCullough et al. (2014) detected a water feature at 1.4 μm, significantly smaller in amplitude than the Swain et al. (2008) result.

The host star HD189733 is magnetically active with photometric variation on the level of 3% (Pont et al. 2013). Although all transmission studies included the effects of starspots in their analysis, McCullough et al. (2014) formulated recently an opposing interpretation of the optical to NIR transmission spectrum: They proposed a clear atmosphere and explained the Rayleigh slope with a combination of scattering from H_2 molecules and systematic effects of unocculted starspots and the lack of pressure-broadened alkali line wings with a very low abundance caused by condensation and subsequent gravitational settling.

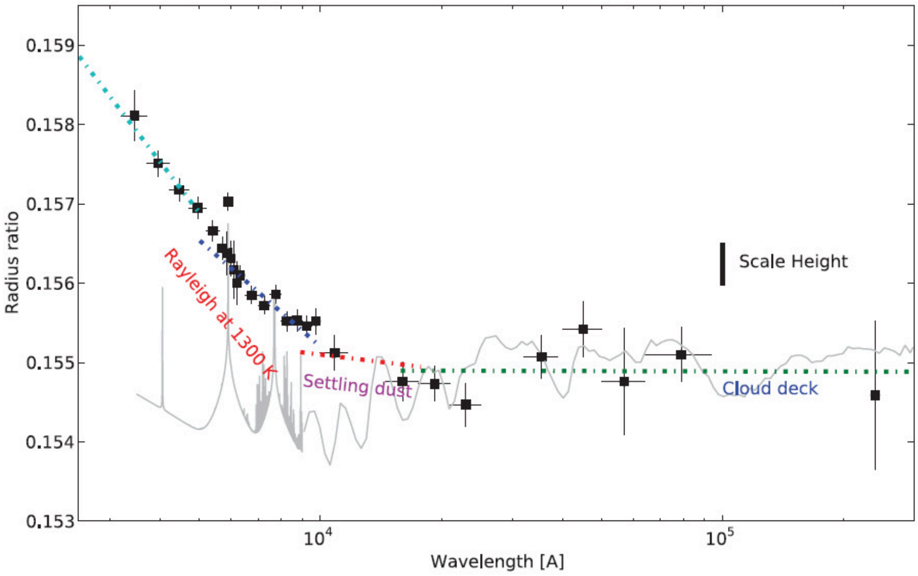

Fig. 2.9. Observed transmission spectrum of HD189733b from the near-UV to the mid-IR. Overlaid in gray is a theoretical spectrum of a cloud/haze-free atmosphere. Figure taken from Pont et al. (2013).

Huitson et al. (2012) was successful in the empirical determination of the temperature-pressure profile along the terminator, finding a temperature inversion similar to the thermosphere of HD209458b. Emission spectroscopy shows that the day side lacks a temperature inversion (Deming et al. 2006; Charbonneau et al. 2008; Swain et al. 2009). However, Pont et al. (2013) demonstrate that the day side emission data are consistent with an increase in temperature for an increasing altitude when the haze/dust is included in the modeling. Jensen et al. (2012) found Hα absorption in the atmosphere of HD189733b and combined it with a Lyman α measurement from Lecavelier Des Etangs et al. (2010) to derive the hydrogen excitation temperature.

2.6.3 GJ1214b

The discovery of GJ 1214b by Charbonneau et al. (2009) represented a milestone along the way towards the detection and characterization of habitable exoplanets. It is a super-Earth whose atmosphere lies within the reach of current observing facilities due to the small size of its M4.5 type host star and its potentially large scale height: If the gas layer is dominated by H_2/He the planet would show measurable variations of the transit depth with wavelength of the order of 10^{-3} (Miller-Ricci & Fortney 2010). The mean density derived from the radius of 2.65 Earth radii and mass of 6.45 Earth masses, intermediate to solar type terrestrial planets and gas giants, could be explained by a variety of interior compositions: The planet might be either (i) a terrestrial planet with an outgassed hydrogen-rich atmosphere, (ii) a small version of Neptune formed by the accretion of gas from the protoplanetary nebula or (iii) a water-world composed mainly of water ice with a secondary water vapor envelope formed by sublimation (Rogers & Seager 2010; Nettelmann et al. 2011). Thus, the attempt to measure planetary radius variations is an attempt to constrain the mean molecular weight μ of the atmosphere. If transit depth variations of the order of 10^{-3} could be measured, μ would be very low ruling out the composition (iii) with a water vapor atmosphere.

However, the very first investigation of GJ1214b's atmosphere of Bean et al. (2010) showed no measurable variations in transit depth from 780 to 1000 nm, strongly disfavoring a cloud-free, H_2/He-dominated atmosphere. This observation was pioniering work for ground-based transmission spectroscopy with MOS spectrographs using very wide slits, a technique that we also employed during the time of the PhD, see e. g. Section 5. Désert et al. (2011) used the warm Spitzer Space Telescope at 3.6 and 4.5 μm and confirmed the planet star size ratio found in the optical. However, the interpretation of this remarkably flat transmission spectrum was challenged when Croll et al. (2011) found a significantly deeper transit depth in the K band, just explainable by an atmosphere of low μ. Another observations tentatively indicating enhanced absorption and therefore a low μ was obtained by de Mooij et al. (2012) at Sloan g', interpretable as Rayleigh scattering. Repeated observations in the NIR and blue optical wavelengths could not confirm the enhanced absorption (Bean et al. 2011; Berta et al. 2012; de Mooij et al. 2013). At about this time, in the years 2011, 2012 and 2013, we were awarded with observing time at the LBT for observations in B, H and K with the same goal to test the enhanced observations of Croll et al. (2011) and de Mooij et al. (2012). Unfortunately, no observations could be executed. Instead, we obtained Sloan g' band data of multiple transits with the 1.2m STELLA telescope, whose final error bars were too large to constrain the atmospheric models. A detailed description of the STELLA analysis and interpretation is not part of this thesis and can be found in Teske et al. (2013).

So far, the combined sample of measurements could be explained by either a high mean molecular weight composition or a gray opacity source like clouds. This degeneracy was lifted when Kreidberg et al. (2014) reached the sensitivity to detect the much smaller absorption features predicted for a cloud-free high mean molecular weight atmosphere. Despite the much improved sensitivity, the measured spectrum was still flat (see Figure 2.10), ruling out chemical compositions with traces of H_2O or CH_4 and pure compositions of CO and CO_2. Note that this also included a cloud-free Earth-like atmosphere that was ruled out. The most plausible remaining interpretation are clouds.

The example of GJ1214b shows impressively how severe the effect of clouds can be for transmission spectroscopy of exoplanet atmospheres. Despite the large sample of observations undertaken with the HST, Spitzer and almost every ground-based large aperture telescope, we do not know anything about the atmosphere, except that there are clouds. With all recent observations combined it is currently not possible to give any conclusion about the chemical composition.

2.6.4 Other Hot Jupiters

The very different spectra of HD209458b and HD189733b already show a diversity in exoplanet spectra that was revealed further with observations of other Hot Jupiters. Here, we give an overview about the current results of transmission spectroscopy in the optical wavelength region of Hot Jupiters. We concentrate on the results obtained in low spectral resolution $R \leq 200$ obtained from the analysis of transit light curves (spectrophotometry) and leave aside other very interesting results for smaller planets like GJ436b (see Knutson et al. 2014a, and references therein) or GJ3470b (see Ehrenreich et al. 2014, and references therein).

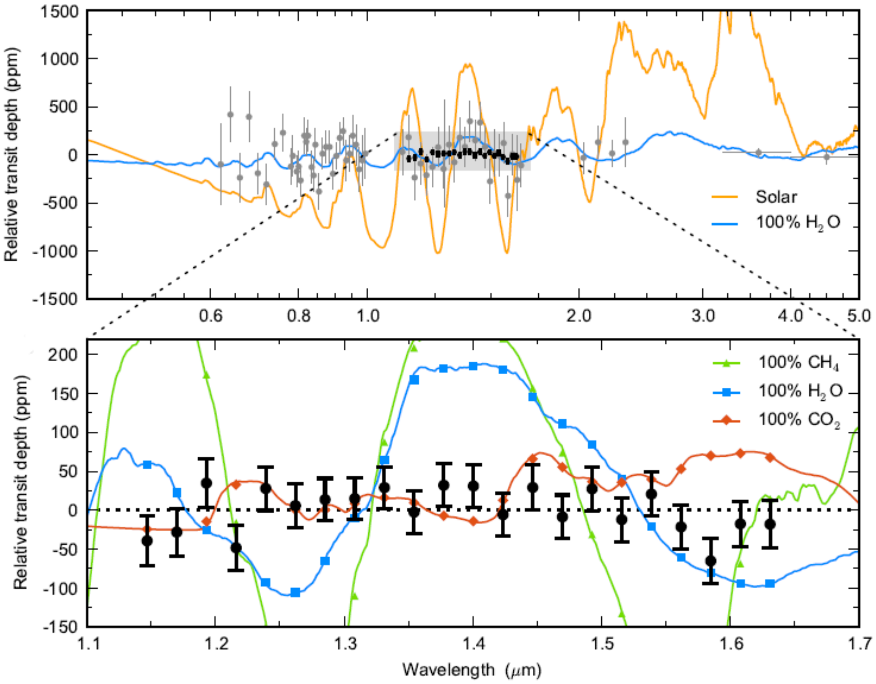

Fig. 2.10. Observed transmission spectrum of GJ1214b. Upper panel: Measurements from Kreidberg et al. (2014) (black points) and previous work (see Kreidberg et al. 2014, and references therein)(gray points), compared to theoretical models (lines). Previous data rule out a cloud-free solar composition (orange line), but are consistent with a high-mean molecular weight atmosphere (e. g. 100% water, blue line) or a hydrogen-rich atmosphere with high-altitude clouds. Lower panel: Detail view of the measured transmission spectrum of Kreidberg et al. (2014) (black points) compared to high mean molecular weight models (lines). The data are consistent with a featureless spectrum, but inconsistent with cloud-free high-mean molecular weight scenarios. Figure taken from Kreidberg et al. (2014).

Theoretical investigations predicted the alkali metals sodium and potassium to produce dominating absorption features in the optical. Robust detections observed in low spectral resolution exist for HD209458b (Sing et al. 2008b), HAT-P-1b (Nikolov et al. 2014) and XO-2 (Sing et al. 2012). Murgas et al. (2014) presented a likely detection of Na for WASP-43b. The (low-resolution) non-detection in the atmospheres of HD189733b and WASP-12b can be explained by scattering particles blocking the atmospheric heights probable for atomic sodium and potassium (Pont et al. 2008; Sing et al. 2013). The non-detection of alkali absorption in WASP-29b and HAT-P-32b can either be explained by clouds strongly muting the spectral features or by sub-solar abundances of sodium and potassium (Gibson et al. 2013a,b). Sing et al. (2011a) found significant K absorption in the atmosphere of XO-2b using spectrophotometry with narrow-band tunable filters giving higher spectral resolution of $R \sim 800$.

A spectral slope in the optical indicative of Rayleigh scattering by aerosols has been found for HD189733b (Pont et al. 2008, 2013), WASP-12b (Sing et al. 2013) and WASP-6b (Jordán et al. 2013). Contrary, the optical spectra of HD209458b and XO-2b are best explained by a clear atmosphere model (Sing et al. 2008b, 2011a, 2012). HD209458b also features a Rayleigh slope shortward of 5000 Å, which is interpreted as scattering by H_2 molecules instead of aerosols (Lecavelier Des Etangs et al. 2008b).

Indications for the presence of TiO in the terminator region was so far just found for HD29458b (Désert et al. 2008) and WASP-12b, in the latter case also TiH being an alternative solution for the measurements (Stevenson et al. 2013). While this molecular absorption in HD29458b still lacks an independent confirmation, a follow-up HST observation of WASP-12 found no indications for TiO anymore (Sing et al. 2013). TiO was not detected in the probably cloud-free atmospheres of WASP-19b (Huitson et al. 2013) and XO-2b (Sing et al. 2011a). Furthermore, it was ruled out for the somewhat cooler atmospheres of HAT-P-1b (Nikolov et al. 2014). The non-detection of TiO in HD189733b and HAT-P-32b can be explained by clouds/haze on top of the atmosphere (Pont et al. 2008; Gibson et al. 2013b).

3 Transmission spectroscopy of HAT-P-19b with OSIRIS@GTC

3.1 Introduction

Here we report a search for sodium absorption in the atmosphere of HAT-P-19b using ground-based differential spectrophotometry. This ground-based technique was pioneered by Bean et al. (2010) for the super-Earth GJ1214b as the search for chromatic transit depth variations among a set of simultaneously observed light curves. We observed one transit event with the optical spectrograph OSIRIS at the Gran Telescopio de Canarias (GTC). Several studies already proved the capability of OSIRIS for optical transit spectrophotometry (Sing et al. 2011a, 2012; Colón et al. 2012; Murgas et al. 2014).

HAT-P-19b is a Hot Jupiter with a period very close to 4 days (Hartman et al. 2011a, hereafter H11). It is similar to Jupiter in size (1.13 $\mathrm{R_J}$) and to Saturn in mass (0.29 $\mathrm{M_J}$), giving it a very low surface gravity of about 6 m/s^2. The equilibrium temperature was estimated by H11 to 1010 K. Hence, the scale height is $\sim$600 km assuming Jupiter's mean molecular weight of 2.2 g/mole. The planet transits a K type main sequence star of V $=$ 12.9 mag, $M = 0.84\,\mathrm{M_\odot}$ and $R = 0.82\,\mathrm{R_\odot}$. A big advantage for differential spectrophotometry is the presence of a near-by reference star, very similar in brightness, just 1.5 arcminutes away and of similar spectral type.

As brightness inhomogeneities on the stellar surface affect the derivation of transit parameters and the slope of the transmission spectrum (see Section 2.4), the knowledge of a long-term flux variation and the stellar flux level at the time of the transit observation can be used to correct for this influence if present. For this reason, we performed a two-color monitoring campaign for HAT-P-19 using the 1.2m telescope STELLA on Tenerife over a time span of about 300 days.

3.2 Observations and data reduction

We observed the exoplanet host star HAT-P-19 in service mode during one transit event with the GTC located at the Observatorio del Roque de los Muchachos on the island La Palma and operated by the Instituto de Astrofísica de Canarias. We monitored the star with the STELLA 1.2m telescope of the Leibniz Institute for Astrophysics Potsdam (AIP) installed in the Observatorio del Teide on the island Tenerife.

3.2.1 Spectroscopic GTC OSIRIS observation

Instrument Setup

During the transit observation we made use of GTC's optical spectrograph OSIRIS. The dispersive element was the VPH R2500R providing a wavelength coverage of 5600 to 7500 Å and a dispersion of about 1 Å per binned pixel. We used the widest long slit available at the time of the observation, the 5.0$''$ slit, which caused the spectral resolution to be seeing limited to roughly $R \sim 1000$. We read out the two Marconi CCD detectors in the fastest available, 500 kHz read out full-frame mode. The standard 2×2 binning resulted in less than 10 seconds closed-shutter time between the exposures. Exposure time was 60 seconds.

We chose a rotation angle of the instrument which allowed to center both the target HAT-P-19 and the reference star GSC-0228301197 (USNO-B1 1246-0009792) in the slit for simultaneous observations. OSIRIS covers its field of view with two CCD chips, we placed both objects on chip 1 to avoid potential differences between chip 1 and chip 2 as error sources in the differential spectrophotometry.

Observing log

The transit observation was conducted on January 10, 2012. The target was observed for a little less than five hours from 19:33 to 00:19 UT, resulting in 238 exposures. Typically, we reached a S/N ratio of ~ 380 per pixel in dispersion at central wavelengths. The transit lasted from 19:56 to 22:39 UT (first to fourth contact). The night was photometric with the seeing varying from $0.9''$ to $1.3''$. Nevertheless, the observing conditions have been far from optimal for high precision spectrophotometry. The observation began shortly after the meridian passage of HAT-P-19 which happened very close to the zenith. Unfortunately, the dome construction of the GTC could not be fully opened at the time of the observation, causing vignetting at the highest elevations. This vignetting was different for target and comparison star, clearly distracting the transit light curve (Figure 3.3) during pre-transit phase. Moreover, the target set quickly during the time series to a maximum airmass of 3.23, leading to a rapid spread of the point spread function with time. In Figure 3.1 the evolution of the flux level, airmass, FWHM and detector position relative to its mean is shown. The point spread function became asymmetric at about half the observing time due to a loss of focus, the observations were not stopped for focus adjustment to avoid further systematics introduced by an abrupt change of the telescope settings. Therefore the obtained values for the FWHM and pixel position need to be treated with caution because they were derived fitting a Gaussian function to the spatial spectral profile. However, the guiding system kept the spectrum almost at the same position during the entire time series, it moved in spatial direction by less than one pixel. Two jumps in pixel position occurred which were of subpixel value and had no effect on the resulting light curves.

Data reduction

The OSIRIS data were reduced by routines written in ESO-MIDAS. Standard calibration frames have been obtained at the same day as the science observations. Flatfield frames were exposed through the $5''$ wide long slit, the same slit used for the science frames. However, calibration spectra of HgAr and Ne lamps have been taken with a $1''$ wide slit to avoid impractically broad lines. A bias subtraction of the flat, arc lamp and science frames has been performed using the overscan regions. The flatfield correction was done by a master flat created of the flux-weighted average of 101 single flatfield frames taken the same day. We noticed that the flatfield correction had almost no effect on the quality in terms of scatter on the final transit light curves nor on the absolute value of the transit parameters. For example, the difference in the planet-to-star radius ratio k whether a flat field correction was applied or not was about 10 percent of the derived $1\,\sigma$ uncertainty.

Prior to the wavelength calibration we corrected for a drift of the spectra in dispersion direction of about 1.4 pixel over the length of the time series. The origin of such drift is most probably a combination of telescope flexure, obvious in a shift of the skylines by a total of about 0.4 pixel, and a drift of the chromatic centroids of the objects in the long slit, probably caused by field rotation residuals and differential atmospheric refraction (OSIRIS does not include an atmospheric dispersion corrector). For simplicity we corrected for the drift achromatically. A difference in drift among the two objects has only been found for

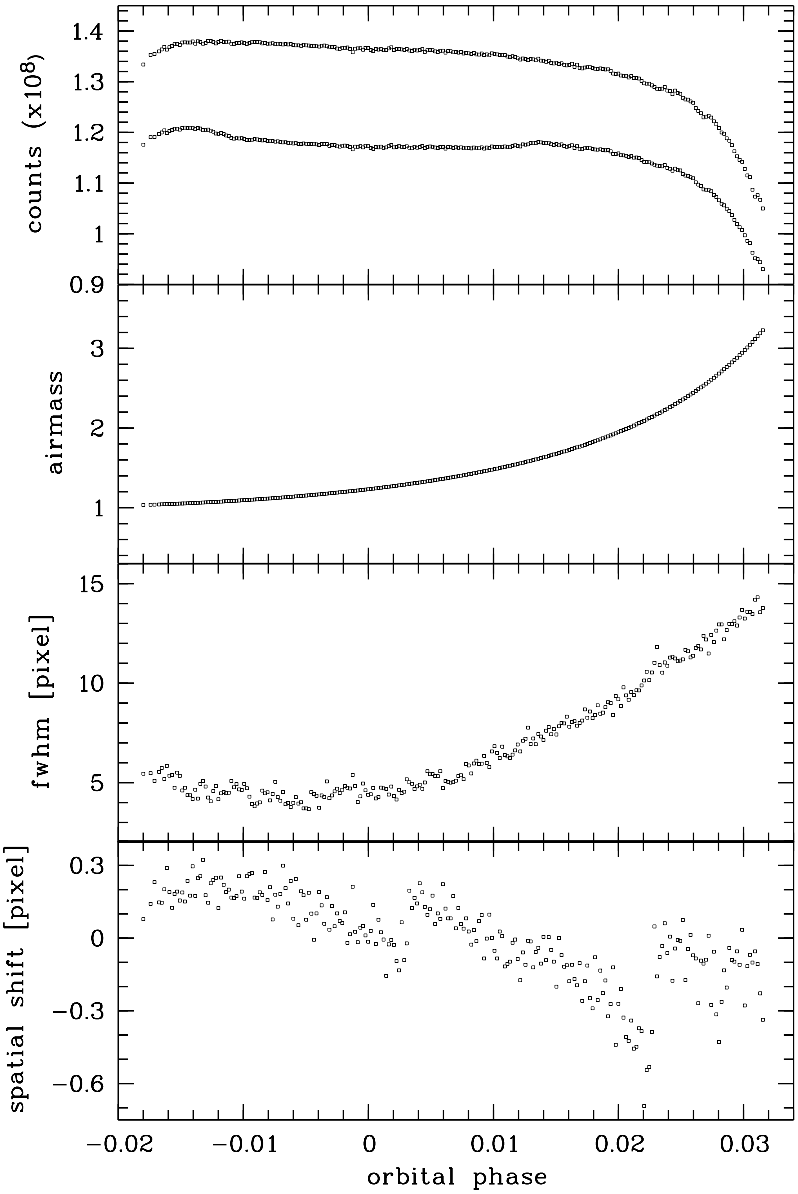

Fig. 3.1. Evolution of observational parameters over the time series. From top to bottom: count rate of target (lower flux level) and reference star (higher flux level) in ADU integrated over the spectral range, airmass, FWHM in spatial direction at central wavelength in pixel, spectrum displacement in spatial direction in pixel.

very high airmass, data which will be excluded in the later analysis (see Section 3.3.1), hence we applied the same drift correction over the entire spatial range. In the through slit acquisition image, taken in the Sloan r band, we measured a slight mismatch of the object centroids in dispersion of ∼ 0.4 pixel (∼ 0.1″), which we also corrected for after the wavelength calibration and spectral extraction. In summary, we estimate the wavelength calibration to be accurate to about 0.5 Å due to residual wavelength dependent shifts and stresses over time both in dispersion and spatial direction.

In the presence of curved sky emission lines we decided for a 2-dimensional wavelength calibration of the whole frame to allow for sky estimation in spatially extended stripes distant to the spatial center of the object. While the choice of the sky stripe width minimized the light curve scatter by up to 10% dependent on the wavelength region, it influenced the absolute transit parameters always by less than their $1\,\sigma$ error values and did not affect the derived transmission spectrum either. The final width of the sky stripes spatially above and below the spectrum was 100 pixel each. The stripes were separated from the object extraction stripe by a 50 pixel gap due to the very extended wings of the spectral profile. The sky value at the object position was estimated by a linear interpolation between these two sky stripes, done for each pixel in dispersion direction independently.

The widths of the aperture in which to extract the object flux were chosen to scale with the spatial FWHM of the spectral profile to account for the immense expansion of the point-spread-function at higher airmass (Figure 3.1). A set of scaling factors have been tested to minimize the scatter in the white light curve. The final aperture size was 7.5 times the FWHM, which ranges from 25 to 105 pixel within the time series. Different widths of the sky stripes were tested, too. The scatter of the white light curve decreased slowly with increasing width until it reached a plateau at about 100 pixel. We tried if the optimal extraction technique of Horne (1986) could further minimize the dispersion on the light curves, but as expected for very high S/N spectra there was no significant difference to a simple flux sum in spatial direction. Instead, the simple flux sum yielded more robust results in the few regions with hot/dark pixels. The 1-dimensional spectra have been extracted in pieces of 10 Å wide steps to account for the wavelength dependent FWHM of the spectral profile. Afterwards the pieces have been stitched together in wavelength, forming spectra from 5617 to 7687 Å. The spectra of exposure 1 are shown in Figure 3.2.

The spectra were then divided in wavelength channels of a certain width (see Figure 3.2 and Section 3.3.4). For each channel the flux of both objects, target and comparison star was integrated and used to perform differential photometry. In this way a set of simultaneously observed light curves consecutive in wavelength was achieved. Individual photometric errors were estimated by

$$\Delta F = \frac{\sqrt{A\,\sigma^2 + \frac{F}{g}}}{F}\,, \tag{3.1}$$

with A as the area (in pixel) over which the total flux F (in ADU) was summed, σ the standard deviation of noise (in ADU) estimated in the two sky stripe areas, and g the detector gain of $g = 1.46\,e^-/\mathrm{ADU}$. This equation follows the photometric error estimation of the software package Source Extractor[1] (Bertin & Arnouts 1996).

3.2.2 Photometric STELLA WiFSIP monitoring

Instrument setup

We observed HAT-P-19 with the wide field imager WiFSIP of the robotic 1.2m twin-telescope STELLA on Tenerife (Strassmeier et al. 2004; Weber et al. 2012). WiFSIP consists of a 4k×4k back-illuminated CCD with a plate scale of 0.322 "/pixel and four read out amplifiers. It covers a field of 22 by 22 arcminutes on the sky. The automatic scheduler of STELLA was set to observe HAT-P-19 in average every second night in blocks of three exposures in V and three exposures in I of 20 seconds exposure time each. We obtained 324 frames within 35 different observing nights from December 2011 to February 2012, between May 2012 and October 2012 the dataset contains of 1268 frames from 82 nights.

---

[1] www.astromatic.net/software/sextractor

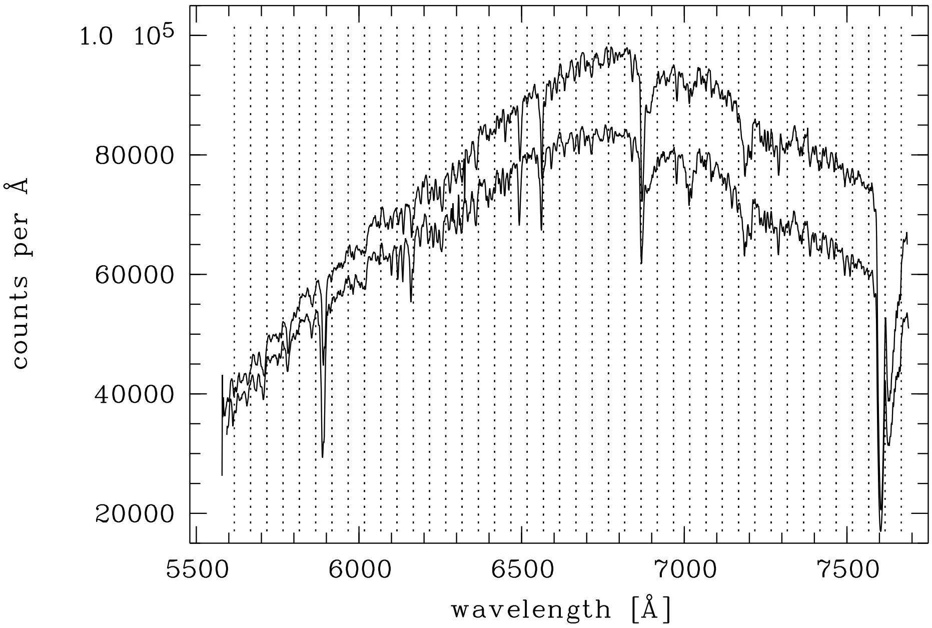

Fig. 3.2. Spectra of HAT-P-19 (lower flux level) and the comparison star (higher flux level) of the first exposure. The 50 Å wavelength channels used for spectrophotometry are indicated by vertical dotted lines.

Data reduction

The bias and flatfield correction was done with the STELLA data reduction pipeline, for details see Granzer et al. (in preparation). The following reduction steps were done with routines written in ESO-MIDAS. We conducted aperture photometry with the software package Source Extractor. Its MAG_AUTO option calculates an elliptic aperture individually to each image and object according to the second order moments of the object's light distribution. This method provides the flexibility to account for the varying observing conditions over the 10 month observing time. The I band data suffered from fringing, whose pattern was found to depend mainly on CCD detector temperature. We created master fringe maps by averaging the individual object-removed and smoothed science frames in groups of the same CCD temperature. The fringe correction was done by the subtraction of the temperature-selected master fringe map, scaled in amplitude to match the fringes of the individual science frames. Typically, the fringe residuals had a strength of about 20% of the original fringe pattern.

We used the method of optimal weighting of an ensemble of comparison stars (Broeg et al. 2005) to form an artificial reference for differential photometry. We experimented with many different comparison star ensembles to verify that the observed photometric signal is independent of the choice of the comparison stars. The final ensemble is formed by three stars similar in brightness and color to HAT-P-19, read out through the same amplifier as the target. The same ensemble was used for the V band and the I band data. After averaging the three consecutively taken data points and subtracting a transit model using the transit parameter derived in Section 3.3.1 and 3.3.3, the point-to-point scatter of the data versus a sine model (see Section 3.3.5) was about 2.5 mmag in both filters.

3.3 Analysis and results

We model and analyze all transit light curves using JKTEBOP (Southworth et al. 2004). The main parameters of the fit are the inclination i, the transit midpoint T_0, the LDC of a quadratic law u and v, and the sum and ratio of the fractional planetary and stellar radius, $r_p + r_\star$ and $k = r_p/\star$, where $r_p = R_p/a$, $r_\star = R_\star/a$, a is the semi-major axis of the planetary orbit and R_p and $R_\star$ are the absolute planetary and stellar radii, respectively.

3.3.1 Detrending and white light curve analysis

A white light curve was formed by an integration of the flux of the entire spectral range. As a very first step, we excluded the first 20 data points which lost flux because of the obscuration of the primary mirror by the dome construction. Unfortunately, these data formed our pre-ingress measurements. The resulting light curve features obvious smooth deviations from a theoretical symmetric transit light curve, see Figure 3.3. For a modeling of this deformation we tested low-order polynomials to the external parameters time, airmass z, sky background, FWHM in spatial direction, pixel shift in x (dispersion direction) and pixel shift in y (spatial direction) and their combinations. The pixel shift in spatial direction was measured by the fit of a Gaussian function to the spatial profile, the measurement of the pixel shift in dispersion was taken as the average of the centroid of six spectral features per object. The detrending function was not simultaneously fitted to the transit model because JKTEBOP does not accept external parameters others than time as input. Our approach was the iteration between a transit fit and a fit of a low-order polynomial to the residuals. With the low-order polynomial the original differential light curve was detrended and a transit fitted again. The fit parameters of the transit model were the fractional radii sum $r_p + r_\star$, the fractional radii ratio k , the inclination i and the transit midtime T_0. The excentricity and longitude of periastron was fixed to the values of H11. When the polynomial coefficients converged and the iteration loop finished after typically a few hundred steps, a $3\,\sigma$ clipping was applied to the residuals and the iteration was performed a second time.

To avoid overfitting of the deformations/trends in the light curve, we choose the function that minimized the Bayesian Information Criterion (BIC, Schwarz 1978). The BIC is similar to the goodness of a fit estimation with a chi-square calculation, but adds a penalty term for the number of parameters in the model,

$$BIC = \sum \frac{(R-P)^2}{\sigma^2} + m \cdot \ln(n) \tag{3.2}$$

with R in our case as the residuals of the observation minus the transit model, P as the detrending function, m the number of free parameters of the detrending function, σ the photometric error of the individual data points and n the number of data points, here 175. We expect Equation 3.1 to underestimate these values because of its ignorance of correlated noise. Therefore, we calculated a scaling factor so that the mean photometric error matches the standard deviation of the photometric points. For the estimation of this factor, we used only the post-transit data (orbital phase > 0.015) to avoid any bias introduced by a premature transit modeling. Afterwards, the BIC values for the tested low-order polynomials were calculated on the entire time series. Table 3.1 gives these values for a selection of tested detrending functions together with their derived transit parameters, which depend significantly on the choice of the detrending function. The final choice was a 3rd order polynomial with the airmass as independent variable because it minimized the BIC value, the scatter of the residuals (rms) and the amount of residual time-correlated noise (estimated by the β value, see Section 3.3.2).

Table 3.1. Dependence of the derived transit parameters on the model function used for detrending. The notation $p(j^i)$ refers to a polynomial of degree i of parameter j, e. g. $p(z^3)$ denotes a polynomial of third degree with respect to airmass z. The model function used for the final light curve analysis is printed in bold face.

model function	BIC	rms (mmag)	β	$k = r_p/r_\star$	$r_p + r_\star$	i (deg)
$p(z^4)$	289.6	0.40	1.03	0.0842 ± 0.0011	0.1403 ± 0.0011	89.96 ± 0.45
$\boldsymbol{p(z^3)}$	**277.9**	**0.40**	**1.08**	**0.0839 ± 0.0011**	**0.1385 ± 0.0012**	**89.77 ± 0.47**
$p(z^2)$	332.9	0.46	1.46	0.0824 ± 0.0017	0.1324 ± 0.0022	89.94 ± 0.71
$p(z^3) + p(x^1)$	290.9	0.40	1.09	0.0838 ± 0.0012	0.1383 ± 0.0012	89.84 ± 0.47
$p(z^3) + p(y^1)$	290.4	0.40	1.10	0.0839 ± 0.0011	0.1385 ± 0.0013	89.81 ± 0.49
$p(z^2) + p(t^2)$	343.3	0.44	1.38	0.0826 ± 0.0019	0.1331 ± 0.0017	89.94 ± 0.66
$p(t^4)$	300.3	0.41	1.03	0.0846 ± 0.0013	0.1401 ± 0.0013	89.96 ± 0.57
$p(t^3)$	318.3	0.44	1.35	0.0825 ± 0.0016	0.1329 ± 0.0020	89.99 ± 0.66
$p(t^2)$	312.8	0.44	1.34	0.0829 ± 0.0018	0.1347 ± 0.0019	89.81 ± 0.71
$p(FWHM^4)$	335.8	0.44	1.63	0.0829 ± 0.0023	0.1328 ± 0.0021	89.53 ± 0.99
$p(FWHM^3)$	394.5	0.49	1.79	0.0824 ± 0.0024	0.1319 ± 0.0025	89.81 ± 1.16

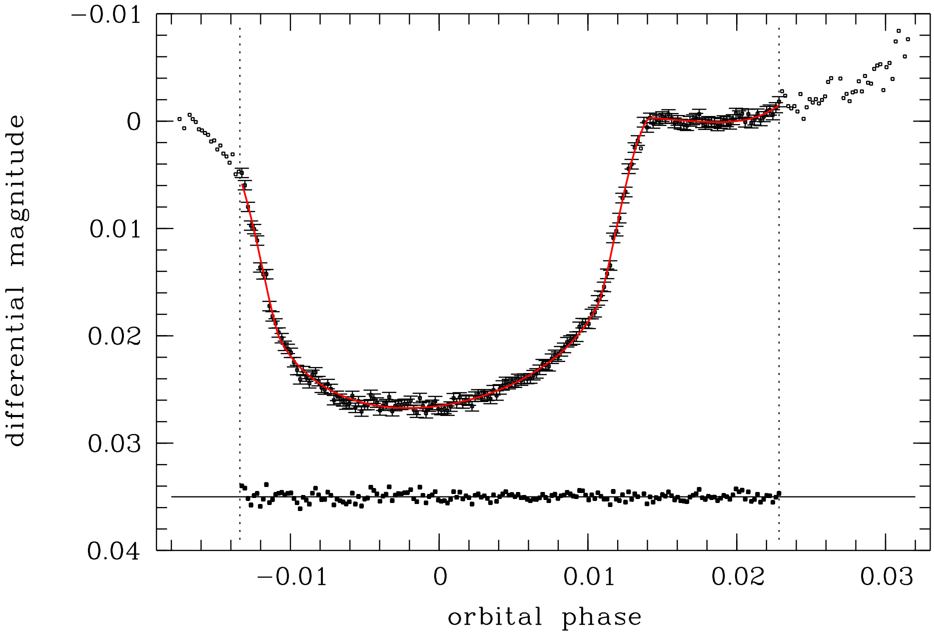

Fig. 3.3. Transit light curve integrated over the entire spectral range (white light). The vertical dashed lines confine the data which have been used for the analysis, see text for details. The red solid line shows the best fit model, the residuals are presented at the bottom.

An additional remark should be made regarding the iterative transit/trend fitting. The analysis described here in Chapter 3 of HAT-P-19b was submitted to the Journal *Astronomy & Astrophysics*. The anonymous referee mentioned the iterative fitting approach as to be unusual and suggested a simultaneous transit fit plus detrending. We performed additional tests to show that our fitting approach does not modify the results: JKTEBOP accepts only time as input parameter next to magnitude and magnitude error. However, it provides the option of a simultaneous detrending with a polynomial over time. Therefore, we compared the results of a simultaneous transit fit plus a detrending using a 3rd order polynomial over time with the results using the same detrending function in the iterative fitting. We repeated the test also with a 2nd and 4th order polynomial over time as detrending function. The results of simultaneous and iterative fit approach were in agreement to a fraction of the derived $1\,\sigma$ uncertainties. Typically, the deviation was between 0.05 and 0.2 times the uncertainty value, the maximum deviation we encountered was 0.35 times the uncertainty. Hence, we conclude that the iterative fitting approach, necessary to combine the JKTEBOP transit fit with a detrending polynomial with airmass as independent variable, does not modify the final result.

The stellar limb darkening was approximated by the quadratic law in the transit fit, see Section 2.3 for a related argumentation. The limb darkening coefficients (LDC) have been spherically calculated for a star of $T_{\mathit{eff}} = 5000$ K and log $g = 4.5$ in high spectral resolution using PHOENIX stellar atmosphere models of metallicity log[M/H] = 0.0, see Claret et al. (2013a) for details. The applied values for the white light curve were found by a flux-weighted average of these nearly monochromatic values. In the analysis of the white light curve we fitted for the linear LDC u and fixed the non-linear term v to the theoretical value. The fitted value of the linear term was in agreement with the prediction within about $1\,\sigma$. In the estimation of the transit parameter uncertainties (see Section 3.3.2) the non-linear LDC v was perturbed in an interval of 0.1 on a flat distribution. This approach of fitting u but fixing v to its theoretical value allows for some flexibility to account for potential systematic differences between the star and its theoretical model spectrum used for determination of the limb darkening parameters. Furthermore, it avoids the problem of enlarged uncertainties when fitting for both coefficients caused by the strong correlation between u and v (Southworth et al. 2007a; Southworth 2008; Johnson et al. 2008).

We make a short note on the systematic error introduced by the metallicity difference between the PHOENIX models (solar metallicity) and HAT-P-19: H11 derived a value of log[M/H] $= 0.23 \pm 0.08$. We used the limb darkening tables of Claret (2000) and Claret (2004) to estimate the systematic error to be on the order of 0.005 for the quadratic LDC (the linear coefficient is a free parameter in our transit fit). This value is very small compared to our pertubation interval of 0.1, therefore the introduced systematic error is much smaller than the derived transit parameter uncertainties.

There are features in the noise in the post-transit light curve at phases later than about 0.023 visible to the eye which are believed to be systematics potentially caused by differential slit loss. In case of only white noise the uncertainty of the radius ratio k should *decrease* approximately proportionally to the square root of the number of out-of-transit (OoT) data. Here it was worth trying if the uncertainties actually decrease with *fewer* OoT data. And indeed, the uncertainty of the radius ratio Δk reached a minimum at an OoT limit of phase 0.0228 (see Section 3.3.2 for their derivation). Also the uncertainties of the sum of radii $\Delta(r_p + r_\star)$, the inclination Δi and the transit midtime ΔT_0 reached their minima at about this number of OoT data, therefore we discarded all later phases from the analysis.

The results of the white light curve analysis are given in Table 3.2 together with an estimation of the surface gravity of the planet g_p, calculated with Equation 2.9 using the value of the stellar velocity amplitude K from H11.

3.3.2 Error estimation of the transit parameters

For an estimation of the transit parameter uncertainties we run a MC simulation of 5000 steps and a residual-permutation algorithm. Details of both methods are explained in Section 2.2. The uncertainty of the detrending function is included in the error estimation because each MC step consisted of a new iteration between detrending and transit fit as described in Section 3.3.1. From the distribution of these 5000 best fit parameters the $1\,\sigma$ uncertainties of the white light curve transit parameters are drawn as the 68.3% of highest probability. For reliable photometric error bars we rescaled them with a common factor to give $\chi^2_\nu = 1.0$. Afterwards, we calculated the β factors as discussed in Section 2.2 to further inflate the photometric errors and account for correlated noise in the light curves. The β factors were obtained by binning the light curve residuals in intervals from 10 to 20 minutes (about the duration of ingress) in 1 minute steps (original time sampling is $\sim$1.1 minute). We derived the factor in each case and formed their average as final values used to enlarge the individual photometric errors. All averaged β values are listed in Table 3.3. We adapted the higher parameter error bar of the MC analysis and the residual-permutation algorithm as our final transit fit uncertainty presented in Table 3.2.

Table 3.2. Transit fit parameter of the white light curve.

Parameter	Value
$r_\star$	0.07373 ± 0.00109
r_p	0.01019 ± 0.00022
$r_p + r_\star$	0.08392 ± 0.00113
k	0.13854 ± 0.00121
i [deg]	89.77 ± 0.47
T_0 - 2400000 [days]	55937.38835 ± 0.00010
u	0.5707 ± 0.0158
v (fixed)	0.1376
g_p [ms^{-2}]	7.30 ± 0.49

3.3.3 Ephemeris

We used the white light curve of our transit measurement and the publically available two complete transits from H11, observed with the KeplerCam camera on the FLWO 1.2m telescope, to recalculate the ephemeris. The FLWO transits were re-analyzed with our algorithms to guarantee consistency in the analysis. A first order polynomial over time was fitted iteratively to the residuals of the transit model fit with JKTEBOP. The free transit parameter was the midtime of the transit T_0. $r_p + r_\star$, k and i were fixed to the values derived from our white light curve, given in Table 3.2. The quadratic LDC were fixed to the values used by H11. The results of the transit midtimes are summarized in Table 3.4 and graphically presented in Figure 3.4. We experimented with the coefficients, using the linear coefficient as free fit parameter or varying both in meaningful ranges. The tests showed very little effect of very few seconds on T_0, which is well inside the errors. The error values were calculated with the JKTEBOP MC simulation of 5000 steps after an enlargement of the individual photometric errors by the β factor, identically to our white light curve analysis described in Section 3.3.1. H11 used the Coordinated Universal Time (UTC) as time base for their BJD calculations. As recommended by Eastman et al. (2010) we converted all times to the Barycentric Dynamical Time (TDB) using their available

Table 3.3.: Characteristics of the extracted transit light curves.

Wavelength (Å)	β	rms (mmag)	u fitted	v calculated	$k = r_p/r_\star$
5617 - 7616	1.06	0.40	0.5705	0.1376	0.1385 ± 0.0012
5617 - 5816	1.09	0.71	0.6047	0.0988	0.1362 ± 0.0019
5817 - 6016	1.03	0.68	0.6141	0.1132	0.1388 ± 0.0015
6017 - 6216	1.12	0.62	0.6202	0.1230	0.1386 ± 0.0015
6217 - 6416	1.00	0.67	0.5947	0.1258	0.1390 ± 0.0013
6417 - 6616	1.02	0.69	0.5634	0.1450	0.1404 ± 0.0013
6617 - 6816	1.09	0.60	0.5784	0.1442	0.1384 ± 0.0013
6817 - 7016	1.17	0.63	0.5737	0.1495	0.1379 ± 0.0018
7017 - 7216	1.00	0.65	0.5505	0.1443	0.1383 ± 0.0013
7217 - 7416	1.00	0.56	0.5154	0.1529	0.1386 ± 0.0011
7417 - 7616	1.00	0.56	0.5043	0.1570	0.1384 ± 0.0011
5617 - 5666	1.17	1.19	0.6087	0.0989	0.1324 ± 0.0030
5667 - 5716	1.00	1.12	0.5708	0.0969	0.1397 ± 0.0022
5717 - 5766	1.19	1.12	0.5799	0.0921	0.1401 ± 0.0028
5767 - 5816	1.00	0.94	0.6054	0.1068	0.1373 ± 0.0019
5817 - 5866	1.00	0.91	0.6230	0.1204	0.1371 ± 0.0018
5867 - 5916	1.08	1.02	0.6008	0.0930	0.1393 ± 0.0022
5917 - 5966	1.00	1.04	0.6425	0.1118	0.1367 ± 0.0021
5967 - 6016	1.00	1.04	0.5833	0.1246	0.1394 ± 0.0020
6017 - 6066	1.00	1.04	0.6169	0.1278	0.1401 ± 0.0021
6067 - 6116	1.18	1.03	0.6310	0.1158	0.1366 ± 0.0024
6117 - 6166	1.21	1.21	0.6064	0.1221	0.1406 ± 0.0028
6167 - 6216	1.00	0.95	0.5917	0.1263	0.1397 ± 0.0019
6217 - 6266	1.00	0.90	0.5613	0.1246	0.1419 ± 0.0018
6267 - 6316	1.08	0.96	0.5985	0.1248	0.1375 ± 0.0021
6317 - 6366	1.00	1.11	0.5898	0.1307	0.1373 ± 0.0023
6367 - 6416	1.01	0.97	0.5748	0.1232	0.1405 ± 0.0020
6417 - 6466	1.00	0.84	0.5633	0.1225	0.1396 ± 0.0016
6467 - 6516	1.00	0.91	0.5800	0.1352	0.1416 ± 0.0018
6517 - 6566	1.26	0.92	0.5474	0.1703	0.1387 ± 0.0023
6567 - 6616	1.02	1.02	0.5441	0.1510	0.1379 ± 0.0020
6617 - 6666	1.21	1.02	0.5606	0.1415	0.1390 ± 0.0026
6667 - 6716	1.26	0.92	0.5817	0.1419	0.1373 ± 0.0024
6717 - 6766	1.19	0.83	0.5646	0.1483	0.1401 ± 0.0018
6767 - 6816	1.00	0.79	0.5917	0.1450	0.1383 ± 0.0014
6817 - 6866	1.00	0.91	0.5380	0.1472	0.1385 ± 0.0024
6867 - 6916	1.37	0.94	0.5525	0.1533	0.1404 ± 0.0031
6917 - 6966	1.00	1.00	0.6017	0.1484	0.1370 ± 0.0024
6967 - 7016	1.17	1.01	0.5375	0.1492	0.1401 ± 0.0023
7017 - 7066	1.00	1.46	0.4979	0.1421	0.1371 ± 0.0030
7067 - 7116	1.00	0.87	0.5514	0.1498	0.1383 ± 0.0017
7117 - 7166	1.07	1.13	0.5175	0.1434	0.1413 ± 0.0022
7167 - 7216	1.00	1.30	0.5635	0.1414	0.1382 ± 0.0027
7217 - 7266	1.01	0.93	0.5100	0.1494	0.1400 ± 0.0023
7267 - 7316	1.00	0.82	0.4700	0.1568	0.1403 ± 0.0015
7317 - 7366	1.00	0.89	0.4935	0.1527	0.1380 ± 0.0018
7367 - 7416	1.00	0.90	0.5588	0.1530	0.1344 ± 0.0018
7417 - 7466	1.00	0.94	0.4962	0.1578	0.1390 ± 0.0018
7467 - 7516	1.00	0.79	0.5019	0.1572	0.1384 ± 0.0016
7517 - 7566	1.00	0.83	0.4743	0.1602	0.1381 ± 0.0017
7567 - 7616	1.00	1.00	0.5035	0.1510	0.1394 ± 0.0019

Table 3.3.: continued

Wavelength	β	rms	u	v	$k = r_p/r_\star$
7617 - 7666	1.00	0.95	0.5126	0.1543	0.1365 ± 0.0019
5667 - 5866	1.01	0.62	0.6018	0.1046	0.1375 ± 0.0015
5867 - 5916	1.08	1.02	0.6008	0.0930	0.1393 ± 0.0022
5917 - 6516	1.14	0.52	0.5892	0.1243	0.1403 ± 0.0014
6537 - 6587	1.17	0.99	0.5409	0.1727	0.1397 ± 0.0022
6587 - 7666	1.06	0.42	0.5282	0.1492	0.1388 ± 0.0013

online tools[2]. The newly found ephemeris is

$$T_c \,=\, \mathrm{BJD(TDB)}\, 2455909.326807(59) \,+\, 4.0087839(15)\, N. \tag{3.3}$$

T_c is the predicted central time of a transit, N is the cycle number with respect to the reference midtime and the numbers in brackets give the uncertainties of the last two digits. The reference midtime was chosen to minimize the covariance between reference midtime and period. The GTC transit corresponds to cycle number 7, accordingly.

We tested if additional transit light curves observed by amateur astronomers could further improve on the accuracy of the ephemeris. The data were made publically available on the Exoplanet Transit Database (ETD) website[3]. We selected the ETD transits to have uncertainties on the transit midtime T_0 of about one minute or less. The light curves were re-analyzed and the transit midtimes converted into BJD(TDB). However, we found that the time uncertainties of the eight ETD transits are too large to improve significantly on the ephemeris of Equation 3.3. Therefore, we decided to only use the better documented and peer reviewed observations of H11 and our own observation. The timings of ETD are in rough agreement with Equation 3.3, see Figure 3.4, their residuals are all consistent with zero within less than $3\,\sigma$.

3.3.4 Transit depth as a function of wavelength

We created two different chromatic sets of light curves by binning the flux of our spectra in wavelength channels of a certain width. At first, we chose 200 Å as channel width, giving rather high signal to noise per photometric data point, but a poor spectral resolution in our resulting transmission spectrum. At second, we binned the flux in narrower channels, providing a higher spectral resolution on the cost of noisier light curves and therefore higher uncertainties of the transit parameter. We performed a simple estimation of the channel width most sensitive for narrow spectral features by the help of a theoretical 1000 K transmission spectrum (Fortney et al. 2010). We compared the theoretically predicted transit depth in a channel centered at the Na D line core with the transit depths in the adjacent channels for channel widths of 10 to 150 Å. The derived function of differential transit depths over channel width was weighted with a simple square root law to account for the signal to noise dependence on the width. For simplicity we assumed here photon noise to dominate the noise budget. The resulting function peaks at about 50 Å. Figure 3.5 shows the light curve set of 200 Å channel width. In the left column the raw light curves are shown, in the middle column the detrended light curves, and in the column to the right the residuals versus the detrend + transit model.

---

[2] http://astroutils.astronomy.ohio-state.edu/time/

[3] http://var2.astro.cz/ETD/

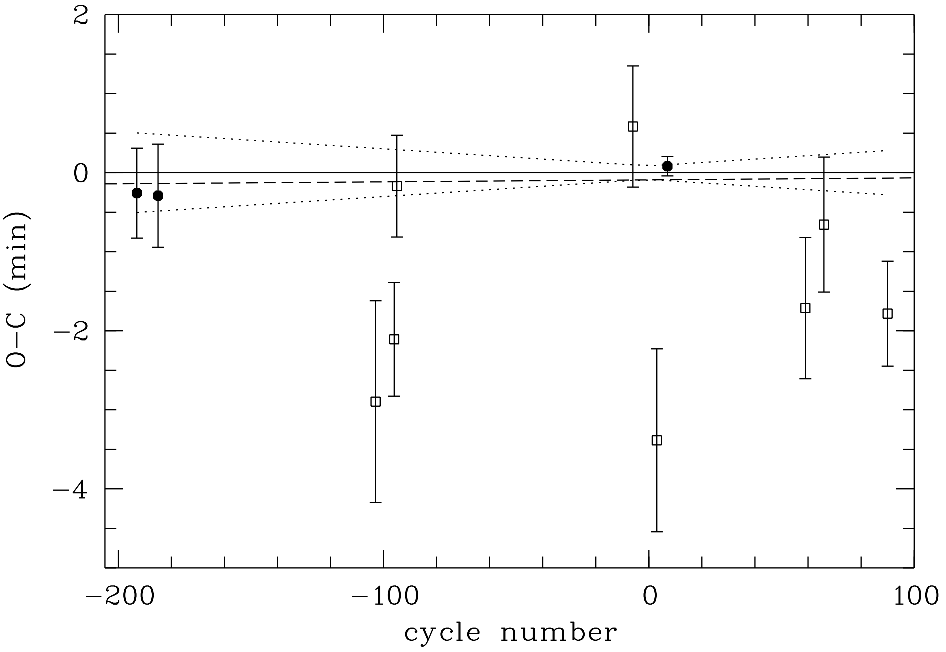

Fig. 3.4. Transit timing residuals versus the linear ephemeris of Equation 3.3. The filled symbols represent the two transits of H11 and the transit of this work, which were used to derive the ephemeris. The open symbols show the amateur ETD transits. The dotted lines give the 1 σ uncertainty of the ephemeris as a function of cycle number. The dashed line shows the difference when the amateur data are included in the ephemeris fit, which yielded no significant improvement and was finally not used for Equation 3.3.

Table 3.4. Transit midtimes of HAT-P-19b and their residuals versus the ephemeris derived in this work. The upper part gives values for professional light curves, used to derive the ephemeris. The lower part gives values for amateur light curves (ETD/TRESCA), tested in the analysis, but finally not used to derive the ephemeris.

Midtime T_0 (BJD(TDB) - 24000000)	Cycle number	Residual (min)	Reference
55135.63133 ± 0.00040	-193	-0.00017	Hartman et al. (2011a)
55167.70158 ± 0.00045	-185	-0.00020	Hartman et al. (2011a)
55937.38835 ± 0.00010	7	0.00005	This work
55496.42005 ± 0.00089	-103	-0.00201	Naves, R
55524.48209 ± 0.00050	-96	-0.00146	Muler, G.
55528.49222 ± 0.00045	-95	-0.00011	Ruiz, J.
55885.27451 ± 0.00053	-6	0.00040	Ayiomamitis, A.
55921.35081 ± 0.00080	3	-0.00235	Naves, R.
56145.84387 ± 0.00062	59	-0.00118	Shadic, S.
56173.90609 ± 0.00059	66	-0.00045	Garlitz, J.
56270.11612 ± 0.00046	90	-0.00123	Zhang, L.

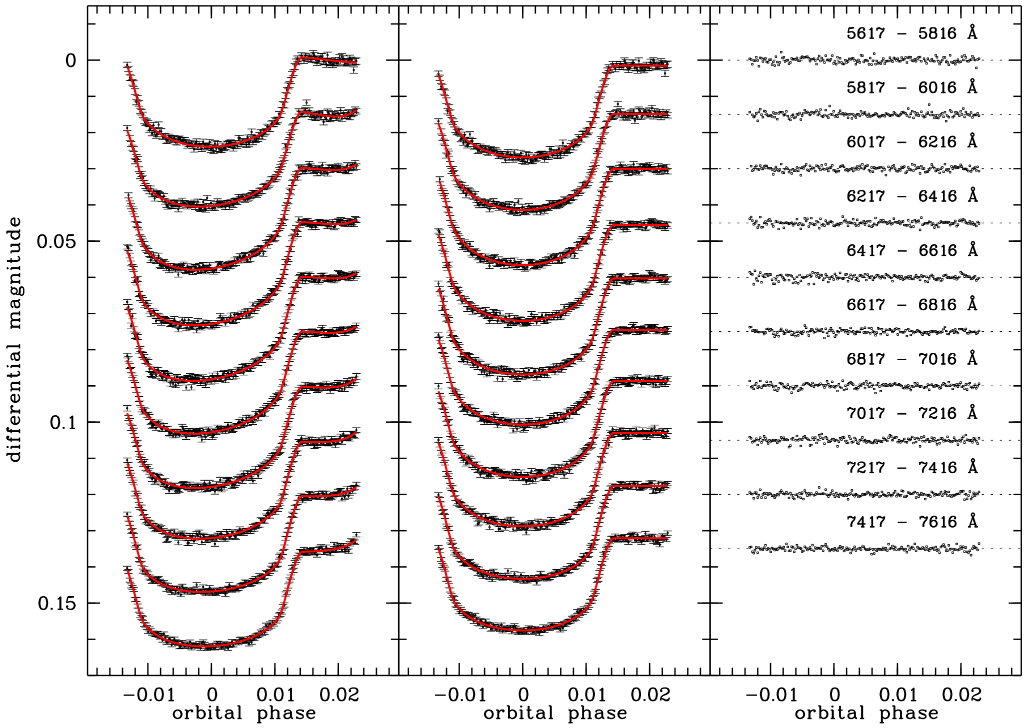

Fig. 3.5. Chromatic set of transit light curves of HAT-P-19b, flux integration done in 200 Å wide flux channels. The left panel shows the raw light curves, the middle panel the detrended light curves and the right panel the light curve residuals.

The analysis of the chromatic set of light curves was the same as it was for the white light curve, see Section 3.3.1, except of a smaller number of free transit parameter. We detrended all light curves with a 3rd order polynomial over airmass, again iteratively to the transit fit made with JKTEBOP. The free transit parameters are the fractional planetary radius r_p and the linear coefficient of the quadratic limb darkening law. The quadratic coefficient was fixed to its theoretical value. The uncertainties of k were derived as explained for the white light curve (see Section 3.3.2), the results are presented in Table 3.3.

The transmission spectrum plotted in Figure 3.6 appears very flat without significant outliers. We calculated the χ^2 of the 50 Å data set versus a Rayleigh-scattering slope given by $dR_p/d\ln\lambda = -4H$ similar to the observed spectrum of HD189733b (Lecavelier Des Etangs et al. 2008a) with H as the atmospheric scale height. We also compared the data to a 1D solar metallicity model using a planet-wide averaged P-T profile computed by Fortney et al. (2010) for the parameters of the HAT-P-19 system, see Figure 3.9. Both models have been binned in the same 50 Å wavelength channels as the observed spectra. The cloud-free model shows a prominent sodium absorption feature with pressure-broadened wings, also predicted by other modeling work for HAT-P-19b's equilibrium temperature of about 1000 K (Seager & Sasselov 2000; Brown 2001; Hubbard et al. 2001). A similar feature of potassium causes the upward slope of planetary size in the model at the red end of our wavelength range, the line core of potassium was not covered, unfortunately. The lowest χ^2 of 30.6 for 40 degrees of freedom is given by a flat line, 35.6 was obtained for the Rayleigh-scattering spectrum and 47.9 for the cloud-free atmosphere.

We tried to test the influence of certain steps of our analysis on the obtained transmission spectrum. For example, we shifted the flux channels in wavelength by fractions of their

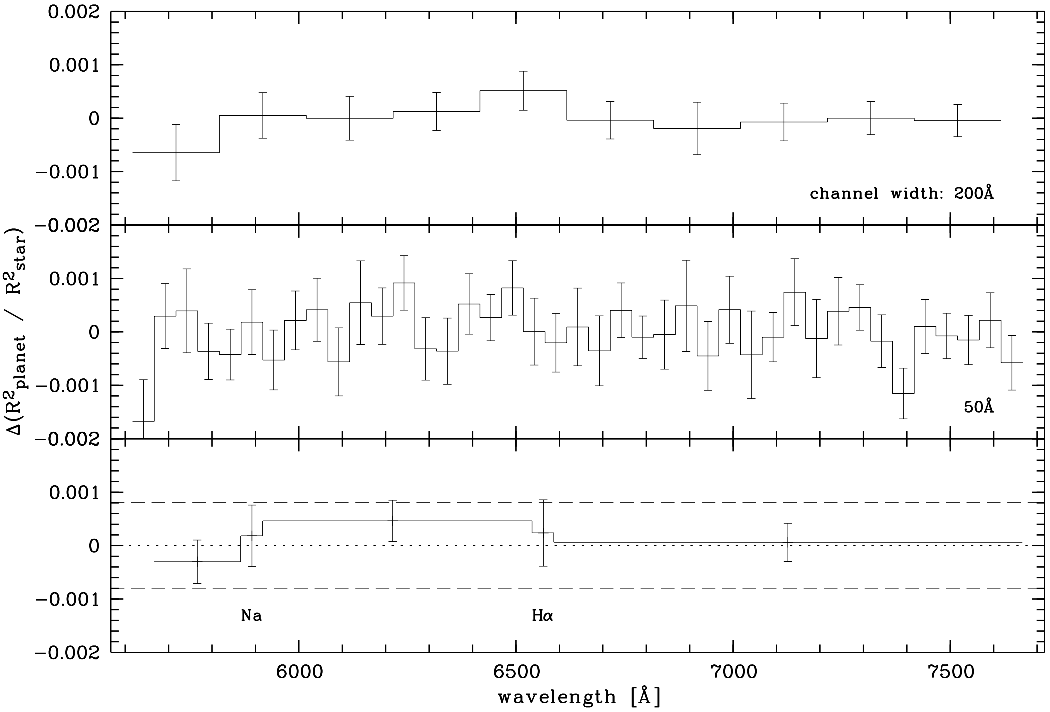

Fig. 3.6. Transmission spectrum of HAT-P-19b. In the upper panel the relativ change in transit depth is shown for 200 Åwide wavelength channels, in the middle panel a channel width of 50 Å is presented. For the lower panel two 50 Å wide channels concentrated on the line center of the Na doublet at ∼5892 Å and Hα at ∼6563 Å. No significant variation was detected. The horizontal dotted line in the lower panel marks the average value, the dashed lines mark the difference corresponding to three atmospheric scale heights.

width, we tested different lengths of post-transit baseline and used other values of $r_\star$ and i, for example the values found by H11. We also varied our treatment of the LDC by fixing both u and v to theoretical values, another time we fitted for both in the transit modeling. No test yielded a significant deviation in spectrum shape from the spectrum presented here in Figure 3.6.

3.3.5 Photometric variability of HAT-P-19

We found a clear periodic variation of HAT-P-19 in the long term photometry shown in Figure 3.7. A least square sine fit to the data revealed a period of 35.5 ± 2.5 days. The error value is drawn from the full width at half maximum of the peak in the periodogram in Figure 3.8. The amplitude was different for the used filters, V and I, with 4.7 ± 0.5 and 3.0 ± 0.4 mmag, respectively, provided by the least square sine fit. There are indications of varying period and amplitude in our data. When analysing only the data of the observing season 2012, we obtain a stronger amplitude of 6.3 ± 0.6 and 4.6 ± 0.5 for V and I and a slightly longer period of 38.6 ± 4.4 days. In the interpretation of the flux variation being caused by starspots rotating in and out of view, these changes in period and amplitude are possibly related to spot evolution. However, the period variation is within one σ and the amplitude variations do not exceed $3\,\sigma$.

The periodogram in Figure 3.8 shows three additional peaks next to the main signal at somewhat shorter period. They loose most of their power or disappear totally when subtracting the most significant signal (pre-whitening). Instead, in the residual data we

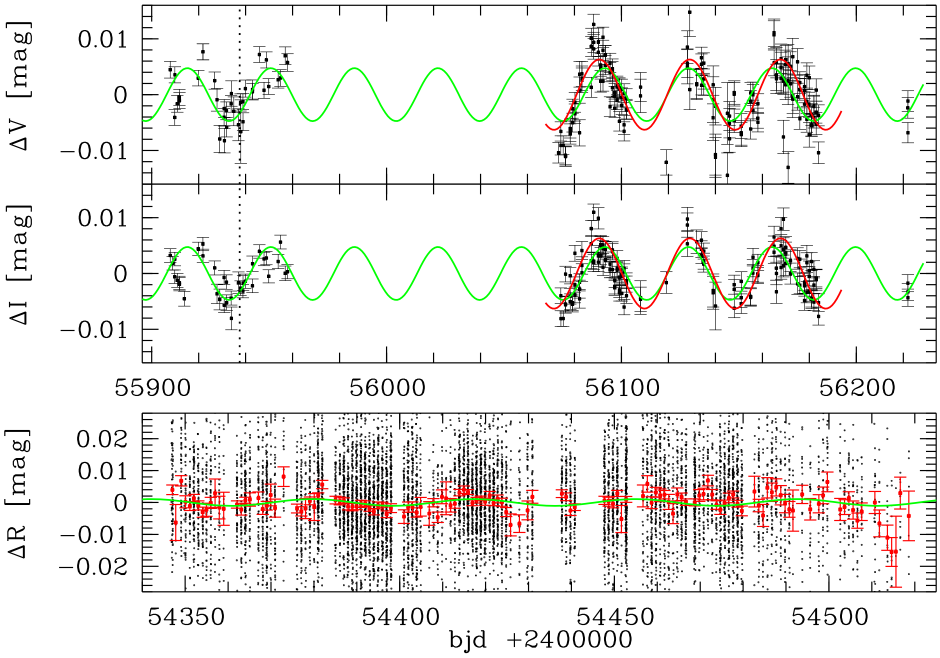

Fig. 3.7. Upper panel: STELLA differential V band photometry. A simple sine model of the 2011+2012 data set overplotted in green, a sine model of only the 2012 data in red. The vertical dotted line marks the transit time of our spectroscopic observation. Middle panel: The same as in the upper panel, here for filter I. Lower panel: The HATnet differential R band photometry from 2007/2008. Black dots are the individual data points, red is the nightly average and green gives the best fit sine model.

find another signal above the false alarm probability of 0.01 at about 23 days. This period might also be related to spot evolution, however an in-depth period analysis is out of scope of the current work.

H11 does not mention a stellar flux variability. In order to look if the periodicity is present in the September 2007 - February 2008 HATnet photometry by which HAT-P-19b was discovered, Joel Hartman kindly provided us with these data. The time series re-analyzed here was already treated by the external parameter decorrelation technique and the Trend Filtering Algorithm, as it is common for HATnet data (see H11 and references therein). When calculating a Lomb-Scargle periodogram, we find a significant period of $P = 37.7 \pm 3.1$ days (false alarm probability < 0.0002), see Figure 3.8. The sine fit reveals a much lower variability amplitude compared to the STELLA data of only 1.0 ± 0.3 mmag.

3.3.6 Correction for starspots

A likely reason for the periodic flux variation of HAT-P-19 are cool spots rotating in and out of view since the variation amplitude is larger in the V band than in the redder I band. Brightness inhomogeneities on the stellar surface influence the transit parameters as explained in detail in Section 2.4. An occultation of a starspot by the transiting planet causes a bump in the light curve, which leads to a shallower transit and an underestimation of the planet size if uncorrected. Starspots unocculted from the planet cause the average brightness to be higher along the transit chord than on the rest of the stellar hemisphere, which leads to deeper transits and an overestimation of the planet size.

The white light curve gives no evidence of a starspot crossing event. Possible scenarios, which allow for spots along the chord without resolvable deformations of the transit shape like very small spots or a homogeneous spot distribution along the chord are considered

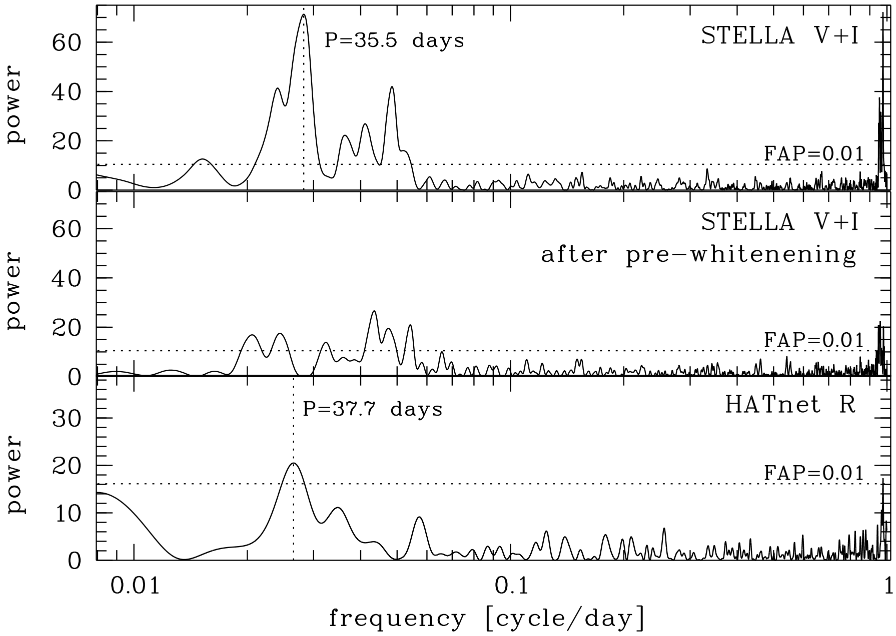

Fig. 3.8. Lomb Scargle periodogram for the STELLA photometry (upper panel) and the HATnet photometry (lower panel). Horizontal dashed lines denote the power value of false alarm probability (FAP) 0.01. Vertical dashed lines mark the period found by the sine fit. The middle panel shows the STELLA periodogram after one pre-whitening step. Significant frequencies remain, which we attribute to the sampling pattern and/or spot evolution.

to either be negligible in their effect or unlikely. We therefore assume that the transit depth is not underestimated. With the long term photometry on hand, we can estimate the influence of unocculted starspots on the stellar hemisphere visible at the moment of the transit event using the formalism introduced in Section 2.4 of this thesis. Mainly, it includes three quantities: The stellar flux level f_{meas} at the time of the transit observation, the stellar flux level without spot dimming f_{quiet} and the effective temperature of the spots T_{spot}. Equations 2.17 and 2.17 translate them into a value for the modification of the transit depth.

A value of the flux variation Δf includes the knowledge of HAT-P-19's flux level f_{quiet} without any spots on its visible surface. It is likely that spots were present also at the time of our light curve's highest count rate, therefore f_{quiet} needs to be estimated. We approximate the level of a permanent flux dimming by the level of the variance of the long term light curve, an approach undertaken by Pont et al. (2013) in the case of HD189733 based on the work of Aigrain et al. (2012). Thus, at the time of our transit observation we estimate $\Delta f \sim -0.007$ in V band. Conservatively, we round this value up to 1% flux dimming by spots.

To estimate Δf over the spectral range covered by our transit observation, a value of the starspot temperature is needed. However, T_{spot} cannot easily be derived by photometric data because of a degeneracy between spot size and spot temperature (Strassmeier 2009). In principle this can be broken by multi-color photometry, but our error bars on the sub-percent variation amplitudes in V and I band cannot reasonably constrain the temperature contrast between spots and photosphere. The starspots of the exoplanet host star HD189733, similar in stellar parameters to HAT-P-19, have temperatures between 750 K (Sing et al. 2011b) and 1000 K (Pont et al. 2008) lower than the spot-free photosphere. In a review article, Berdyugina (2005) lists several early K dwarfs with spots of about 1500 K temperature contrast. We calculated spot corrections on the transmission spectrum for three different temperature contrasts, 500 K, 1000 K and 1500 K. The spectral energy distributions of the spots and spot-free photosphere were simply approximated by black body radiation. Furthermore, we neglect here the contribution of faculae. Under these assumptions a flux dimming of 1 percent corresponds to about 2.3 (1.4, 1.1) percent coverage of the stellar hemisphere with spots of 500 K (1000 K, 1500 K) temperature contrast. The obtained Δk^2 correction values over wavelength range from $\sim 1\%$ of the transit depth ($\Delta k^2 \sim 0.00019$) at the blue end of our spectrum to about 0.8% ($\Delta k^2 \sim 0.00016$) at the red end. The difference in Δk^2 according to the different spot temperatures is at the level of 0.1% transit depth at 7500 Å. Our derived uncertainty of the transit depth k^2 for the white light curve is about 1.7%. Hence, the spot correction on the absolute transit depth is of minor importance and the correction on the relative changes of transit depth over wavelength is negligible.

3.4 Discussion

3.4.1 Discrepancy in the transit parameter

The transit parameters derived in the present work differ from the values obtained by H11. Our best fit transit model implies an inclination of almost 90 degrees, 89.77 ± 0.47, which is discrepant from the literature value by about $3\,\sigma$. While the radius ratio changes just moderately by about $1.5\,\sigma$ to 0.1385, the higher inclination causes both the star and the planet to be smaller than derived by H11. For $r_\star$ and r_p we measured 0.0737 ± 0.0011 and 0.0102 ± 0.0002 in comparison to 0.0817 ± 0.0045 and 0.0112 ± 0.0007 found by H11. The difference in $r_\star$ and r_p is significant to about 2 and $1.5\,\sigma$, respectively. The linear LDC u of the quadratic law, fitted as free parameter, 0.571 ± 0.016, is in agreement to the theoretical value of 0.555 within $1\,\sigma$ confidence. Please note, when fixing the inclination during the transit fit to the value found by H11, $i = 88.2°$, the derived values for $k, r_\star$ and r_p agree with H11 to within $1\,\sigma$. In this case, the residuals give a higher rms (0.47 mmag compared to 0.40 mmag) and a somewhat higher discrepancy of the measured linear LDC towards the theoretical value ($1.6\,\sigma$ compared to $1.0\,\sigma$). We tested fitting and non-fitting both LDC, other detrending functions, including more data points of the out-of-transit time series, but in all cases when including the inclination as free parameter, we derived an inclination very near 90°. We also tested JKTEBOP with simulated data to check if the lack of pre-ingress data might drive the inclination artificially to higher values, but found no confirmation for such trend.

3.4.2 The transmission spectrum

We run a simple calculation to test if any potential variations in transit depth among the narrow wavelength channels could be blurred by the point-spread-function. We assumed the FWHM in dispersion direction to equal the measured FWHM in spatial direction due to the 5” wide slit. While the FWHM increased to more than 10 pixel towards our OoT phase limit of 0.0228, the average value during 2nd and 3rd contact of the transit was 4.8 pixel (1.2” on the sky). The corresponding light leakage weakens a potential difference in transit depth of the sodium 50 Å channel in respect to the adjacent channels by $\sim 3\%$. Hence, we neglect this effect here.

Key values for an initial characterization of an exoplanet atmosphere are the error bars of the relative transit depth measurements. We found the average error value to be higher than the scatter of the k^2 values for both the 50 Å and the 200 Å light curve sets. The reduced χ^2 values of 0.7 and 0.4, respectively, versus a constant k^2 confirm this indicator

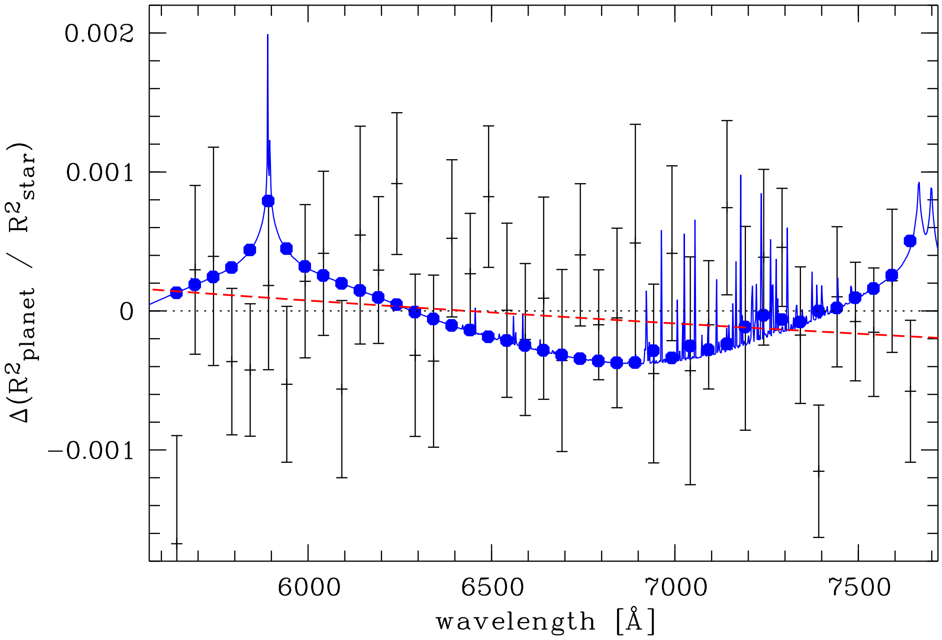

Fig. 3.9. Derived transmission spectrum in comparison to a theoretical spectrum calculated by Fortney et al. (2010) illustrated as continuous blue line. The model values integrated over 50 Å flux channel width are shown in blue filled circles. Also presented is a spectrum typical for Rayleigh-scattering as red dashed line. Both models were computed according to the system parameters of HAT-P-19.

of a slight overestimation of the error bars. We compared our achieved 200 Å accuracy to similar investigations present in the literature by a search for values of ground-based single transit analyses using a comparable width of the flux channels in about the same wavelength range. Please be aware that differences can occur by different telescope size, target brightness, complexity of systematics in the light curves and analysis techniques. However, our average uncertainty of k^2 for the 200 Å channels of 3.8×10^{-4} is in good agreement with the range of literature values $1.8 - 3.4 \times 10^{-4}$ (Gibson et al. 2013a,b; Jordán et al. 2013; Murgas et al. 2014). One reason for our uncertainty to be slightly larger is certainly the lack of out-of-transit baseline on one side.

Our transmission spectrum of HAT-P-19b favors a featureless flat spectrum, but although less likely, the Na rich, cloud-free atmosphere overplotted in Figure 3.9 is not ruled out. If confirmed by follow-up observations, a non-detection of the pressure-broadened Na absorption could be explained in two ways: First, a cloud or haze layer does not allow to probe the deeper layers of the atmosphere and covers the broad alkali line wings. Due to the slant viewing geometry during transmission spectroscopy even condensates of rather low abundance can make the atmosphere opaque (Fortney 2005). Observations of higher spectral resolution would be needed to search for a spectroscopic feature at the line core. The other explanation would be a clear atmosphere with a depletion of atomic sodium. Sodium condensation into clouds of for example sodium sulfide at the planets cooler night side could potentially decrease the amount of atomic sodium at the terminator region probed by our measurement (Lodders 1999). Another potential cause of atomic Na depletion is ionization by stellar UV photons (Fortney et al. 2003), a scenario which is plausible because we found HAT-P-19 to be magnetically active.

Among the known sample of Hot-Jupiter exoplanets which have already been investigated by transmission spectroscopy there are three planets similar to HAT-P-19b in their system parameters: HAT-P-1b (Bakos et al. 2007b), HAT-P-12b (Hartman et al. 2009) and WASP-29b (Hellier et al. 2010). All these planets have roughly the mass of Saturn, roughly the size of Jupiter and an equilibrium temperature of 1000 to 1200 K. They orbit solar-like main-sequence stars of spectral type G or K. Gibson et al. (2013a) obtained an optical transmission spectrum of WASP-29b around the sodium line and was able to significantly rule out a pressure-broadened absorption feature. Nikolov et al. (2014) observed HAT-P-1b in the optical regime during transit and detected extra-absorption at the sodium core in a 30 Å wide flux channel, but no spectral signature of the broadened line wings. Line et al. (2013) observed HAT-P-12 in the near-IR and found evidence against spectral signatures of H_2O theoretically expected in a clear atmosphere. All these studies have in common that they do not agree with theoretical cloud-free atmosphere models, but could be much better explained by an opaque layer in the atmosphere either blocking only the pressure-broadened wings or the entire absorption feature when observed in low spectral resolution. Our measurements for HAT-P-19b are in good agreement with these results and point towards the final statement of Fortney (2005) that, caused by the slant viewing geometry of transmission spectroscopy, the detection of clear atmosphere will be seldom. The only object for which the sodium wings indicating a clear atmosphere have been detected so far is the somewhat hotter HD209458b (Sing et al. 2008a). But also in the temperature regime of 2000 K and above it seems to be very common to find a spectrum less rich in features than expected by clear atmosphere models, see a review by Madhusudhan et al. (2014).

Finally, we want to give a word of caution on how much the result might depend on the details of the analysis: So far, in this work on HAT-P-19b we treat the light curve channels individually. If we assume here, just for a test, that the physical cause of the trend in the light curves is the same for all wavelength channels (for example differential atmospheric extinction), it would be reasonable to conclude that the coefficients of the detrending polynomial evolve over wavelength and are therefore correlated in adjacent wavelength channels. To test if such correlation had a significant effect on the transmission spectrum, we approximated the derived coefficients of the individually treated wavelength channels with a second order polynomial over wavelength and fixed the detrending polynomial in a new transit fit to these approximated values. A comparison of the transmission spectra is given in Figure 3.10. In black the spectrum of Figure 3.6 and 3.9 is shown derived from the individual treatment of the channels. In red, the test spectrum is presented in which the detrending polynomials are correlated. In another test we approximated the correlation by a linear function over wavelength and constrained the analysis of the region of most interest, the sodium channel and the 3 neighboring channels to both sides. The coefficients of the detrending polynomial were fixed in a new transit fit to the values of these linear approximation. The result is shown in green. Clearly, additional absorption in the sodium channel is indicated by a larger transit depth, significant to about $2.5\,\sigma$ (red) and $3.0\,\sigma$ (green). From about 6000 to 7500 Å the spectra mostly agree with each other, but on the blue and red end we see strong deviations. This example is simply meant to illustrate the dependence of the result on details of the data analysis. We favor the individual treatment of the wavelength channels because it is unclear to which extend the trend in adjacent wavelength channels are linked to each other. Telluric effects might be different in the sodium channel because of the telluric sodium absorption. Instrumental effects like pixel sensitivity are not correlated among channels either. A higher β factor for the sodium channel, when detrending is linked to the neighboring channels, also favors the independent treatment.

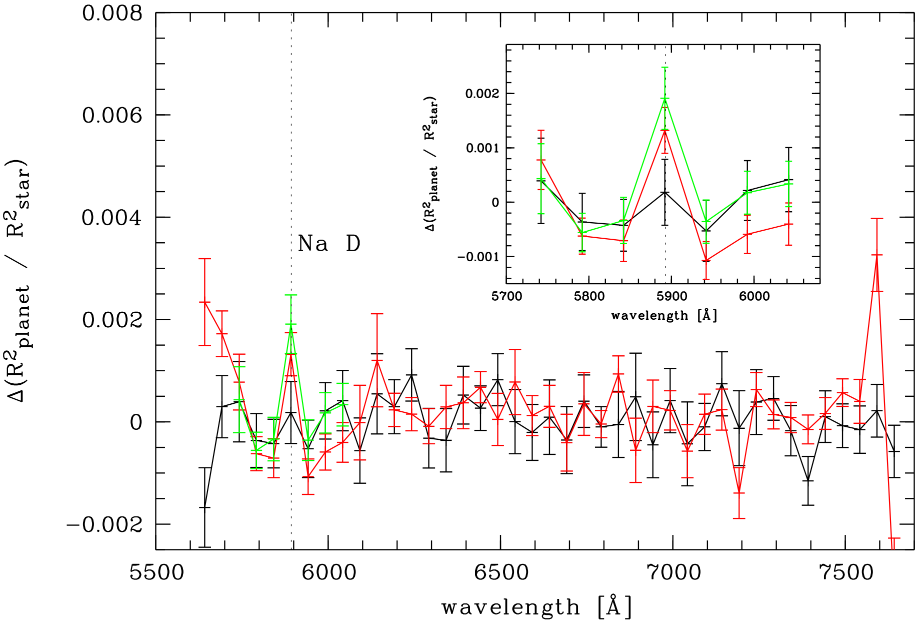

Fig. 3.10. Transmission spectrum of HAT-P-19b when the detrending of the light curve is linked to adjacent wavelength channels, see text for details. The black spectrum shows the independent treatment of the channels, in red the evolution of the detrending coefficients over wavelength is approximated by a second order polynomial. For the green spectrum the evolution of the coefficients of the detrending polynomial was approximated by a linear function over wavelength. The small panel shows a zoom into the sodium region.

3.4.3 The long term photometric variability

H11 gathered photometry data with the HATnet telescopes from September 2007 to February 2008, high-resolution spectra for RV follow-up have been taken in August 2009 to August 2010. They do not mention any indications for stellar activity from photometry or spectroscopy. The RV jitter is low, 6.7 m/s, and might be caused by instrumental systematics. However, the periodic photometric variations we found in data taken from December 2011 to October 2012 were interpreted as starspots moving in and out of view because of the larger amplitude of the variation in B than in V. The same period of ∼ 37 days detected in the HATnet data and STELLA data, consequently interpreted as stellar rotation period, shows an increase in amplitude from 2007 to 2012 by about a factor of 5. Possible interpretations for such an increase are a very homogeneous spot distribution in 2007 and a very inhomogeneous distribution in 2012. Another explanation is a change in activity level comparable with changes in the activity level during the 11-year solar cycle. Such stellar activity cycles have been detected in a variety of stars, see Strassmeier (2009) and references therein.

Knowing the rotation period of the star and its effective temperature, we have the opportunity to determine the age of HAT-P-19 using gyrochronology. Here, we assume that the host star was not spun up by tidal interactions with its close-in planet. According to Equation 15 in Husnoo et al. (2012) the timescale for synchronization of the rotation is above the age of the universe and several orders of magnitudes higher than for these systems with detected excess rotation possibly caused by tidal effects (Pont 2009; Husnoo et al. 2012; Poppenhaeger & Wolk 2014). In order to apply the age determination from Barnes (2010), the effective temperature was converted empirically to a B–V color using the formula in Reed (1998). We derived $\mathrm{B}-\mathrm{V} = 0.927 \pm 0.042$ from $\mathrm{T}_{\mathrm{eff}} = 4990 \pm 130$ K.

The errors arising from the unknown initial rotation period at zero age of a star between 0.12 d and 3.4 d result in an uncertainty of 0.2 Gyr for that specific spectral type and rotation period. Taking all uncertainties into account (error in effective temperature, error in period determination, error in age determination), we estimate the age of the exoplanet host HAT-P-19 to be $5.5^{+1.8}_{-1.3}$ Gyr. This result refines the age estimation from H11 of 8.8 ± 5.2 Gyr based on stellar evolutionary tracks.

Knowledge of the rotation period of the star and its spectroscopic line broadening $v \sin i$ allows in principle for the determination of the inclination of the star in the observer's line-of-sight (Walkowicz & Basri 2013). It does not provide an absolute angle between the orbital plane of the planet and its host star rotation axis, but as we know the inclination of the planetary orbital plane from the transit measurement to be close to 90°, any significant deviation of the stellar inclination from the same value indicates a misalignment of the planetary system. However, in case of very slow rotating stars like HAT-P-19, no meaningful conclusions can be drawn. The $v \sin i$ value of 0.7 ± 0.5 km/s (taken from H11) in combination with our stellar rotation period of ~ 35 days allows for inclination angles from 10 to 90 degrees.

4 Broad-band spectrophotometry of HAT-P-12b

4.1 Introduction

The search for a wavelength dependence of the apparent radius of an exoplanet is not limited to spectroscopic transit observation. In fact, multiple broad-band filters can be used to create a "spectrum" which consists of a few data points over the optical and NIR wavelength range. Similarly to the color index of stars which allows for a rough classification of stars, it might be possible to distinguish between several categories of planetary atmospheres by the usage of only a handful well separated color filters.

Transit light curves always suffer to some degree of correlated noise caused by the Earth atmosphere or instrumental effects (Pont et al. 2006). One approach to mitigate this is to observe transits at multiple epochs and multiple telescopes since these light curves are not correlated to each other and the influence of the individual red noise averages out (Lendl et al. 2013). In this work we combine a high number of transits in their majority taken with small to medium class telescopes at different epochs to refine the ephemeris and orbital parameters, search for transit timing variations and a wavelength dependence of the planetary radius.

The selected target for this study is the Hot Saturn HAT-P-12b. It was discovered in 2009 by Hartman et al. (2009) and has a mass of $\sim$0.2 M_J and a radius of about 1 R_J. The mean density and the surface gravitational acceleration is rather low ($g \sim 6$ ms^{-2}). HAT-P-12b orbits its host star on a close orbit of semi-major axis $a = 0.0384$ AU every $\sim$3.2 days. The host star HAT-P-12 is a K5 main sequence star with a mass of 0.73 $M_\odot$ and a radius of 0.7 $R_\odot$ (Hartman et al. 2009; Ehrenreich & Désert 2011). The low surface gravity and the equilibrium temperature of $\sim$1000 K result in an atmospheric pressure scale height of about 600 km. Together with the large transit depth due to the small stellar size, HAT-P-12b is among the known exoplanets with the largest potential transmission signal. The host star HAT-P-12 was described to be moderately active (Knutson et al. 2010). The line cores of the Ca H&K lines show emission features with $\log(R'_{HK}) = -5.1$. However, the jitter of the RV measurements is low with a few meter per second (Hartman et al. 2009).

The first follow-up photometry of HAT-P-12b was published by Sada et al. (2012), who presented one J band transit light curve. Shortly after, three optical light curves were analyzed by Lee et al. (2012), allowing for a transit parameter refinement and a more accurate ephemeris. Todorov et al. (2013) published upper limits on the eclipse depth and the brightness temperature. A first transmission spectrum was presented by Line et al. (2013) using HST in the Near Infrared.

The wavelength width of broad-band filters allows for high-precision photometry with rather small telescopes. Strömgren or even narrower filter systems in combination with a small telescope aperture would lead to unfeasible high photon noise in the light curves. However, the usage of broad filters like the Johnson/Bessel or Sloan filter system come with the drawback that signals of narrow spectral features in the planetary atmosphere like absorption from the sodium D line is strongly damped and smeared out. However, broad-band observations can be used to search for general trends in the spectrum like the rising absorption towards short wavelengths caused by Rayleigh-scattering or the predicted redward slope between very blue colors and the central part of the optical window caused by TiO (Fortney et al. 2010). Despite the growing number of observational publications in very recent years, the task remains challenging due to the weakness of the expected signals. Three groups have succeeded to constrain the potential atmospheric models: Nascimbeni et al. (2013b) and Biddle et al. (2014) showed that the spectrum of GJ3470b cannot be explained with a gray, featureless atmosphere. Instead, a Rayleigh slope needs to be included in the modeling to gain a reasonable fit to the observed data. For the atmosphere of GJ1214b, de Mooij et al. (2012) ruled out a cloud-free solar composition. The achieved precision of the broad-band spectrophotometry papers of Bento et al. (2014), Fukui et al. (2013) and de Mooij et al. (2013) did not yield significant results, but tentatively it was possible to favor a certain atmospheric model in front of others. Mancini et al. (2013a) could draw tentative conclusions when their data were combined with previously published results for the same object at other wavelengths. In contrast, there is a larger number of broad-band spectrophotometry investigations of exoplanets that did not reach the necessary precision to distinguish between atmospheric models (Southworth et al. 2012b; Nikolov et al. 2013; Mancini et al. 2013b, 2014b,a; Copperwheat et al. 2013; Chen et al. 2014; Fukui et al. 2014; Zhou et al. 2014).

The high number of transit light curves analyzed in this work provides the opportunity to analyze the data for transit timing variation (TTV). This technique allows the detection of so far unseen planetary mass companions and the derivation of various system parameters (Agol et al. 2005). In general, the current understanding of planet formation and migration predicts Hot Jupiters to orbit their host stars alone (see e.g. Steffen et al. 2012, and references therein). However, there might be exceptions from this general rule, as Szabó et al. (2013) presented several exoplanet candidates detected by TTVs of Hot Jupiters based on Kepler data. Furthermore, Maciejewski et al. (2013) and von Essen et al. (2013) announced tentative detections of TTV signals using ground-based data. However, ground-based results should be taken with care as the debate for TTVs in the WASP-10 system illustrates (Maciejewski et al. 2011; Barros et al. 2013). There are also a handful of examples of candidates or confirmed multi-planet systems with a Hot Jupiter, where indications or evidence of another companion was achieved with the radial velocity method, see Hartman et al. (2014) and references therein. Lee et al. (2012) found variations of the transit times of the target investigated here, HAT-P-12b, which were significantly larger than their error values. This result motivated us to investigate if HAT-P-12b might be exceptional, too.

4.2 Observations

We acquired data of in total 20 primary transit events. Observations were done with the STELLA telescope, the Large Binocular Telescope (LBT), the William Herschel Telescope (WHT), the Telescopio Nazionale Galileo (TNG), the Nordic Optical Telescope (NOT), the Asiago 1.82m telescope and the 0.8m telescope of the Montsec Astronomical Observatory (OAdM). Two transits were observed in multi-channel mode. The STELLA telescope has been used to monitor the host star HAT-P-12 in rwo colors for a length of about four month in 2012 and four month in 2014. A summary of the transit observations is given in Table 4.1 including the date of observation, the filter, the exposure time, the time between consecutive exposures (cadence), the number of data points, the rms, the beta factor (see Section 4.6) and the airmass range during the observation.

4.2.1 The transit observations

STELLA

STELLA observed 13 transits in the observing seasons 2011, 2012 and 2014. STELLA is a robotic 1.2m twin telescope located on Tenerife (Strassmeier et al. 2004). The instrument of use was its wide-field-imager WiFSIP (Weber et al. 2012) with a field of view (FoV) of 22'×22' at a scale of 0.32"/pixel. The detector is a single 4096×4096 back-illuminated thinned CCD with 15μm pixels. The telescope was slightly defocused during the observations (FWHM typically 2-3 arcseconds) to minimize flat-fielding errors (see e.g. Southworth et al. 2009). The observations have been carried out using the Sloan r' filter in the 2011 season and quasi-simultaneously with alternating filters Johnson B and V in 2012. The B band light curves have been of low quality because of the intrinsic faintness of HAT-P-12 at blue wavelengths and weather problems, therefore they are not analyzed here. In the year 2014 two transits were observed in Sloan g' and one in Sloan i'. The r' observations from 2011 were performed reading out the entire detector area. In the season 2012, we optimized the setup with the read-out of a central window of 1k by 1k to safe read-out time. An object centroid drift of a few pixel per hour over the detector is typical for the STELLA observations.

LBT

One transit was observed with the Large Binocular Camera (LBC, Giallongo et al. 2008) on April 4, 2013 (PI: I. Pagano). The LBC consists of two prime-focus, wide-field imagers mounted on the left and right arms of LBT, and is optimized for blue and red optical wavelengths, respectively. We applied the U_{spec} filter on the blue arm, a filter with Sloan u' response but having an increased efficiency, centered at $\lambda_c = 357.5$ nm, and the F972N20 filter on the red arm, which is an intermediate-band filter centered at $\lambda_c = 963.5$ nm. The two filters have been chosen to cover a very wide wavelength range, furthermore the F972N20 filter avoids most of the telluric lines in the red region. On both sides just the central chip of four chips has been read out to save hard disk space and a region of interest (window) has been defined to save read-out time. The final FoV encompassed $\sim$7.5×7.5 arcminutes^2. The blue arm was defocused to an artificial FWHM of about 4 arcseconds, the PSF of the red side lost a Gaussian shape and had a width of about 8 arcseconds at half the peak count rate. The exposure time was set to 90 seconds on both sides with a cadence of $\sim$125 seconds on the blue and $\sim$117 seconds on the red side. Unfortunately, the observation was affected by clouds, especially in the second half of the transit almost no flux of the target was received. However, the observation was not interrupted and a number of useful frames were recorded again after egress. The telescope was passively tracking during the time series resulting in a centroid drift of about 20 pixel in both directions on the blue side and 80/40 pixel in x/y on the red side.

WHT

We observed one transit on March 15, 2014 (PI: V. Nascimbeni) with the triple beam, frame-transfer CCD camera ULTRACAM (Dhillon et al. 2007). The instrument splits the incoming light into three channels with individual CCDs, allowing simultaneous observations with three filters. We chose the Sloan filters u', g' and r'. The exposure time for all three channels was 5.7 seconds with almost no overheads (25 ms) due to the frame-transfer technique. The telescope has been defocused to a FWHM of approximately 5/4/3.5 arcseconds in the u'/g'/r' band. The observing conditions were photometric. The drift of the centroid was below 2 pixels over the entire time series in both directions for g' and r', while it amounted to 5 pixel in u'. No windowing was applied to the FoV of 5×5 arcminutes^2.

For the u’ channel four exposures were co-added on chip before read-out to reduce the influence of the read-out noise.

TNG

One transit was observed with the TNG on May 28, 2014 using the focal reducer DOLORES in imaging mode (DDT program, PI: M. Mallonn). DOLORES is equipped with a 2048×2048 E2V 4240 CCD camera with a very good quantum efficiency at blue wavelengths and a FoV of 8.6×8.6 arcminutes^2. We employed the permanently mounted Sloan u’ filter. A binning of 2×2 was used to reduce the read-out time. An exposure time of 40 seconds resulted in a cadence of 49 seconds. A mild defocus was applied throughout the time series to reach an artificial FWHM of about 2 arcseconds. The observing conditions were non-photometric with variable seeing and the target flux varied by up to 30% on short time scale. Twice during the time series the position of the target jumped abruptly by about 10 pixel. In between these jumps the object drifted by less than 3 pixel/hour.

NOT

One transit was observed with the NOT on March 15, 2014 as a Fast-Track program (PI: M. Mallonn). The imaging time series was taken with the stand-by CCD imager StanCam, which hosts a 1k×1k TK1024A CCD detector. The FoV amounted to 3×3 arcminutes^2, sufficient to image the target and one nearby reference star of similar brightness. We used a Bessel B filter with an exposure time of 60 seconds, resulting in a cadence of 103 seconds. The night was photometric with a seeing between 1.0 and 1.3 arcseconds. We noticed an object drift of about 6 pixel in both directions over the length of the time series.

Asiago

Two transits were observed with the Asiago 1.82m telescope (PI: V. Nascimbeni) and its Asiago Faint Object Spectrograph and Camera (AFOSC). The camera hosts a 2k×2k E2V 42-20 CCD, which images the 9×9 arcminutes^2 FoV with a 0.26”/pixel plate scale. We applied a 4×4 pixel binning and read out only a region of interest to reduce the overheads to about 2 seconds. All images were exposed for 10 seconds. A defocus was used which enlarged the PSF to 3–5 arcseconds FWHM.

OAdM

One partial transit was observed on May 15, 2014 (PI: E. Herrero) with the fully robotic 80-cm Ritchey-Chrtien telescope of the Montsec Astronomical Observatory (Colomé et al. 2008). The telescope hosts a FLI PL4240 2k×2k camera with a plate scale of 0.36 arcseconds per pixel. Because of the intrinsic faintness of the K dwarf HAT-P-12 at blue wavelengths we chose the reddest filter available here which was the Cousin I filter. The exposure time accounted to 120 seconds with a cadence of 136 seconds. The beginning of the astronomical twilight prevented us from observing a full transit. The telescope was mildly defocused to an FWHM of $\sim$2.5 arcseconds, the centroids drifted over the time series by 60 and 30 pixel in x and y direction.

Table 4.1. Overview about new transit observations of HAT-P-12b. The columns summarize the observing date, the used telescope, the chosen filter, the exposure time, the observing cadence, the number of individual data points, the dispersion of the data points as root-mean-square (rms) of observation minus transit+detrend model, the β factor (see Section 2.2) and the airmass range of the observation.

Date	Telescope	Filter	t_{exp} (s)	Cadence (s)	N_{data}	rms (mmag)	β	Airmass
2011, Mar 9	Asiago	R	10	12.1	1117	2.00	1.07	1.00-1.20
2011, Apr 7	STELLA	r’	40	78	205	1.92	1.34	1.03-1.91
2011, Apr 23	STELLA	r’	40	78	85	1.45	1.00	1.07-1.28
2011, May 9	STELLA	r’	40	78	204	1.26	1.34	1.03-1.59
2011, May 25	STELLA	r’	40	78	204	1.83	1.00	1.08-2.77
2011, Jun 7	STELLA	r’	40	78	205	1.14	1.00	1.03-1.61
2011, Jun 23	STELLA	r’	40	78	203	2.03	1.00	1.07-2.76
2012, Feb 6	STELLA	V	30	145	133	4.10	1.00	1.03-1.90
2012, Mar 19	Asiago	R	10	12.1	930	2.11	1.00	1.03-1.42
2012, May 3	STELLA	V	40	186	92	2.04	1.00	1.03-1.36
2012, May 6	STELLA	V	40	186	107	2.77	1.00	1.03-2.02
2012, June 4	STELLA	V	40	128	129	3.88	1.00	1.03-2.12
2013, Apr 5	LBT	U_{spec}	90	125	66	1.57	1.00	1.02-1.28
2013, Apr 5	LBT	F972N20	90	117	63	0.98	1.00	1.02-1.28
2014, Feb 27	STELLA	g’	80	104	140	1.69	1.00	1.07-2.17
2014, Mar 15	STELLA	g’	80	104	136	1.34	1.30	1.03-1.28
2014, Mar 15	NOT	B	60	103	139	1.52	1.00	1.04-1.34
2014, Mar 15	WHT	u’	23	23	676	7.16	1.27	1.03-1.38
2014, Mar 15	WHT	g’	5.7	5.7	2717	1.69	1.89	1.03-1.38
2014, Mar 15	WHT	r’	5.7	5.7	2717	1.27	1.89	1.03-1.38
2014, May 15	OAdM	I	120	136	40	1.44	1.00	1.20-1.51
2014, May 28	STELLA	i’	45	72	240	1.55	1.00	1.04-1.56
2014, May 28	TNG	u’	40	49	308	5.44	1.09	1.03-1.32

4.2.2 Observations of the monitoring program

We monitored HAT-P-12 with STELLA/WiFSIP from April to August in 2012 spanning 112 days. If weather, target visibility and scheduling constrains allowed for it, a sequence of 7 exposure in Johnson V and 7 exposures in Johnson I was obtained every night. In a few occasions, the robotic telescope system observed multiple 7+7 blocks per night separated by a few hours. In total, we gathered 636 images in V and 631 images in I. The exposure time was 30 and 60 seconds, respectively.

In 2014, the monitoring program was continued from February until July. 1081 images were taken in V, 1077 images in I. The exposure time was 60 seconds in V and 50 seconds in I and the images were observed in blocks of 5 exposures per filter. Please note that in the year 2013 the CCD detector of WiFSIP was replaced, therefore the time series in 2012 and 2014 have not been obtained with identical instruments. Additional telescope manufacturing work was done in May 2014 followed by the development of a new pointing model, which manifests in the time series as an abrupt change in detector position on June 2. Unfortunately, this change was accompanied by a jump in the differential light curve of about 1 percent amplitude.

4.3 Data reduction

4.3.1 Transit data

The data reduction of the data obtained on STELLA, LBT, WHT, TNG, NOT and OAdM was done with the same scripts written with ESO-MIDAS which call the photometry software *SExtractor* (Bertin & Arnouts 1996). Bias and flat field correction was done in a usual way, with the bias value extracted from the overscan regions. Cosmic ray correction was done within SExtractor. We performed aperture photometry with circular apertures (MAG_APER in SExtractor) and automatically adjusted elliptical apertures (MAG_AUTO in SExtractor). The elliptical aperture offers the advantage to account for variations of the PSF over time, with the disadvantage of different apertures for target and comparison stars.

In a first step, our algorithm selects the brightest stars in the field and weights them based on their individual light curve quality in terms of point-to-point scatter (rms) (Broeg et al. 2005). Then, the algorithm automatically searches for the combination of comparison stars which minimizes the rms of the target light curve. It omits one star and computes the rms value in the differential target light curve using the weighted combination of all the other stars as artificial reference star. This star gets rejected whose exclusion reduced the rms value most. After a rejection the weights of the remaining comparison stars in the sample are estimated again. The rejection of stars and herewith the search for the best star combination finishes if the weighted combination of all kept stars yields a lower rms value in the differential target light curve than all the combinations with one star omitted. Note that the rms of the target light curve is not only computed on the out-of-transit part, but on the residuals of the entire time series after a transit fit including a second order polynomial in time for detrending (more on the transit light curve modeling in Section 4.6). In this way the algorithm searches for the comparison stars in the field that have the highest signal to noise *and* resemble the target in terms of systematics. As expected, the algorithms tends to choose only a low number of near-by stars in non-photometric conditions[1], while in photometric conditions the number of chosen comparison stars is higher (typically 5 to 8) including stars with larger spatial distance.

---

[1] In non-photometric conditions, e. g. with high cirrus clouds, systematics differ for spatially separated stars

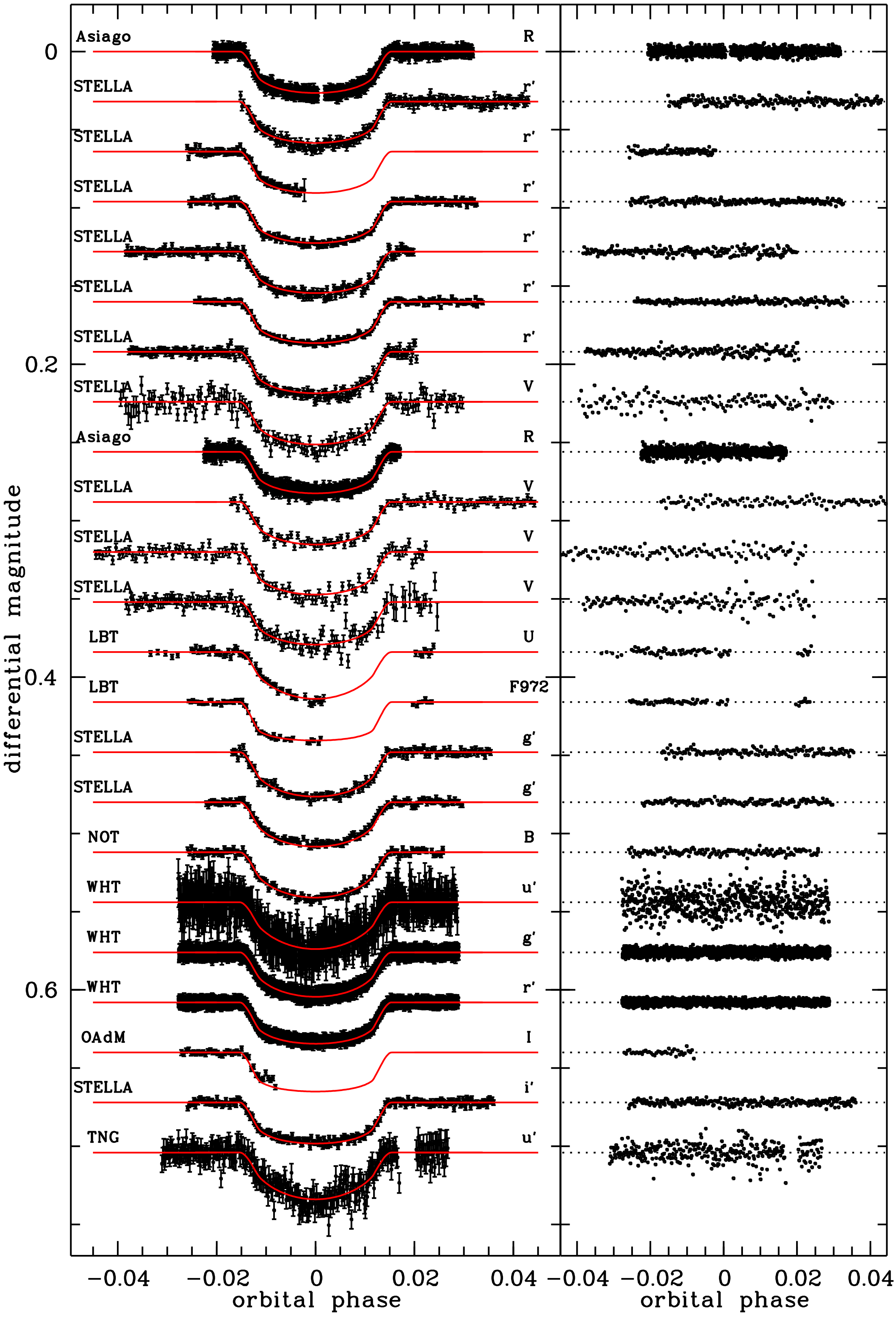

Fig. 4.1. Light curves of Table 4.1 after detrending with a second order polynomial over time, presented in a chronological order according to their observing date. The residuals are shown in the right panel.

In a last step, the algorithm repeats the light curve extraction many times with different aperture sizes to search for the aperture that minimizes the scatter in the differential target light curve. In the majority of our observations the circular aperture with fixed radius (MAG_APER) gave the more stable photometry than the flexible elliptical aperture(MAG_AUTO).

We performed a test of our data reduction pipeline by a comparison of our extracted ULTRACAM light curves with a version of the same light curves extracted with the ULTRACAM real-time pipeline (Dhillon et al. 2007). Note that the official real-time pipeline used only one comparison star and did not optimize the photometric aperture. A transit modeling of both light curve versions brought agreement of the derived transit parameters within a fraction of $1\,\sigma$ and our light curve extraction algorithm reduced the rms by 41%/23%/12% in the u'/g'/r' light curve.

The LBT transit observation suffered from highly variable sky transparency due to clouds moving through. We restricted the time series to data points that reached at least half the maximum flux value. We carried out a fringe correction for the LBC F972 light curve by the creation of a master fringe map. The bias corrected and flatfielded science frames were cleared from all detected objects by giving zero weights to all pixels in rather wide apertures around the centroids. Afterwards, the object-removed frames were smoothed with a median filter to suppress noise. The resulting images were averaged to create the master fringe map. The object drift during the time series was sufficient to obtain a complete map without object wholes. In each science frame the amplitude of the fringe pattern was estimated to scale the master fringe map before its subtraction. This fringe correction resulted in a marginal depression of the point-to-point scatter of the final transit light curve from 1.01 mmag to 0.98 mmag, the values of the transit parameters remained unchanged. With this experience of rather little benefit we did not apply a fringe correction to the very short OAdM I filter light curve. For the third light curve in our sample which was affected by fringing, the STELLA i' light curve, a correction was not possible. We did not apply a dither and the object drift was too little (pointing too stable) to assure that every pixel saw pure sky during the time series.

The Asiago data were reduced with the software package STARSKY, described in detail in Nascimbeni et al. (2013a). Figure 4.1 shows the differential light curves of all transits after normalization and detrending (for details of the detrending see Section 4.6.1).

4.3.2 Monitoring data

The data reduction of the HAT-P-12 monitoring data followed the description of the HAT-P-19 monitoring data reduction given in Section 3.2.2. In short, we used SExtractor for aperture photometry with the option of automatically adjusted elliptical apertures. The I band data were fringe corrected. We applied the method of optimal weighting of an ensemble of comparison stars to form an artificial reference for differential photometry. We verified that the three used comparison stars GSC2.2-N130301273, GSC2.2-N130301284 and GSC2.2-N130301294 were photometrically stable to our achieved precision.

We performed a selection of data points which consisted of a selection against data points of very high airmass, little flux caused by weather, extremely high sky background (twilight), extreme values of FWHM indicating problems with the telescope focus and extreme numbers of PSF elongation indicating vibrations of the telescope caused by wind. Furthermore, we excluded the data taken after June 2, 2014 with the new pointing model, as the new detector position caused a jump in the differential light curve of about 1.0% in V and 0.5% in I. Additionally, we applied a $5\,\sigma$ clipping to remove persistent outliers. The final light curve in V contained 486 of the 636 observed data points in 2012 and 873 of the 1081 data points in 2014. The I band light curve kept 402 of 631 images from the year 2012 and 709 of 1077 from the season 2014.

Finally, the V band light curve of 2012 had a length of 109 days with a scatter of 5.1 mmag (rms), while the data points of 2014 covered 112 days and show a deviation of 3.2 mmag. The deviation is lower simply because the exposure time was doubled in 2014. The I band light curve from 2012 scatters by 3.0 mmag, what is about the same as the scatter of 2.6 mmag of the I band data from 2014.

4.4 Re-analysis of literature data

Table 4.2. Overview about published transit observations of HAT-P-12, which were re-analysed in this work. The columns give the observing date, the chosen filter, the number of individual data points, the dispersion of the data points as root-mean-square (rms) of observation minus transit+detrend model, the β factor (see Section 2.2) and the reference of first publication.

Date	Filter	N_{data}	rms (mmag)	β	reference
2007, Mar 27	i’	151	1.78	1.00	Hartman et al. (2009)
2007, Apr 25	z’	375	2.62	1.00	Hartman et al. (2009)
2009, Feb 5	z’	219	2.66	1.00	Hartman et al. (2009)
2009, Mar 6	g’	214	5.14	1.17	Hartman et al. (2009)
2010, May 31	J	383	2.52	1.28	Sada et al. (2012)
2011, Mar 29	R	224	1.75	1.55	Lee et al. (2012)
2011, Apr 14	R	273	2.64	1.19	Lee et al. (2012)
2011, May 13	R	314	1.80	1.41	Lee et al. (2012)

We re-analyzed the optical transit light curves from Hartman et al. (2009) and Lee et al. (2012) and the J band light curve published by Sada et al. (2012). Whenever possible we treated the data identically to our observations, however, Hartman et al. (2009) used a detrending function different from the one commonly used in this work. We comment on this in Section 4.6.2. Before we included the literature light curves into our data sample, we tested whether our analysis routines were able to reproduce the published results. For the Hartman et al. (2009) light curves we achieved excellent agreement in the parameters, but found error bars that were higher by up to a factor of 2. Also the Lee et al. (2012) results (which were derived with JKTEBOP, too) could have been almost exactly reproduced, however our error estimation yields values higher by a factor of 2 for k and 10 for i. The J band light curve from Sada et al. (2012) shows rather complex deviations from the symmetric transit shape and was originally detrended by a 5th order polynomial over time fitted to the out-of-transit data. The uncertainty of this polynomial was not included in the transit parameter error estimation. Following this approach, we can reproduce the transit parameters to within $1\,\sigma$ with about the same error bars. However, a simultaneous fit of detrending polynomial and transit model and an error propagation of the uncertainty of the detrending to the transit parameters, changes the parameters by up to $1.5\,\sigma$ and increases the uncertainty by up to a factor of 2.

4.5 The potential starspot crossing event on March 28, 2014

An additional transit observed on March 28, 2014 by the 1.8m telescope of the Asiago Astrophysical Observatory showed clear deviations from a symmetrical transit model light (see Fig. 4.2). A scientifically interesting origin would be the crossing of a starspot on the visible hemisphere of the host star by the transiting planet, see Section 2.4 for a general discussion of starspots effects on transit light curves and Section 4.7 for a discussion of activity effects on HAT-P-12. A detection of a starspot signal could be analyzed for size and temperature information of the spot (Tregloan-Reed et al. 2013). A simple way to test if the light curve feature is of astrophysical origin and not caused by instrumental or telluric effects is the investigation of transit data taken simultaneously from other observing sides. We were awarded with telescope time for simultaneous observations of this transit event at the STELLA telescope and the 2.0m telescope of the Rozhen National Astronomical Observatory. Unfortunately, both observations had been weathered out. However, we found four transit data sets of this specific epoch at the web server of the Exoplanet Transit Database (ETD), observed by Giorgio Corfini, Frantiek Lomoz, Jaroslav Trnka and Martin Vrak. We detrended these light curves with a linear or quadratic function of time and fitted a light curve model with k, $r_p + r_\star$ and i fixed to literature values. Parameters free to fit were the vertical offset, the mid transit time and the limb darkening parameter of a linear limb darkening law. We choose this simplest limb darkening model because the color information given in ETD is very poor and the light curves were of too low quality to fit for more than one limb darkening coefficient (LDC). All five transit measurements correspond to the same transit event, nevertheless we did not fix the transit midtimes to a common value due to potential synchronization errors of the undocumented ETD light curves. The light curves with overplotted models are shown in Fig. 4.3. The individual ETD light curves are of rather low signal-to-noise, therefore their residuals were combined and binned in 4-minute intervals. Here, the achieved accuracy (rms) of about 2.5 mmag is sufficient to proof the ∼4 mmag feature in the Asiago light curve to be not intrinsic to HAT-P-12. The light curve could not be cleaned of that feature by a different treatment in the data reduction (comparison star selection, aperture size,...) or a decorrelation to external parameters like FWHM, pixel position, CCD temperature, etc. and was therefore discarded.

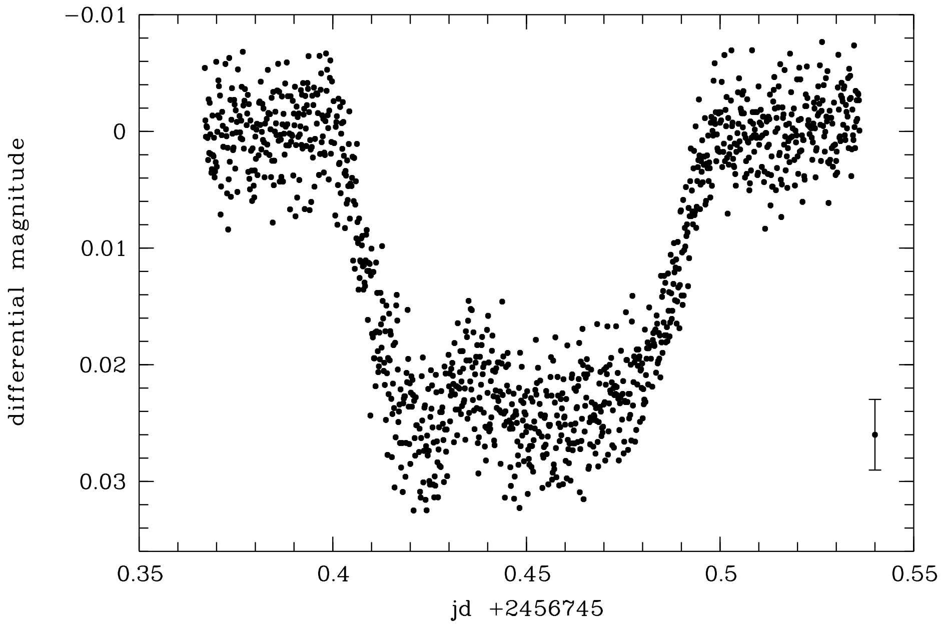

Fig. 4.2. Light curve of the March 28, 2014 taken by the 1.8m Asiago telescope. A representative error value is shown to the right. At Julian Date 2456745.437 the light curve deviates significantly from a model transit curve. Such asymmetry could be of instrumental or telluric origin, but could potentially also be of astrophysical origin as a starspot crossing of the transiting planet.

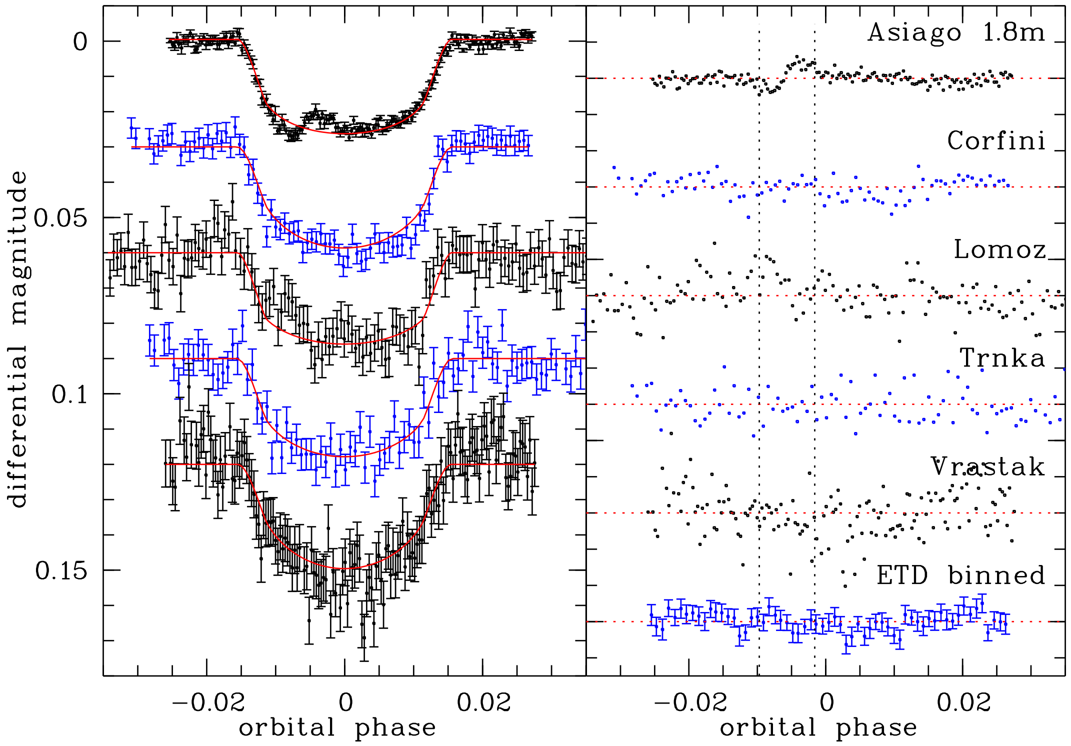

Fig. 4.3. Light curves of the epoch of the potential starspot crossing event, from top to bottom: Dataset from the 1.8m Asiago telescope (binned to 90 sec intervals), 4 ETD light curves from the observers Giorgio Corfini, Frantiek Lomoz, Jaroslav Trnka and Martin Vrak. The left panel gives the light curves with corresponding model when k, $r_p + r_\star$ and i are fixed to literature values. The right panel shows the residuals plus the combined ETD residuals binned in 4 minute intervals. The combined ETD residuals proof the feature in the Asiago residuals (marked by vertical dotted lines) to be not intrinsic to HAT-P-12.

4.6 Transit modeling and results

4.6.1 Detrending of the light curves

Most ground-based differential light curves show more features than the intrinsically symmetric transit dip. One feature common to almost all light curves is a long-term trend caused by atmospheric effects due to a color difference between the target and the combined reference stars. This trend can be modeled with a second order polynomial over time or a linear function with airmass as independent variable (see an example in Figure 4.4). However, short- and long-term features in the light curve can also occur due to instrumental effects, for example by residuals of pixel-to-pixel variations in sensitivity after flat field correction, errors in the sky correction or non-linear sensitivity of the CCD detector. Such instrumental effects might manifest as correlations of magnitude versus external parameters like pixel position, FWHM of the PSF, elongation of the PSF, sky background or pixel peak count rate. Nevertheless, regularly the source of short-term deviations from a symmetric transit light curve are not understood and cannot be modeled. The error estimation methods try to account for such residual systematics.

In this analysis we modeled the trend in the light curves consistently with a second order polynomial over time. For the transit model fit we used the publicly available software JKTEBOP (Southworth et al. 2004), which allows for a simultaneous fit for the

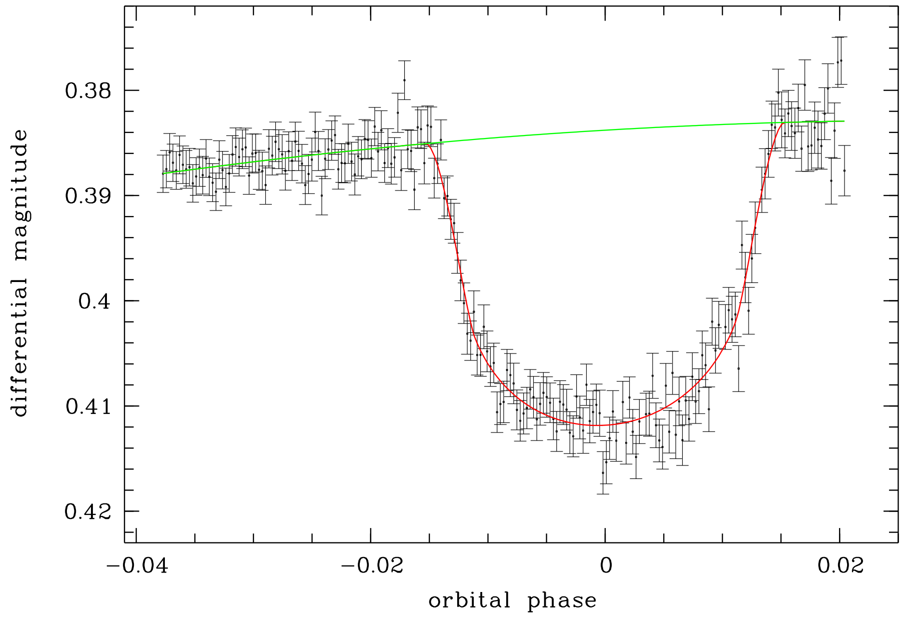

Fig. 4.4. Example of the long term trend in differential magnitude probably caused by atmospheric effects. The black data points are the r' band STELLA transit observation from 2011, Jun 23, overplotted in green with a second order polynomial over time to model the trend and in red with the combined trend + transit model.

transit model and detrending. However, JKTEBOP does not accept independent input parameters else than time, therefore we had to use another fit approach when testing more complex detrending function versus other external parameters. We used an iteration to first fit and subtract a model composed of transit + parabola over time from the raw light curve, in the second step we fitted the residuals with a linear or quadratic function with other parameters as independent variable. These other parameters were the x and y position on the detector, the FWHM and elongation of the target PSF, the sky background, the pixel peak count rate, the airmass and the rotation angle of the telescope. The iteration between these two steps run till the parameters converged. We checked if the decorrelation against another parameter than time was able to suppress the scatter in the residuals (= raw data minus combined model of transit, time parabola and linear/quadratic function over an external parameter). In a few cases we found marginally lower scatter compared to the transit + time parabola model, but according to the BIC value this small improvement was insufficient to verify the inclusion of additional free fit parameters. Hence, for none of our transit observations we found a significant correlation between the differential magnitude and a parameter different than time. Therefore, throughout this HAT-P-12b analysis we used a second order polynomial over time to detrend/decorrelate the light curves.

4.6.2 Global transit parameters

We started the analysis by fitting all light curves individually with a transit model that included a second order polynomial over time. The transit fit parameters consisted of the sum of the fractional planetary and stellar radius, $r_\star + r_p$, and its ratio $k = r_p/R_\star$, the orbital inclination i, the transit mid point T_0 and the host stars LDC u and v of the quadratic limb darkening law. The index "$\star$" refers to the host star and "p" refers to the planet. The dimensionless fractional radius r is the absolute radius R in units of the orbital semi-major axis a, $r_\star = R_\star/a$. The planetary eccentricity was fixed to zero following Hartman et al. (2009) and the period P to 3.21306 days according to Lee et al. (2012). Additional fit parameters were the 3 coefficients $c_{0,1,2}$ of the parabola over time.

In a first step we applied a $4\,\sigma$ rejection to the light curve residuals after the subtraction of an initial model, with σ being the standard deviation. A following fit was used to rescale the individual photometric error bars: The error bars supplied by SExtractor yielded a reduced χ^2 always slightly larger than 1, which indicates that the photometric error bars are underestimated. Therefore, we enlarged the error bars by a factor individual to each light curve to give a χ^2_{red} of unity. Furthermore, we calculated the β factor, for details see Section 2.2. It was estimated as the average of the values from 10 to 25 minute bins, since the ingress of HAT-P-12b lasts about 19 minutes. The derived β factor for each transit light curve was used as a factor to further enlarge the individual photometric error bars, Table 4.1 and Table 4.2 summarize the derived values for the newly obtained and the re-analyzed light curves.

Theoretical LDC for the stellar parameters of HAT-P-12 were made available by Claret (2000) and Claret (2004) derived from ATLAS and PHOENIX models. We fitted our complete r' and g' transits using a linear limb darkening law, with $r_p + r_\star$, k, i and the linear LDC as free fit parameters. The obtained limb darkening values were closer to the theoretical values of the ATLAS stellar models than the values derived from the PHOENIX stellar models by Claret (2004). In the remaining part of the analysis we used the quadratic limb darkening law with initial values for the coefficients u and v found by interpolating tabulated ATLAS values from Claret (2000) and Claret (2004) for the stellar parameters of HAT-P-12: $T = 4650$ K, log $g = 4.61$, [Fe/H]$= -0.29$, and $v_{mic} = 0.85$ km s^{-1} (Hartman et al. 2009).

By fitting all transits individually, we find transit parameter values that deviate significantly from their mean. Two different approaches can explain this phenomenon: Either this difference is of astrophysical origin, caused by stellar activity or atmospheric variability for example caused by weather on the planet. Or the difference is caused by the measurement, i. e. residual red noise in our light curves that was not removed by our polynomial detrending function and whose influence was underestimated in the error estimation. The result of our monitoring program shows the host star to be fairly constant (see Section 4.7), ruling out significant effects on our derived transit parameters. Furthermore, any potential weather phenomena are too small in amplitude to reasonably explain the transit parameter deviations. However, due to the large potential transmission signal of HAT-P-12 (see Section 2.1) variations of r_p as function of wavelength might be realistic. Hence, we attribute all significant variations in $r_\star$, i, and the fitted LDC to residual red noise. For a better consideration of this red noise in the derived parameter uncertainties, we formed a first version of the global parameter values as a weighted mean and re-calculated the β factor per transit observation, now on the residuals regarding the joint transit model.

The new β factor estimation and the derivation of the global parameter values was a multi-step process. In the first joint model fit we fixed $r_\star$ and i to global values, in the second step we fixed the linear LDC u and in the third step also r_p. The values for the fixed parameters were newly derived in every step. Note that u and r_p were treated as wavelength dependent and fixed to values per filter band instead to global values. Thus, the only free parameter in the last step per transit fit were the three coefficients of the second order detrending polynomial and T_0. The rms values and β factors given in Table 4.1 and 4.2 were derived in the last step of this procedure. The β values were in average 10%, in maximum 50% higher than in the first step of their derivation, the rms values increased typically by only very few percent.

Under the assumption of no intrinsic planetary and stellar variability, we can compare the individually derived transit parameters and their uncertainties to the mean to draw a rough conclusion about the reliability of the uncertainties: The 25 values of the complete transits analyzed in this work give a reduced χ^2 for the inclination i of 2.2, which can be interpreted as slightly underestimated error bars. For the fractional stellar radius $r_\star$ the value is 1.0 and 0.9 for the linear LDC u (derived values of u were compared with their theoretical predictions), an indication for error bars that match the scatter of within these 25 measurements very well. The reduced χ^2 for the radius ratio k is rather high with 3.5, hence either the errors are underestimated or we see intrinsic effects like a potential wavelength dependence (see Section 4.6.4) or potential starspot modifications of the light curves, for which k is the most sensitive transit parameter (see Section 4.7).

With the newly determined β factors of the individual transits we fit now all light curves of one filter band simultaneously. JKTEBOP does allow the simultaneous fit of multiple transit observations if one joint limb darkening function can be applied. The software can not attribute different LDC to subsamples of the input data, and therefore the simultaneous fit of multiple color data makes no sense. The simultaneous fit of multiple light curves compared to the average of individually fitted light curves has the advantage of being sensitive to red noise in the data, while a weighted average is insensitive to systematics among the individual results. Hence, in all our analysis, the uncertainties of a simultaneous fit of multiple transits were larger and hence more conservative than the uncertainties derived by a weighted average ($\sigma^2 = 1/\Sigma_{i=1}^{n}\sigma_i^{-2}$).

However, since JKTEBOP is not able to define subsamples of the input data and detrend them individually, it requires the individual transits to be detrended and normalized before their simultaneous fit. Therefore, the uncertainty of the detrending model (second order polynomial over time) is ignored in the error estimation of the transit parameters. We performed a simulation to investigate how much the transit parameter uncertainties are underestimated due to this ignorance. We created three light curves with a sampling of about 100 data points in-transit and 100 out-of-transit. The first light curve did not contain a trend, the second contained a parabolic trend with extremum near the transit mid point and the third contained a parabolic trend with the extremum outside the data points (see the upper panel of Figure 4.5). We investigated the effect on full transits (with out-of-transit baseline on both sides) and on partial transits with a removal of all data points before ingress (“cut” 1 in Figure 4.5) and with a removal of all data points before the flat bottom part during transit (“cut 2”). Gaussian noise was added to the light curve as there is one example shown at the bottom of the upper panel of Figure 4.5. We fitted the transits with $r_p + r_\star$, k, i, T_0, u and c_0 as free parameters ($n = 6$ with n as the number of fit parameters) or with these six plus c_1 and c_2 ($n = 8$), with $c_{0,1,2}$ being the three coefficients of the second order polynomial over time. For error estimation of the uncertainties we run Monte Carlo simulations and draw the 1 sigma uncertainty as the 68.3% of highest probability.

As seen in the lower panels of Figure 4.5, the ratio between the uncertainties when fitted for $n = 6$ and $n = 8$ parameters depends whether the transit is complete or not. For a full transit the uncertainty of the $r_p + r_\star$, k and i is underestimated by less than 13%, a value that can be neglected when we take into account that for multiple simultaneously fitted transits this number decreases further by the square root of the number of transits. This is true under the reasonable assumption that the trends and their uncertainties of the individual transits are uncorrelated. Therefore, the detrending before the simultaneous transit fit is justified. However, to get individual transit times as well as if we fit partial transits, the uncertainty of the detrending function can not be ignored, thus the detrending should be included in the fit and error estimation.

The light curves from Lee et al. (2012) and Hartman et al. (2009) we obtained in an already detrended format. Following our argumentation stated above we assume that the

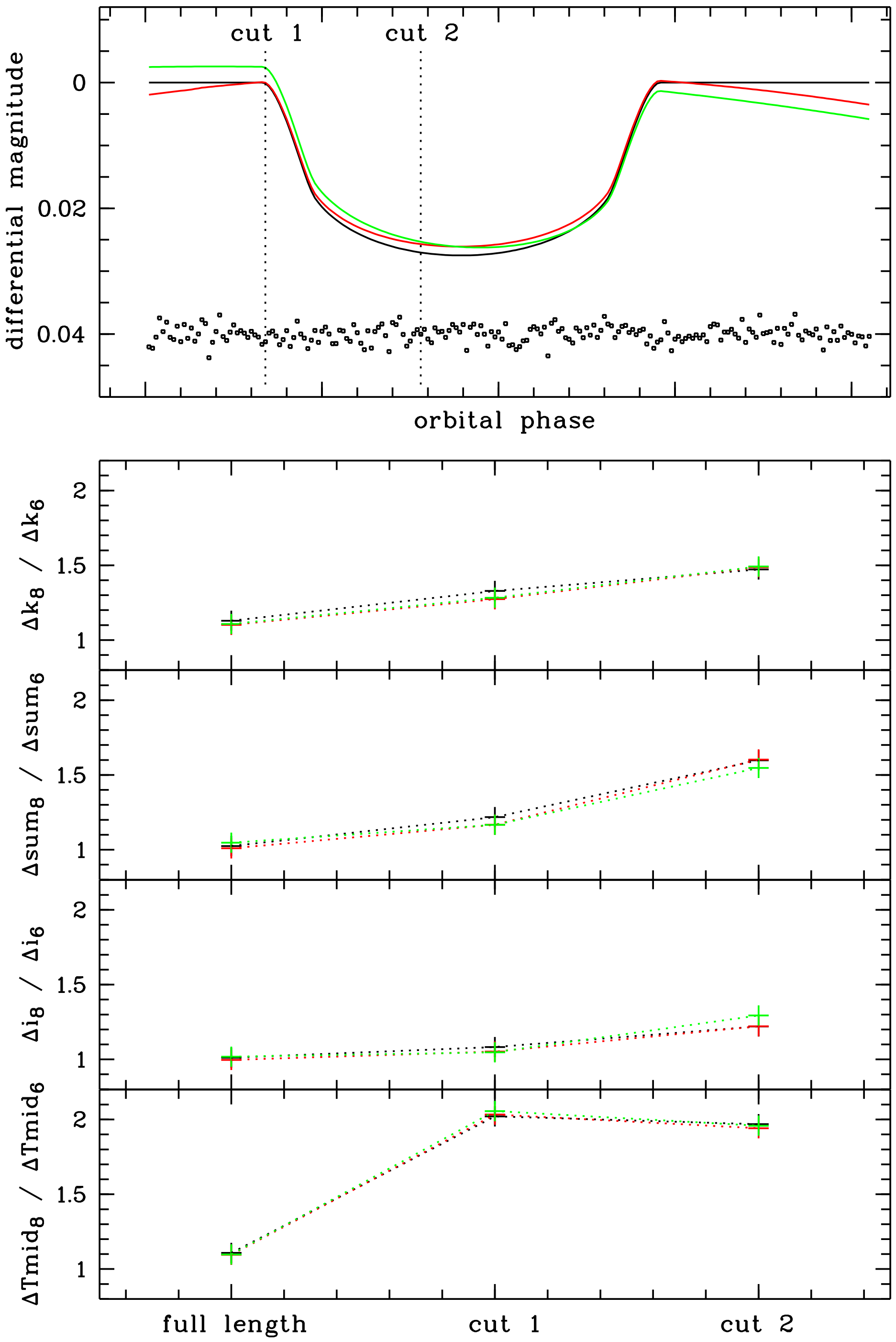

Fig. 4.5. Results of the simulation to investigate the underestimation of transit parameter uncertainties when the detrending uncertainty is ignored. The upper panel shows the three light curves without a trend (black), with a parabolic trend with extremum near the transit mid point (red) and with a parabolic trend with extremum outside the data points (green). The investigation was done for full transits and partial transits starting at "cut 1" and "cut 2". The lower panels show the ratio of the derived uncertainty between the fit with eight free parameters ($r_p + r_\star$, k, i, T_0, u and $c_{0,1,2}$) and six free parameters ($c_{1,2}$ fixed) for the parameters k, $r_p + r_\star$, i and T_0. A ratio very close to unity indicates that the uncertainty introduced by the detrending coefficients c_1 and c_1 is negligible.

error introduced by the linear detrending function over time used by Lee et al. (2012) can be neglected. Hartman et al. (2009) used a more complex model for systematic corrections in their follow-up light curves. Their External Parameter Decorrelation (EPD, Bakos et al. 2010) contains five free parameters per individual transit (hour angle, square root of hour angle, FWHM, elongation and position angle). In a test we ignored their influence on the uncertainty of the transit parameters and fitted a transit model to the detrended light curves. We expected to derive smaller transit parameters uncertainties due to this ignorance than Hartman et al. (2009), who jointly fit for the transit parameters and the detrending parameters. Instead, our error bars are larger by a factor of $\sim$1.5-2, potentially caused by the different error estimation techniques. The transit parameters itself agree well to within $0.5\,\sigma$. Hence, we conclude that the detrending is no significant error source for these light curves and keep on working on the EPD-detrended light curves.

Table 4.3 lists the transit parameters derived from all complete transits of each band fitted simultaneously. Note that for a simultaneous fit it was necessary to convert all barycenter-corrected timings of the observations to a common time standard which is in this work the Barycentric Dynamical Time (TDB) following the recommendation of Eastman et al. (2010). The u' band transits are not listed as their rather low accuracy would not improve the global results. Free parameters of the fits were $r_p + r_\star$, k, i, T_0, c_0, the period P and the linear coefficient u of the quadratic law. The quadratic LDC v was fixed to its theoretical value, but perturbed during the error estimation. For the B band transit, the only filter with only a single transit measurement in Table 4.3, we kept also u to its theoretical value to avoid the JKTEBOP warning of a "light curve solution with inclination of 89.9 degree or more". For error estimation we run a Monte Carlo simulation of 5000 steps and the residual-permutation algorithm (see detailed explanation in Section 2.2) supplied by JKTEBOP and chose the larger value of both. The final values were formed as the weighted average of the seven filters.

As discussed earlier, the weighted average neglects systematic uncertainties and therefore underestimates the true final uncertainties by a certain amount. One argument in favor of this procedure is the high number of transits involved here from which the majority is taken at different epochs with different telescopes, hence there should be no common systematics and individual systematics should average out. Although the average weight is routinely used by JKTEBOP users (Southworth et al. 2012a,b, 2013; Mancini et al. 2013b,a, 2014b), it certainly is a disadvantage of JKTEBOP which could be circumvented by a transit fit package that can fit transits of multiple colors simultaneously like EXOFAST[2] (Eastman et al. 2013) or TAP[3] (Gazak et al. 2012).

For simultaneously fitted multiple transit data sets, the residual-permutation method gives mostly higher error bars than the Monte Carlo simulation because it is sensitive to red noise while the MC approach is not. However, the uncertainties seem to be too conservative when looking at the reduced χ^2 of the values of the seven filters: The inclination i and fractional stellar radius $r_\star$ give χ^2_{red} of 0.2 and 0.1, for u we derive 1.0. Also the value for k decreased from 3.5 for the 25 individually complete transits to 1.3 for the seven color-combined values.

Our final transit parameters are generally in good agreement with previous publications on HAT-P-12b. Most values agree within the $1\,\sigma$ levels, the strongest deviation of about $2\,\sigma$ is found for k between our value and the one from Hartman et al. (2009). The rather high value for i of Lee et al. (2012) matches the value of this work to $1\,\sigma$ if we consider the uncertainty of 1.0 which we derive from a re-analysis of their light curves.

---

[2] http://astroutils.astronomy.ohio-state.edu/exofast/

[3] http://ifa.hawaii.edu/users/zgazak/IfA/TAP.html

Table 4.3. The derived transit parameters of this work in comparison to literature values for HAT-P-12b.

	$r_\star = R_\star/a$	$k = r_p/r_\star$	i (deg)	linear LDC u	quad. LDC v
B	0.08526 ± 0.00382	0.13916 ± 0.00311	89.00 ± 1.04	0.9150	-0.0592
g'	0.08654 ± 0.00235	0.13877 ± 0.00202	88.54 ± 0.53	0.8156 ± 0.0333	-0.0122
V	0.08518 ± 0.00582	0.13675 ± 0.00450	89.26 ± 1.31	0.7473 ± 0.1094	0.0961
r'	0.08494 ± 0.00147	0.13598 ± 0.00139	89.08 ± 0.66	0.5779 ± 0.0272	0.1665
R	0.08542 ± 0.00153	0.13800 ± 0.00167	88.95 ± 0.64	0.5824 ± 0.0350	0.1823
i'	0.08501 ± 0.00261	0.13521 ± 0.00209	89.30 ± 0.85	0.5321 ± 0.0632	0.2198
z'	0.08567 ± 0.00295	0.14132 ± 0.00180	88.80 ± 0.92	0.3073 ± 0.0642	0.2426
final	**0.08534 ± 0.00084**	**0.13781 ± 0.00074**	**89.03 ± 0.28**		
Hartman et al. (2009)	0.0850 ± 0.0013	0.1406 ± 0.0013	89.0 ± 0.4		
Lee et al. (2012)	0.0852 ± 0.0012	0.1370 ± 0.0019	89.9 ± 0.1		
Sada et al. (2012)	0.0891 ± 0.0045	0.1404 ± 0.0026	88.5 ± 1.0		
Line et al. (2013)	0.0862 ± 0.0029	0.137 ± 0.0011	88.7 ± 0.6		

4.6.3 Ephemeris and O-C diagram

We fitted all individual transits, complete or partial, with a transit model fixing $r_p + r_\star$, k and i to the final parameter values of Table 4.3. Free parameters are the transit midtime T_0, the linear LDC u and the three coefficients of the detrending polynomial $c_{0,1,2}$. The uncertainties were estimated using a Monte Carlo simulation with 5000 steps. Although the light curves from Hartman et al. (2009) and Lee et al. (2012) used slightly different detrending functions, we approximated their error contribution by inclusion of the same three free parameters $c_{0,1,2}$ as for the newly observed light curves of this work. The fit and MC error estimation of the Sada J band light curve additionally contained the free parameters c_3, c_4 and c_5 to model the trend with a 5th order polynomial over time. The quadratic LDC v was fixed to its theoretical value. We did not perturb v in the MC simulation since we found that T_0 is insensitive to the treatment of limb darkening.

We compared our derived uncertainties of T_0 to those from Lee et al. (2012), who also re-analyzed the Hartman light curves for T_0. Our uncertainties are in average two times larger for the same light curves. The T_0 estimations are almost identical with only 2 seconds mean difference for the three R band light curves of Lee et al. (2012). However, for the three full transits of Hartman et al. (2009) there is a difference between our and the Lee estimation of 60 to 65 seconds. This indicates that Lee et al. (2012) probably did not homogenize the time standard between their data and the Hartman light curves. Hartman et al. (2009) presents all times in the time standard UTC (J. Hartman, private communication), while Lee et al. (2012) and this work use Barycentric Dynamical Time (TDB). The difference between both standards was 65.184 seconds in 2007 at the time of the first two Hartman light curves and 66.184 seconds in 2009. The transit midtime of the J band light curve was consistently estimated by Sada et al. (2012) and this work with a difference of about $1\,\sigma$ due to the improved simultaneous detrending here. Our derived uncertainty is about 50% higher.

Simultaneously observed transits offer the possibility to test the reliability of the derived transit timing uncertainties, although one needs to be careful to draw definite conclusions from such low-number statistics. We observed the transit of March 15, 2014 with three different telescopes, the William Herschel Telescope observed with ULTRACAM in three different bands. Hence, we have five transit light curves of the very same event. The reduced χ^2 value of these five transit midtimes is 2.32. We run a simulation of 10000 datasets of five points each, added Gaussian noise and found that in 10% of all cases such a χ^2_{red} or higher was reached. Therefore, it appears likely that the uncertainties are slightly underestimated. However, with a hypothetical increase of only 10% on the error bars the χ^2_{red} value would already lie within $1\,\sigma$ of the mean of the simulated χ^2_{red} distribution.

Table 4.4 summarizes all individual transit timings with their uncertainties and includes the individual deviation $O - T_c$ of the observation from the calculated ephemeris. All times are given in BJD(TDB). We used a linear least-squares fit to the transit times of the 26 complete transits to newly determine a linear ephemeris:

$$T_c = \text{BJD(TDB)}\, 2456032.151332(39) + 3.21305756(20)\, N. \tag{4.1}$$

T_c is the predicted central time of a transit, N is the cycle number with respect to the reference midtime and the numbers in brackets give the uncertainties of the last two digits estimated with a Monte Carlo simulation of 5000 steps. The reference midtime was chosen to minimize the covariance between reference midtime and period. The estimated period differs by about $1\,\sigma$ from the original value given in the discovery paper Hartman et al. (2009), but is an order of magnitude more accurate. However, the deviation to the period value of Lee et al. (2012) is about $5\,\sigma$, our period is 0.15 seconds shorter. This can be understood in that the very first transits of the data sample, the Hartman transits, happen systematically earlier in the calculation of Lee et al. (2012) which might be explained by a missing UTC-TDB correction.

Table 4.4. Observed transit times of HAT-P-12b. The transit times of the literature light curves were newly estimated in this work.

BJD(TDB) (2,450,000+)	Uncertainty	Cycle number	$O - T_c$	Reference
4187.85647	0.00061	-574	0.00017	Hartman et al. (2009)
4216.77343	0.00023	-565	-0.00037	Hartman et al. (2009)
4869.02462	0.00033	-362	0.00013	Hartman et al. (2009)
4897.94297	0.00057	-353	0.00095	Hartman et al. (2009)
5347.76952	0.00035	-213	-0.00054	Sada et al. (2012)
5630.51929	0.00011	-125	0.00015	this work (Asiago)
5649.79770	0.00035	-119	0.00022	Lee et al. (2012)
5659.43649	0.00044	-116	-0.00016	this work (STELLA)
5665.86227	0.00037	-114	-0.00049	Lee et al. (2012)
5675.50436	0.00047	-111	0.00242	this work (STELLA)
5691.56661	0.00022	-106	-0.00061	this work (STELLA)
5694.78089	0.00029	-105	0.00060	Lee et al. (2012)
5707.63244	0.00027	-101	-0.00006	this work (STELLA)
5720.48443	0.00015	-97	-0.00031	this work (STELLA)
5736.54999	0.00030	-92	-0.00004	this work (STELLA)
5964.67787	0.00059	-21	0.00075	this work (STELLA)
6006.44779	0.00012	-8	0.00091	this work (Asiago)
6051.42937	0.00048	6	-0.00030	this work (STELLA)
6054.64202	0.00060	7	-0.00070	this work (STELLA)
6083.55936	0.00065	16	-0.00088	this work (STELLA)
6388.80101	0.00081	111	0.00029	this work (LBT)
6388.80064	0.00048	111	-0.00007	this work (LBT)
6716.53165	0.00033	213	-0.00093	this work (STELLA)
6732.59827	0.00063	218	0.00039	this work (STELLA)
6732.59765	0.00011	218	-0.00022	this work (NOT)
6732.59811	0.00028	218	0.00023	this work (WHT)
6732.59741	0.00023	218	-0.00046	this work (WHT)
6732.59796	0.00009	218	0.00008	this work (WHT)
6793.64833	0.00092	237	0.00236	this work (OAdM)
6806.49642	0.00062	241	-0.00178	this work (STELLA)
6806.49815	0.00019	241	-0.00004	this work (TNG)

Figure 4.6 shows the deviations of the individual transit times from the linear ephemeris of Equation 4.1. All data points give $\chi^2_{\rm red} \sim 4.8$ and an exclusion of the partial transit lowers this value only marginally to $\chi^2_{\rm red} \sim 4.5$. The most significant deviation from the ephemeris of almost $7\,\sigma$ shows the data point from the Asiago telescope March 19, 2012. If this point is excluded, the $\chi^2_{\rm red}$ lowers to 2.4.

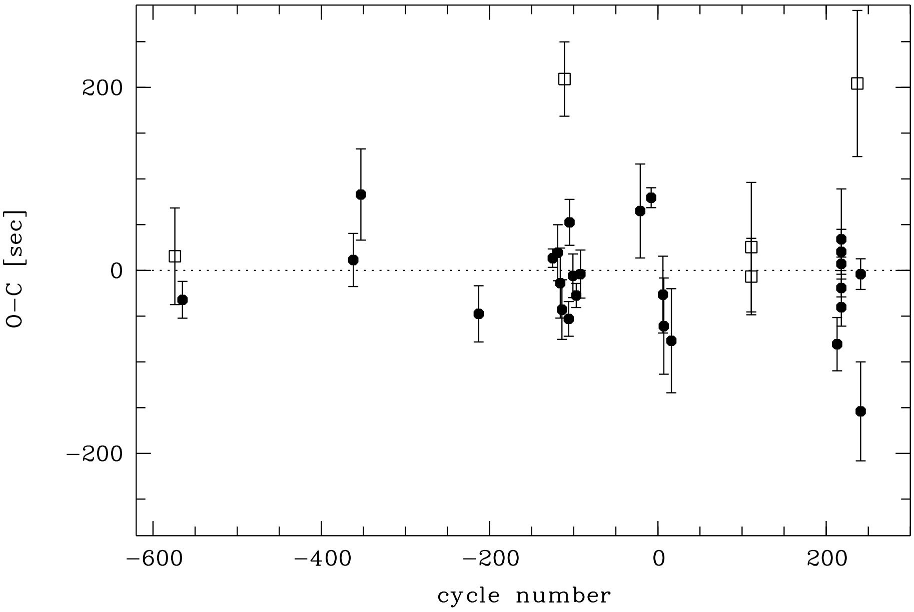

Fig. 4.6. Transit timing residuals versus the linear ephemeris of Equation 4.1. The filled symbols represent complete transit, the open squares mark transits which were only partially observed.

We calculated a Lomb-Scargle periodogram of all transits times excluding the partial transits, which is shown as black line in the upper panel of Figure 4.7. For a test, we excluded again the Asiago transit from March 19, 2012 and found a very different periodogram without any significant peak, given as red line in the upper panel of Figure 4.7. The lower panel shows the window function. The limit for the highest frequency was defined by the average Nyquist frequency. We conclude that we find no evidence for a transit timing variation and that the rather high value of $\chi^2_{\rm red} \sim 2.4$ is caused by an underestimation of the error bars due to systematics. One potential source of systematics in the light curves that influence the timing are starspots (Barros et al. 2013), a plausible scenario for this slightly variable host star, see Section 4.7.

4.6.4 Planetary radius over wavelength

One major goal of this work is the search for a wavelength dependence of the effective planetary radius. For this purpose, we fitted all light curves again individually, this time by fixing the inclination i and the fractional stellar radius $r_\star$ to the values derived in Section 4.6.2 and the period and transit midtime to values derived from the ephemeris (Equ. 4.1) in Section 4.6.3. All these parameters are assumed to be wavelength independent, but their global values have uncertainties. There are at least two ways how to deal with these uncertainties. The first is to include them in the Monte Carlo and residual-permutation error estimation as Gaussian priors, i. e. the values of these parameters are perturbed according to their uncertainties. The second is to neglect $\Delta r_\star$, Δi and ΔT_c under the assumption that they are a source of uncertainty common to all band passes. The derived

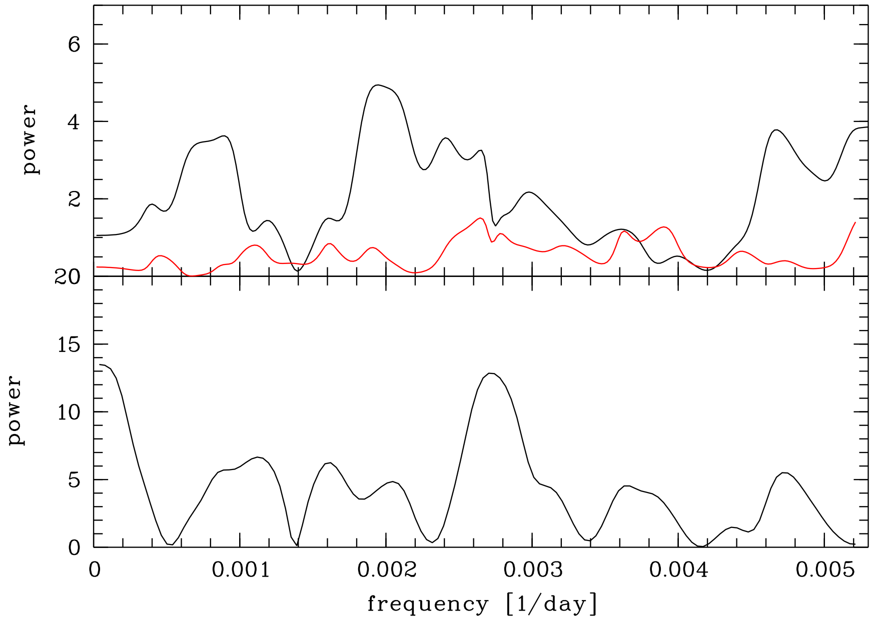

Fig. 4.7. Upper panel: Lomb-Scargle periodogram of the timing deviation from the linear ephemeris (O-C) when excluding the partial transits (black). A marginal signal can be seen at a frequence of ~ 0.0019 day^{-1}. In comparison the periodogram when the transit of March 19, 2012 (cycle number $= -8$) is excluded (red). Lower panel: The window function of the data set.

error bars Δk are then relative errors. Both ways are accepted in the literature, here we chose the second. Free fit parameters of the model were the fractional planetary radius r_p and the three coefficients of the detrending parabola $c_{0,1,2}$. For comparison we fitted each transit twice, first with the linear stellar LDC u as fit parameter and at second with u fixed to its theoretical value. The quadratic stellar LDC v was fixed to its theoretical value in both cases but perturbed in the error estimations. The results for r_p, here given in combination with the wavelength-independent $r_\star$ as the planet-star radius ratio k, are presented in Table 4.5 and Figure 4.8.

We combined the data sets per filter band again in a simultaneous fit. As discussed and justified in Section 4.6.2, this approach does not allow for the inclusion of c_1 and c_2 as fit parameters. Free parameters were r_p, c_0 as the vertical offset called *scale factor* in JKTEBOP and u. Note that several similar studies using JKTEBOP for broad-band transmission spectrophotometry do not mention c_0 as free parameter in this analysis (e.g. Southworth et al. 2012b; Mancini et al. 2013b; Nascimbeni et al. 2013b). However, if the vertical offset is fixed to a certain value, the uncertainty of the light curve normalization is neglected, or in other words, the uncertainty of the level of the out-of-transit baseline is not taken into account. Own tests have shown that fixing c_0 leads to an underestimation of $\mathit{\Delta} k$ by 25 to 50% depending on the amount of out-of-transit data points. The partially observed transits from the LBT were not included in the u' band, respectively z' band data set. Instead, they were analyzed separately to fully account for the detrending uncertainty. Furthermore, the two partial STELLA r' transits and the partial OAdM transit were not analyzed here. In general, we note a very good agreement of the observationally derived linear LDC per filter and their theoretical calculations. Only in the two filter sets mostly affected by red noise, R and J, we see deviations of 2.7 and 2.3 σ. Following are a few comments to the datasets per filter:

- u' filter: The partial transit of the LBC is very sensitive to the detrending uncertainty

Table 4.5. The derived planet-star radius ratio k per transit observation with relative uncertainties. An error value of 0.0 in the forth Column stands for a fixed value of u that was perturbed in the error estimation. See the text for more details.

date	filter	$k = r_p/r_\star$ u free	u fitted	k u fixed	u theo.	v theo.
Individual light curves:						
2013, Mar 5	u’	0.13871 ± 0.00212	1.0910 ± 0.0	0.13947	1.0698	-0.2218
2014, Mar 15	u’	0.13989 ± 0.00282	0.9922 ± 0.0797	0.13793	1.0698	-0.2218
2014, May 28	u’	0.13627 ± 0.00263	1.1778 ± 0.0741	0.13914	1.0698	-0.2218
2014, Mar 15	B	0.13836 ± 0.00106	0.9428 ± 0.0301	0.13905	0.9154	-0.0592
2014, Feb 27	g’	0.13932 ± 0.00119	0.8046 ± 0.0346	0.13879	0.8492	-0.0122
2014, Mar 15	g’	0.13328 ± 0.00125	0.9074 ± 0.0359	0.13392	0.8492	-0.0122
2014, Mar 15	g’	0.13605 ± 0.00049	0.8662 ± 0.0143	0.13620	0.8492	-0.0122
2012, Feb 6	V	0.14103 ± 0.00244	0.7060 ± 0.0798	0.14180	0.6934	0.0961
2012, May 3	V	0.13615 ± 0.00179	0.6776 ± 0.0607	0.13661	0.6934	0.0961
2012, May 6	V	0.13821 ± 0.00221	0.8590 ± 0.0695	0.14114	0.6934	0.0961
2012, Jun 4	V	0.13783 ± 0.00251	0.6575 ± 0.0857	0.13785	0.6934	0.0961
2011, May 9	r’	0.13915 ± 0.00097	0.5350 ± 0.0370	0.13881	0.5831	0.1665
2011, May 25	r’	0.13951 ± 0.00103	0.6473 ± 0.0659	0.13923	0.5831	0.1665
2011, Jun 7	r’	0.13731 ± 0.00102	0.5796 ± 0.0397	0.13749	0.5831	0.1665
2011, Jun 23	r’	0.14187 ± 0.00122	0.5818 ± 0.0416	0.14164	0.5831	0.1665
2014, Mar 15	r’	0.13377 ± 0.00038	0.6047 ± 0.0129	0.13420	0.5831	0.1665
2011, Mar 29	R	0.13930 ± 0.00152	0.7328 ± 0.0484	0.14312	0.5450	0.1823
2011, Apr 14	R	0.14176 ± 0.00160	0.6319 ± 0.0579	0.14325	0.5450	0.1823
2011, May 13	R	0.14067 ± 0.00130	0.5322 ± 0.0767	0.14044	0.5450	0.1823
2011, Mar 9	R	0.13880 ± 0.00064	0.5977 ± 0.0213	0.13984	0.5450	0.1823
2012, Mar 19	R	0.13598 ± 0.00062	0.5806 ± 0.0161	0.13687	0.5450	0.1823
2007, Mar 27	i’	0.13931 ± 0.00205	0.2295 ± 0.1119	0.14029	0.4379	0.2198
2014, May 28	i’	0.13597 ± 0.00083	0.4786 ± 0.0310	0.13715	0.4379	0.2198
2007, Apr 25	z’	0.14047 ± 0.00107	0.3261 ± 0.0381	0.14018	0.3518	0.2426
2009, Feb 5	z’	0.14024 ± 0.00142	0.3633 ± 0.0532	0.14057	0.3518	0.2426
2013, Apr 5	F972	0.13893 ± 0.00188	0.3395 ± 0.0	0.13868	0.3518	0.2426
2010, May 31	J	0.13775 ± 0.00285	0.3660 ± 0.0637	0.14033	0.2200	0.3120
Combination of light curves per filter:						
	u’	0.13802 ± 0.00229	1.0910 ± 0.05573		1.0698	-0.2218
	g’	0.13615 ± 0.00064	0.8634 ± 0.01365		0.8492	-0.0122
	V	0.13815 ± 0.00111	0.7138 ± 0.03573		0.6934	0.0961
	r’	0.13611 ± 0.00068	0.5871 ± 0.01186		0.5831	0.1665
	R	0.13755 ± 0.00094	0.5908 ± 0.01711		0.5450	0.1823
	i’	0.13696 ± 0.00098	0.4804 ± 0.03088		0.4379	0.2198
	z’	0.14040 ± 0.00085	0.3395 ± 0.03262		0.3518	0.2426

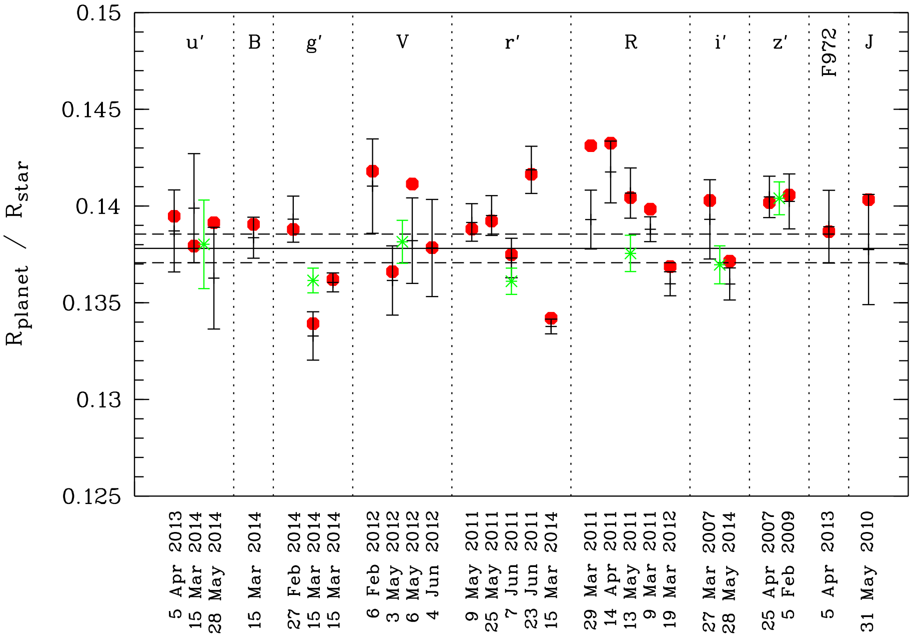

Fig. 4.8. The planet star radius ratio k for the indiviual transit light curves. Black crosses show k when the linear LDC u is a free fit parameter, red points show the same value when u is fixed to its theoretical value given in Table 4.5. Data points in green show the value of k for the simultaneous fit of multiple transits. The horizontal line shows the globally derived value of k as given in Table 4.3 and its uncertainty in dashed lines.

and was therefore not fitted simultaneously to the TNG and WHT u' band light curves (see Section 4.6.2). The light curve covers too little of the transit to constrain detrending and limb darkening in the same fit. Therefore, u was fixed to the value found in the simultaneous TNG + WHT u' band fit and perturbed during error estimation.

- R filter: The Lee data yield values which are systematically higher than the Asiago data and the mean k. We do not exclude these three light curves from the combined fit because we want to include as many transits as possible to average out uncorrected red noise. However, their exclusion would change the achieved value very little from 0.13755 ± 0.00094 to 0.13723 ± 0.00101. The final R band fit yields the highest deviation in u from the theoretical value with regard to the derived uncertainties, which also points towards strong influence of red noise. The deviation is $2.7\,\sigma$. Fixing u to its theoretical value changes k by $1.3\,\sigma$ to $k = 0.13882$.

- F972N20 filter: As for the simultaneously observed LBC u' band light curve, we fix u in the transit fit, but perturb it during the error estimation using the derived mean and $1\,\sigma$ uncertainty of the z' band light curves.

- J filter: The model fit differs from all other filters by the 5th order detrending polynomial, whose coefficients where all kept free in the fit and error estimation. There is a moderate correlation between k and each of the polynomial coefficients $c_{1,2,3,4,5}$ which results in a rather large uncertainty of k compared to other light curves of similar cadence and scatter. The obtained value $u = 0.3660 \pm 0.06375$ is discrepant by $2.3\,\sigma$ from its theoretical counterpart $u = 0.2200$. If u is fixed to this value, k changes by less than $1\,\sigma$ to $k = 0.14033$.

4.7 Results of the monitoring program and starspot correction

We monitored HAT-P-12 in the seasons 2012 and 2014 for about four months duration each in two colors V and I. The differential light curves are presented in Figure 4.9. A calculated Lomb-Scargle periodogram for V and I in 2012 found no compelling periodicity in this dataset. The periodogram of the V band data of 2014 showed indications for variations with a period of about 60 days. A fit of a sine curve with this period yielded a semi-amplitude of 1.8 ± 0.4 mmag. The I band data set of 2014 also shows mild indications for this period, but a period of about half this value, $P \sim 30$ days, is more significant. A sine fit yields an amplitude of 1.9 ± 0.3 mmag for the 30 days period and 1.4 ± 0.4 mmag for the period of 60 days. We calculated plain least-squares periodograms to estimate the amplitude of periodic sine and cosine functions over a wide period range and concluded that periodic signals of semi-amplitudes larger than about 2 mmag are excluded by the V and I data of 2014. For the observation period of 2012 we can exclude period signals of semi-amplitudes higher than about 1.5 mmag. An inspection of the light curves by eye reveals the strongest measured variation to be in the V band data of Season 2014 between Julian date 2456701 and 2456723. Here, the measured differential magnitude changes by almost 1%. As an upper limit, we estimate Δf, the difference of the measured stellar flux and the flux of the unspotted photosphere (Equation 2.17), for this value of extreme variation. Thus, $\Delta f \sim 1.3\%$, using again the variance of the long term light curve as an estimation of the level of the permanent flux dimming due to spots (see Section 3.3.6 for details). If we assume a temperature contrast between photosphere and spots of 1000 K, the filling factor would amount to ~ 0.015. Correspondingly, the maximum correction for unocculted spots ranges from about $\Delta k = -0.0004$ in the J band to about $\Delta k = 0.0015$ at u'. Note again, this correction is based on the 1% measured flux variation. If we assume that most of our transit observations took place at moments with much less flux variation and therefore smaller filling factors, the correction values are much lower than our derived error bars and can therefore be neglected.

Although the necessary correction for occulted spots would be higher, we list now our arguments why we adopt the uncorrected values for the plots and discussion regarding the transmission spectrophotometry:

- In none of our light curves we see indications for a bump caused by a starspot crossing (see also Section 4.5).
- Transits affected mostly by occulted spots are shallower than the average value. The transits of March 15, 2014 show a shallower transit in g' and r'. However, their simultaneously taken equivalents in B and u' are not shallower than the average value. Because the effect of occulted spots would be enhanced for this bluer wavelengths we conclude that the lower values of k in g' and r' are caused by different kinds of systematics.
- If the spots are not homogeneously distributed along the transit chord, they cause deformations which would be treated like red noise in our analysis, hence the uncertainty introduced by these spots is included in the uncertainty of the transit parameters.
- Even in the unphysical case of spots evenly distributed along the transit chord (resulting in a symmetric transit shape without bumps), the shallower transit curve would be discrepant from other transits. When analyzed simultaneously, this different shape would be treated like red noise to which our error analysis is sensitive.
- The monitoring campaigns have shown that the activity is time dependent with times of no measurable spot modulation. We interpret these times with very low

spot activity and assume that the simultaneous analysis of transits taken at different epochs weakens the influence of spots crossed at times of higher activity.

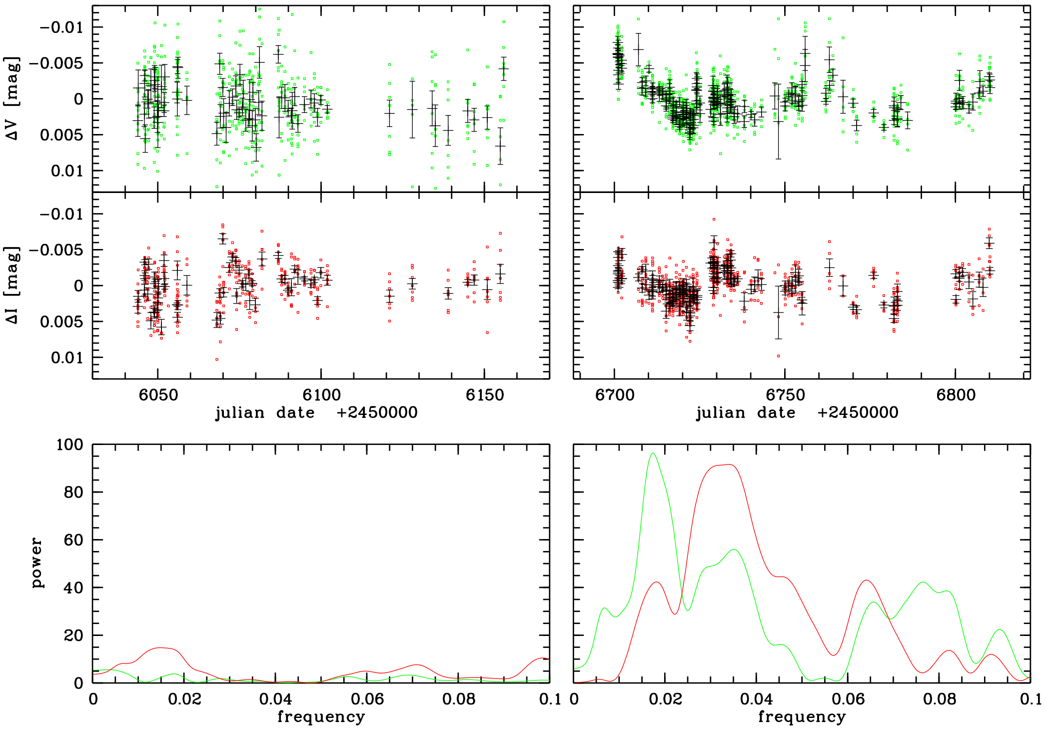

Fig. 4.9. Upper panel: STELLA/WiFSIP differential V band photometry with the original data points in green and the average of the five exposures taken as a block given in black with the error bars as the standard deviation divided by the square root of the number of averaged data points. On the left the observations from 2012 are shown, on the right the data from 2014. Middle panel: Same as in the upper panel, here for the I band photometry. Lower panel: The Lomb-Scargle periodogram for the V band data (green) and the I band data (red), on the left for 2012, on the right for 2014.

4.8 Discussion

4.8.1 Transmission spectrum

We compared the measured transmission spectrum to three different theoretical atmosphere models: The first model presents a cloud-free scenario and was computed by Fortney et al. (2010) using a planet-wide average P-T profile, solar metallicity and the planet parameters of HAT-P-12b. The second model simulates an atmosphere with a haze layer by the introduction of a Rayleigh-scattering slope of $dR_p/d\ln\lambda = -4H$ similar to the observed spectrum of HD189733b (Lecavelier Des Etangs et al. 2008a). H is the atmospheric scale height and equals $\sim$600 km in the case of HAT-P-12b. The third model is a simple flat line and represents an atmosphere dominated by clouds that cause gray absorption. We folded all models with the filter transmission curves and a theoretical spectrum of HAT-P-12 computed with the SPECTRUM spectral synthesis code (Gray & Corbally 1994) to obtain a theoretical value to which we compared our measurements by the $\chi^2_{\rm red}$ value. All three models were offset in the vertical direction until their mean from the B to the z' band equaled the measured k value of Table 4.3, $k = 0.13781$, see Figure

4.10. In this way, we defined the pressure level that defines the planetary radius. The achieved values were $\chi^2_{\mathrm{red}} = 2.40$ for the flat line model, 3.14 for the cloud-free model and 6.69 for the Rayleigh slope with the number of degrees of freedom equaling the number of data points minus one. The one-tailed probabilities of a χ^2 test are 8×10^{-3}, 5×10^{-4}, and $< 1 \times 10^{-5}$. This indicates that the measured data points disagree with all three models, but it is based strongly on the data points of the g', r' and z' band, which deviate from the mean k value by 2.6, 2.5 and $3.0\,\sigma$, respectively. Taking these data points for real would prove a wavelength dependence of the planetary radius. Following the arguments of Section 4.7 and assuming the star to have no significant influence on this result, the detection of a planetary atmosphere could be claimed.

However, in observational astronomy deviations of more than 3 σ are often called "outlier", attributed to unknown systematics and rejected. Here, a rejection of the z' band value changes the result dramatically: After a newly calculated vertical shift the χ^2_{red} value for the flat, cloud-free and Rayleigh model are now 1.1, 1.9 and 2.8, respectively. Thus, the data sample is in perfect agreement with the flat line and no detection of an atmosphere could be claimed anymore. However, the corresponding probability for the Rayleigh model of 3×10^{-3} still rules out this scenario. Note that this probability rises slightly if we take into account that a constant Rayleigh slope is unlikely to sustain over many scale heights due to grain settling (Pont et al. 2013). In the case of HD189733b, the Rayleigh slope is constant from the UV to the z' band (Sing et al. 2011b), but weakens at redder wavelengths until k reaches a constant value at about the H or K band (Pont et al. 2013). To simulate this effect we adjust the same value of k for the J band as for the F972N20 filter for the Rayleigh slope model, which changes χ^2_{red} to 2.5 and increases the probability to 8×10^{-3}. For completeness we want to emphasize that the low likelihood of the Rayleigh slope model is strongly based on the two data points of the F972N20 and J band filter. Excluding these in addition to the z' band point and comparing the remaining eight Near-UV and Optical data points to the Rayleigh slope model results in a fair agreement of $\chi^2_{\mathrm{red}} = 1.8$ and $P = 0.08$. We would also like to mention that fixing u to its theoretical value would further reduce the agreement of the measurements with the Rayleigh slope model since all data points remain nearly unchanged except the point at J, which increases by about $1\,\sigma$.

In a previous study, Line et al. (2013) obtained a transmission spectrum from 1.1 to 1.7 μm which clearly rules out the presence of the broad water absorption feature at 1.4 μm. We combined the two sets of transmission measurements into one plot in Figure 4.11 with a vertical offset for the Line et al. (2013) data of 0.00129 to match the cloud-free model. Line et al. (2013) concluded that clouds in the atmosphere are the physically most plausible scenario to explain their rather flat spectrum. The NIR measurements do not allow for a conclusion regarding the Rayleigh slope since such slope might not extend into this wavelength regime due to grain settling. The data sample of this work could not distinguish between the flat and the cloud-free model. Therefore, the two data sets cannot confirm each other, instead they are complementary. Of the three discussed atmospheric scenarios, the cloud-free model, the flat cloudy model and the hazy model with Rayleigh-scattering, we can exclude the first and the third. A flat transmission spectrum caused by clouds without Rayleigh slope is the most likely scenario for HAT-P-12b.

HAT-P-12b has an equilibrium temperature of about 1000 K. Theoretical models of Hot Jupiter atmospheres predict cloud-free atmospheres as clouds should form below the probable altitude by dust condensation (see Madhusudhan et al. 2014, and references therein). However, HAT-P-12b is not the only Hot Jupiter of this temperature regime that does not fulfill the theoretical predictions. The works on transmission spectroscopy of Gibson et al. (2013a) on WASP-29b and of Nikolov et al. (2014) on HAT-P-1b together with the analysis of HAT-P-19b in Chapter 3 all disfavor clear atmospheres. Although for

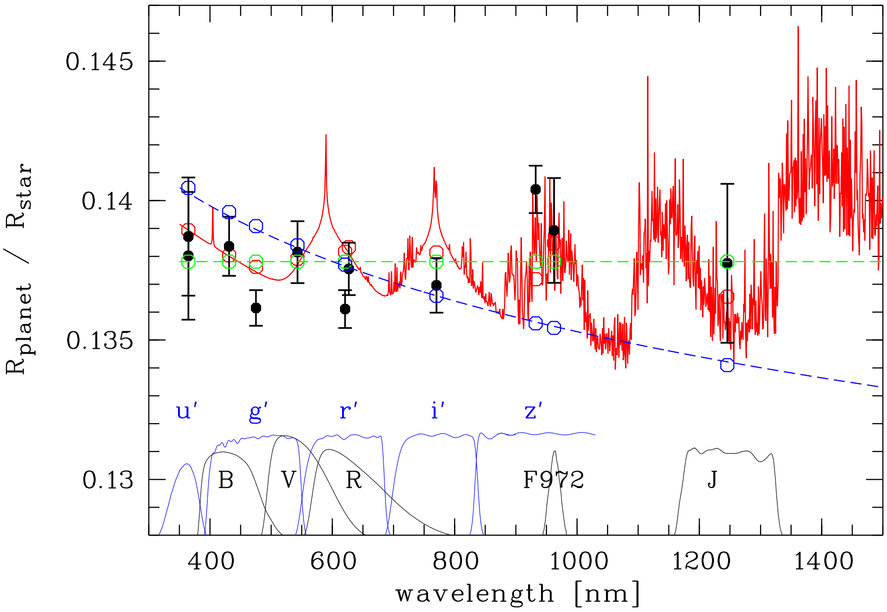

Fig. 4.10. Broad-band transmission spectrum of HAT-P-12b. The measured values are given in black. Overplotted are a cloud-free solar metallicity spectrum of HAT-P-12b from Fortney et al. (2010) (red solid line), a Rayleigh-scattering slope $dR_p/d\ln\lambda = -4H$ (blue solid line) and a flat line presenting wavelength-independent atmospheric absorption (green solid line). The model values when folded with the filter transmission curves and a theoretical spectrum of HAT-P-12 are given in their corresponding color as open circles. At the bottom the transmission curves of the used filters are shown.

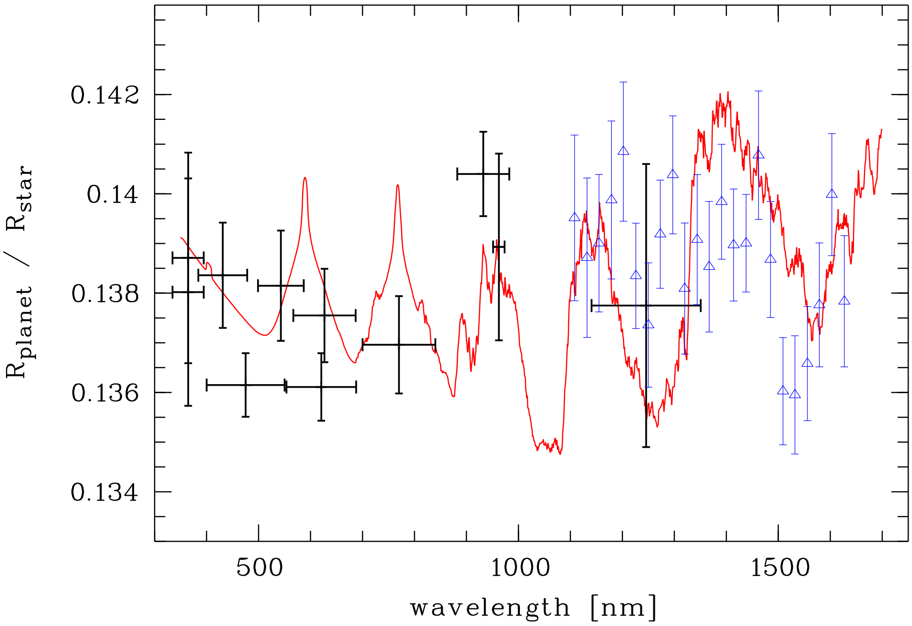

Fig. 4.11. Transmission spectrum of HAT-P-12b combining the measurements of this work (black) with the HST measurements of Line et al. (2013) (blue triangles). The data from Line et al. (2013) were vertically shifted by 0.00129 to match the modeled cloud-free transmission spectrum of Fortney et al. (2010) (red solid line). The cloud-free scenario is ruled out to 4.9 σ (Line et al. 2013).

each case there might be individual explanations, one scenario eases the interpretation of all these observations: the slant viewing geometry of this observing technique through the planetary atmosphere strongly enhances the opacities of condensates. Even in extremely low concentrations, such dusty material can make the atmospheres optically thick (Fortney 2005). Therefore, opaque atmospheres could be the normality and the detection of broad absorption features in exoplanet atmospheres the exception.

4.8.2 Other broad-band spectrophotometry studies

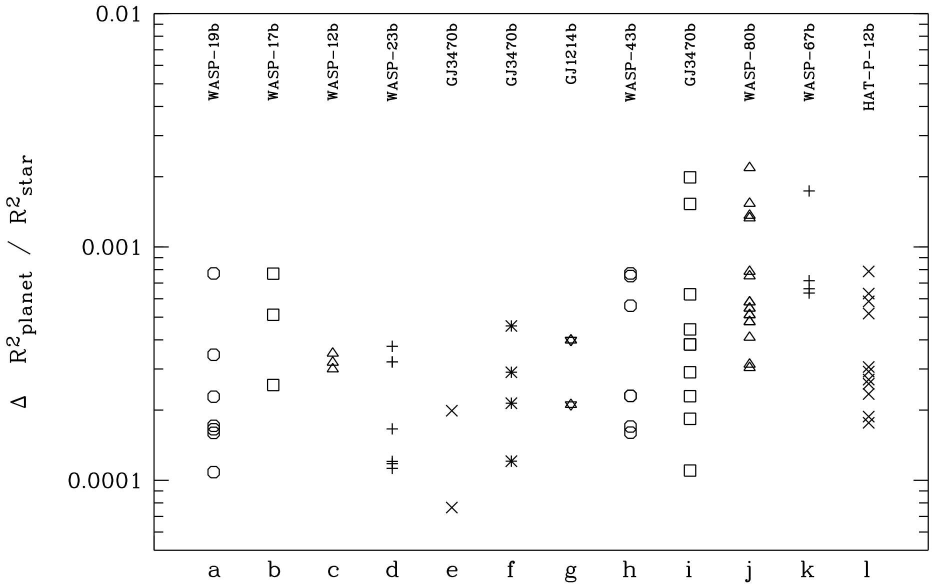

Fig. 4.12. Comparison of the achieved uncertainty of the transit depth $k^2 = R_p^2/R_\star^2$ given in the literature of broad-band transmission spectroscopy. This list is not exhaustive and the sequence along the abscissa is arbitrary. a: Mancini et al. (2013a), b: Bento et al. (2014), c: Copperwheat et al. (2013), d: Nikolov et al. (2013), e: Nascimbeni et al. (2013b), f: Fukui et al. (2013), g: de Mooij et al. (2013), h: Chen et al. (2014), i: Biddle et al. (2014), j: Fukui et al. (2014), k: Mancini et al. (2014a), l: this work.

The capability to constrain theoretical models of exoplanet atmospheres is a matter of the accuracy that a transit observation can reach. For a comparison we compiled the uncertainties that similar investigations of ground-based broad-band spectrophotometry achieved for the measured planet-star radius ratio. As visible in Figure 4.12, several studies reached lower uncertainties than we presented here. We like to discuss now why we think that our results are robust.

All the values that currently form the best ground-based measurements of the planet-star radius ratio k (Nascimbeni et al. 2013b; Mancini et al. 2013a; Nikolov et al. 2013; Fukui et al. 2013; Biddle et al. 2014) were derived by fitting single transit light curves. In our analysis, the majority of single transit fits obtain higher uncertainties in the MC error estimation (not sensitive to red noise) after β factor inflation, whereas the simultaneous fit of multiple transits reaches mostly higher error bars with the red noise sensitive residual-permutation (RP) method. This might be caused by the fact that the full amount of systematics contained in a light curve can be better revealed by multiple measurements and than better accounted for by the RP error estimation than with the β factor inflation. For single transit measurements, parts of the systematics might be compensated by a different transit model and therefore remain unrecognized by the error estimation, especially these parts of systematics that do not change the symmetry of a transit. The only way here to learn whether an obtained result is robust or not are repeated measurements.

We binned the individual transits of g', r' and R per filter in phase and formed single, high-precision (0.40 mmag rms per 1 minute bin in r') light curves to test the hypothesis that the error bars of single transit measurements tend to be underestimated. We obtained uncertainties Δk smaller by factors of 1.7 to 2.3 than the uncertainties given in Table 4.5 for the simultaneous fit of the multiple transits. This result is confirmed by the circumstance that for these filters the best quality individual light curves give a smaller uncertainty than the combined analysis.

Thus, there are two important advantages of repeated transit measurements, both dealing with the fact that systematics (either intrinsic, atmospheric or instrumental) are better revealed if multiple measurements exist: First, the effect of systematics decreases with more observations since the systematics average out, therefore the derived transit parameters become more robust. And at second, the uncertainties become more reliable.

Another striking fact about the transit parameter uncertainties in the modern literature is that although high standards are used in recent transit photometry publications, the derivation of reliable parameter uncertainties seems to remain a tricky business. The parameter uncertainties derived in this work in the re-analysis of literature light curves provided uncertainties which were in their majority significantly different from their published values. Typically, they were larger by a factor of 2, but we also encountered a case of an error value larger by a factor of 10. Another example for different error bars for the same data sets can be easily found in the literature: the light curves which were used for the currently most accurate (to our knowledge) ground based measurement of k by Nascimbeni et al. (2013b) (see Figure 4.12) and the GJ3470 light curves from Fukui et al. (2013) were re-analyzed by Biddle et al. (2014), who found error bars which are higher by a factor of 1.5 for the Nascimbeni light curves and uncertainties up to 3 times larger for the light curves of Fukui et al. (2013). To obtain a third result, we also re-analyzed the Fukui data and got values for Δk always higher than the uncertainties of Fukui et al. (2013), but partly larger, partly smaller by a factor of 1.5 than the uncertainties derived by Biddle et al. (2014). This variation in Δk is caused by its sensitivity to many details in the analysis, beginning with the photometric errors in the light curve, continuing for example with the light curve detrending, the different treatment of the fit parameters, the handling of the stellar limb darkening and ending with the different used error estimation algorithms (Monte Carlo simulation, bootstrapping, residual-permutation, MCMC, etc.). The discrepancy in the error bars is especially worrisome as the detection of a planetary atmosphere or the attempt to constrain atmospheric models is at the very edge of what can be done with current ground-based facilities. The results depend crucially on the parameter uncertainties and would change significantly in most investigations if the error bars were inflated or decreased by a factor of 2.

4.8.3 Periodicity in the monitoring light curves

The V band light curve of the season 2014 presented in Section 4.7 showed a periodicity of ~ 60 days, the I band one of ~ 30 days, thus the question arises if these are linked to the stellar rotation period. The semi-amplitude for both of the order 1-2 mmag are too small to claim significance, because they are well in the regime of systematic effects. One way to verify this signal is the investigation of independent photometric data sets. Therefore, we downloaded the monitoring data of HAT-P-12 of the SuperWASP survey from the NASA Exoplanet Archive[4] observed in 2007 and found a periodicity of ~ 65 days, here with a

---

[4] exoplanetarchive.ipac.caltech.edu/docs/SuperWASPMission.html

slightly larger amplitude of about 3 mmag. However, not far from this period the window function of this data set has a moderate peak at ~ 80 days. We also analyzed the discovery light curve from the HATnet survey, taken in 2006 and another HATnet monitoring of this object from the year 2010, both made available at the HATnet homepage[5]. Their precision rules out significant periods with amplitudes higher than about 4 mmag, but do not allow for any statement about the potential periods at 30 and 60 days. Therefore, we are not confident about the detection of the stellar rotation period.

---

[5] hatnet.org/planets/discovery-hatlcs.html

5 Transmission spectroscopy of HAT-P-12b and HAT-P-32b with MODS@LBT

5.1 Introduction

Low-resolution spectrophotometry with large-aperture telescopes as presented in Chapter 3 is complementary to broad-band spectrophotometry using small- to mid-aperture telescopes as presented in Chapter 4. While broad-band spectrophotometry is sensitive to overall trends and gradients in the spectrum like a Rayleigh slope, it cannot resolve narrower spectral features as for example the sodium and potassium absorption predicted for cloud-free Hot Jupiter atmospheres. Here, we present the search for the pressure-broadened Na and K absorption using transit observations of the optical multi-object spectrograph MODS at the Large Binocular Telescope (LBT). Our goal was to complement the analysis of Chapter 4 of HAT-P-12b. Furthermore, we wanted to compare the achieved result of this 1000 K hot gas giant with observations of the same kind of another very favorable target, HAT-P-32b. This Hot Jupiter is much hotter with $T_{\mathrm{eq}} \sim$ 1800 K.

The discovery of HAT-P-32b was announced by Hartman et al. (2011b). The Hot Jupiter was among the first exoplanet candidates of the HATnet survey with discovery photometry dating back to 2004. However, the object proved difficult to confirm because of a high radial velocity jitter of about $\sim$80 ms^{-1}. HAT-P-32b has a mass of about 0.9 $\mathrm{M_{Jupiter}}$ and a radius of about 1.8 $\mathrm{R_{Jupiter}}$, making it one of the most bloated planets found to date. The host is a F-type main-sequence star of V = 11.3 mag, with a mass of 1.16 $\mathrm{M_\odot}$ and a radius of 1.22 $\mathrm{R_\odot}$ (Hartman et al. 2011b). Although substantially more high S/N spectra were taken for the radial velocity curve than for typical HATnet candidates, the planet's eccentricity e could not be well constrained due to the jitter, $e = 0.2^{+0.19}_{-0.13}$ (Knutson et al. 2014b). Because of the planet's high T_{eq} of about 1800 K and the large scale height H of about 1100 km, HAT-P-32b is a very favorable target for transmission spectroscopy as illustrated in Figure 2.2.

The orbital plane of HAT-P-32b was found to be misaligned to the stellar spin axis with a projected angle of 85 ± 1.5 degrees (Albrecht et al. 2012), which could be an indicator for an inward migration caused by multi-body interactions (Wu & Murray 2003). A projected near-by star was found by Adams et al. (2013) just 2.9" away. It is unclear if both stars are physically associated, however, for transmission spectroscopy this object might be important. Depending on the size of the photometric aperture its light influences the derived transit parameters as third light contribution.

Knutson et al. (2014b) confirmed a trend in the radial velocity measurements of HAT-P-32, which indicates an additional massive companion at several AU semi-major axis. The imaged near-by star found by Adams et al. (2013) is too distant to explain the RV trend, hence it might be that HAT-P-32 has two massive outer companions. Seeliger et al. (2014) performed a TTV analysis to search for additional close-in planets in resonant periods to HAT-P-32b which in part might be responsible for the RV jitter. Their sensitivity reached the super-Earth mass level, but none was found.

A first transmission spectrum of HAT-P-32b in the optical was obtained by Gibson et al. (2013b). They used two Gemini-North GMOS transit observations to rule out pressure-broadened absorption features of sodium and potassium. The achieved featureless spectrum could be best explained by a cloud coverage of the planetary atmosphere. Chapter 3 taught us that current attempts of ground-based transmission spectroscopy are at the edge of the instrument capabilities and Chapter 4 proved how vulnerable the drawn conclusions can be on systematics in the light curves. Therefore, we were interested if the results of Gibson et al. (2013b) could be reproduced with a new data set and an independent analysis.

Hartman et al. (2011b) argued that the high RV jitter is probably not caused by brightness (temperature) inhomogeneities on the stellar surface. Instead, it might be caused by convective inhomogeneities which vary in time. However, we monitored the host star HAT-P-32 with STELLA/WiFSIP during two observing seasons to be sure that the transit parameters are not affected by starspots.

5.2 Transit observations with MODS

We were awarded with LBT observing time for one transit event of HAT-P-12b in the seasons 2011A and 2012A. While no observation could be executed in 2011, we gathered data in the night of April 23, 2012. The transit lasted from 05:48 to 08:08 UT. Unfortunately, we lost the beginning due to weather and started the time series at 06:54 UT, which was about the mid time of the transit. The time series finished at 09:15 UT.

The observation was performed with the Multi-Object Double Spectrograph (MODS, Pogge et al. 2010), a low- to medium-resolution optical spectrograph/imager. MODS covers a field of view (FoV) of 6×6 arcminutes^2. We employed the instrument in its dual-channel mode, i.e. the incoming light beam is split by a dichroic into separate red- and blue-optimized channels at a wavelength of 565 nm. A wavelength region from 340 to 1000 nm is covered in one shot. We used the multi-object spectroscopy mode (MOS) in which multiple stars are observed simultaneously through a user-designed slit mask. Next to the target we took spectra of the objects GSC-0303300996 and GSC-0303300754. As dispersive element we chose a grating. Both channels are equipped with e2v 3K×8K CCD detectors, differently coated for the blue and the red arm, which are read-out by eight amplifiers each. At the moment of observation the telescope control software was not yet able to allow for binocular observations with MODS, therefore we used the binocular telescope in "one-eye" mode. For high-accuracy spectro-photometry we wanted to be sure that we loose a negligible amount of flux at the edge of the slits. Due to pointing and seeing variations this light loss would be variable and could potentially manifest as significant noise source in the resulting light curves. Therefore, we designed 10 arcseconds wide slits for the MOS mask. The length of the slits was 30 arcseconds to allow for a proper skylight correction.

The exposure time of our time series of HAT-P-12 was 60 seconds. To reduce the dead time between consecutive exposures we binned 2×2 pixels on-chip resulting in overheads of 51 seconds in the red arm and 57 seconds in the blue. Hence, we obtained 78 and 73 exposures, respectively. The airmass evolved from 1.02 to 1.15, the seeing was 1 arcsecond and slightly below. Typically, we reached a signal-to-noise ratio of about 190 per pixel in dispersion for exposures of the blue arm and 380 for the red exposures. The object drifted by about 1 pixel/hour in spatial and dispersion direction. Despite the weather problems during the first half of the transit, the conditions were photometric during the observed time series.

Similar to the HAT-P-12 observation, an awarded five hours observation of HAT-P-32 could not be executed in the year 2011, either. We successfully obtained transit data in 2012, November 13. The MODS observation started at 04:36 UT and lasted until 09:49 UT. The last exposures of the red arm could not be transfered to the data archive because of technical problems, hence the red time series ended already at 09:29 UT. The transit happened between 05:43 and 08:49 UT. All spectroscopic frames were exposed for 30 seconds, together with the overheads of 44 and 49 seconds this resulted in a cadence of 74 and 79 seconds for the red and blue arm, respectively. Again, a 2×2 pixel binning was applied on-chip. The time series consisted of 238 frames in blue and 240 frames in red. The night was clear and offered photometric conditions, the seeing varied between 1.0 and 1.5 arcseconds. The airmass increased from 1.03 to 1.39 during the observation. Simultaneously to the target HAT-P-32, we observed four reference stars. In this work we concentrate on the two brightest stars, GSC-0328100957 and GSC-0328100900. As in the HAT-P-12 observation with MODS, we used 10 arcseconds wide slits in the user-designed slit mask. The object drifted by about 3 pixel in both spatial and dispersion direction over the length of the time series. Per exposure the target achieved a signal-to-noise of about 260 per pixel in dispersion in the blue MODS channel and about 370 in the red channel.

5.3 Data reduction of the MODS data

The data reduction of the MODS spectra was similarly done to the reduction of the OSIRIS long slit spectra described in Section 3.2.1. Examples of extracted spectra of HAT-P-12, HAT-P-32 and their comparison stars are shown in Figure 5.1 and 5.2. The multi-object spectra were treated as multiple long slit spectra and reduced using the same ESO-MIDAS scripts. We did not employ the official MODS Spectral Data Reduction Pipeline because it does not support our non-standard 2×2 binning read-out mode. The bias and flat field correction was done in a usual way. However, special care had to be given to an odd/even column pattern resulting from the two read-out amplifiers per quadrant of the MODS CCD, each having its own bias and gain level. The bias level per amplifier was extrapolated from the overscan regions on both sides of the data frames, flat field exposures were taken at the same day as the science frames using gas lamps. We averaged 30 flat field exposures to create a master flat.

The dispersion direction of the spectra is misaligned to the pixel rows of the detector, we rebinned the spectra in spatial direction for alignment. Over the rather short extent of the spatial slit length, the sky lines were not bent and followed the pixel columns. Therefore, a rebinning in dispersion direction or a 2-dimensional wavelength calibration as done for the OSIRIS data in Section 3.2.1 was not necessary. Wavelength calibration spectra were obtained with a different slit mask: The slit positions and lengths were the same as in the science mask, whereas the width was reduced to $1''$ to avoid impractically broad lines. The wavelength calibration included a shift in dispersion to correct for a pixel drift of about 2 to 4 pixel over the time series. For both data sets of HAT-P-12 and HAT-P-32 we estimated the spectral drift by the centroid measurements of prominent stellar lines. We compared these values to the centroid shifts of telluric absorption lines and found no difference. According to the wavelength solution of the arc lamp exposures and the scatter of the residual line positions in wavelength, the accuracy of the wavelength calibration is better than 0.3 Å.

We simply summed the flux within a FWHM-dependent aperture and compared it with the flux extracted with the optimal extraction technique of Horne (1986). As in the reduction of HAT-P-19 in Section 3.2.1, we found the simple flux sum to yield light curves with lower scatter, hence a more robust spectrophotometry. Again, we tested which object aperture and width of sky stripes minimizes best the rms of the light curve residuals after a transit model subtraction using literature transit parameter. This resulted in an aperture of 5.5 times the spatial FWHM in the blue arm and 6.5 times the spatial FWHM in the red arm. Note, these apertures involve most of the flux of the faint companion of HAT-P-32 at 2.9” distance, we discuss its influence in Section 5.5. Interestingly for the sky subtraction, we did not find the widest sky stripes to give the lowest scatter in the light curves as in Section 3.2.1. Instead, rather small stripes of 10 pixel width on both sides yield the best quality despite their higher photon noise. We think this is caused here by the fact that wider sky stripes need to approach the spectral centroid closer because of the limited spatial extension of the spectra. Thus, wide sky stripes contain more target light of the wide spectral profile wings resulting in an erroneous sky determination.

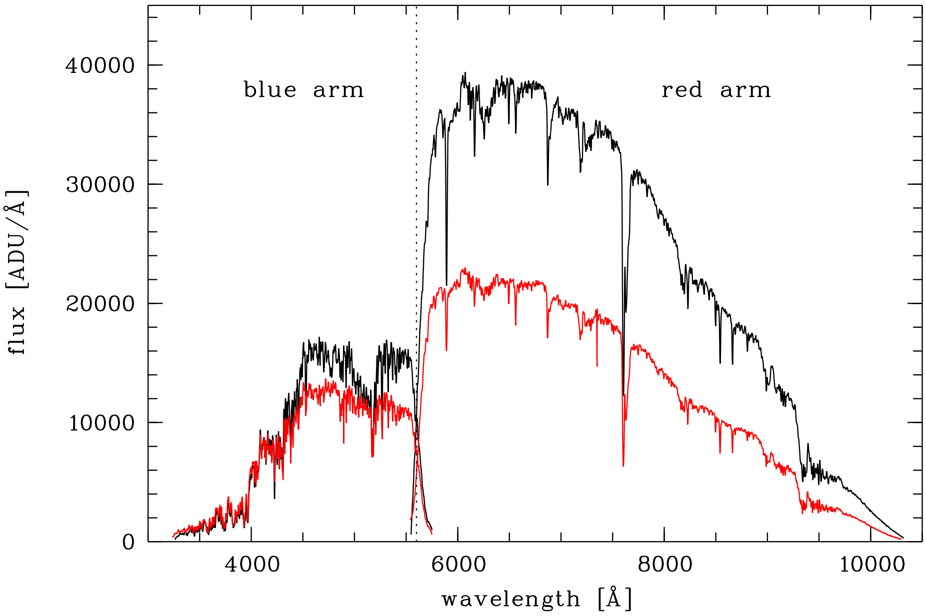

Fig. 5.1. Spectra of HAT-P-12 in black and the comparison star in red of a single exposure. The wavelength separation of the blue and the red arm of MODS at 5650 Å is indicated by a vertical dotted line.

Differential spectrophotometric light curves were created from the flux of target and comparison stars in wavelength channels of 100 Å width. We tested which of the comparison stars could minimize the rms of the light curve residuals or if their combination yielded the best light curves. For HAT-P-12, the usage of the brighter comparison star alone gave the least photometric scatter, while for HAT-P-32 the choice was wavelength dependent. The photometric error values were calculated using Equation 3.1. In Figure 5.3 and Figure 5.4 the chromatic set of light curves are presented for HAT-P-12b and HAT-P-32b, respectively. Overplotted are the best fit transit models derived in Section 5.6.

5.4 Monitoring of HAT-P-32

Between December 2011 and March 2013 we monitored the host star HAT-P-32 with STELLA/WiFSIP in the filter Johnson B and Sloan r’. In total, we obtained 2456 and 2442 images in these two filters. The images were obtained in blocks of three frames in B plus three frames in r’ with an exposure time of 15 seconds each. If the conditions allowed for it, multiple blocks have been taken per night. In total, the telescope observed HAT-P-32 in 180 individual nights. We read out the full FoV of 22×22 arcminutes^2 and applied no defocus.

The data reduction has been done in the same way as for the WiFSIP monitoring data of HAT-P-19 and HAT-P-12 as described in Section 3.2.2 and 4.3.2. The automatic search for the comparison star combination, which minimizes the scatter in the target light curve, ended with the selection of seven comparison stars in r’ and 11 stars in B,

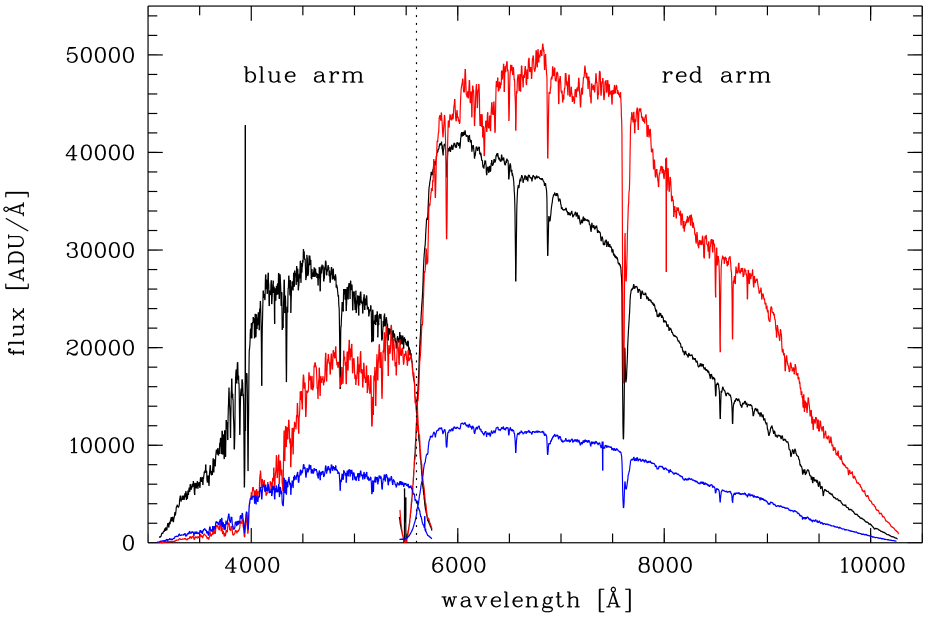

Fig. 5.2. Spectra of HAT-P-32 (black), comparison star 1 (red) and comparison star 2 (blue) of a single exposure. The wavelength separation of the blue and the red arm of MODS at 5650 Å is indicated by a vertical dotted line.

preferably near-by to the target, but from three of the four read-out amplifiers. We verified that the Lomb-Scargle periodograms of Figure 5.6 are not significantly influenced by the comparison star selection. The data points were selected against a peak count rate of the target higher than 60 000 ADU, a flux rate significantly lower than 50% of average, an unusual high sky background, an exceptional FWHM (focus problems) and abnormal PSF shapes. The final light curves encompassed 1567 and 1730 data points in B and r', respectively.

We subtracted an offset between the two observing seasons (jd $\approx$ 2456048) present in both filters of about 4 mmag. Interestingly, the light curves in Figure 5.5 and the Lomb-Scargle periodograms in Figure 5.6 show that the transit dip is detected with the correct periodicity, meaning that the candidate status of a transiting exoplanet could have been given to HAT-P-32b with these monitoring data alone. In principle, a WiFSIP monitoring program like ours on a more densely populated stellar field could be used to search for transiting close-in giant planets.

After the subtraction of a transit model using fixed literature transit parameters the peaks associated with the orbital period disappeared from the Lomb-Scargle periodograms. The scatter (rms) of the unbinned data is 4.6 and 4.1 mmag in B and r', respectively. No additional significant periodicity could be found. If sine functions are fitted to smaller peaks in the transit-cleaned r' band periodogram, for example at about 0.2 and 0.1 cycles per day, the obtained corresponding semi-amplitudes are $\sim$1 mmag. We believe that variations of such amplitudes might be influenced by measurement systematics and are not trustful. A plain least-squares periodogram used to estimate the amplitude of periodic sine and cosine functions over a wide period range confirms that no semi-amplitudes larger than about 1 mmag are present in the data.

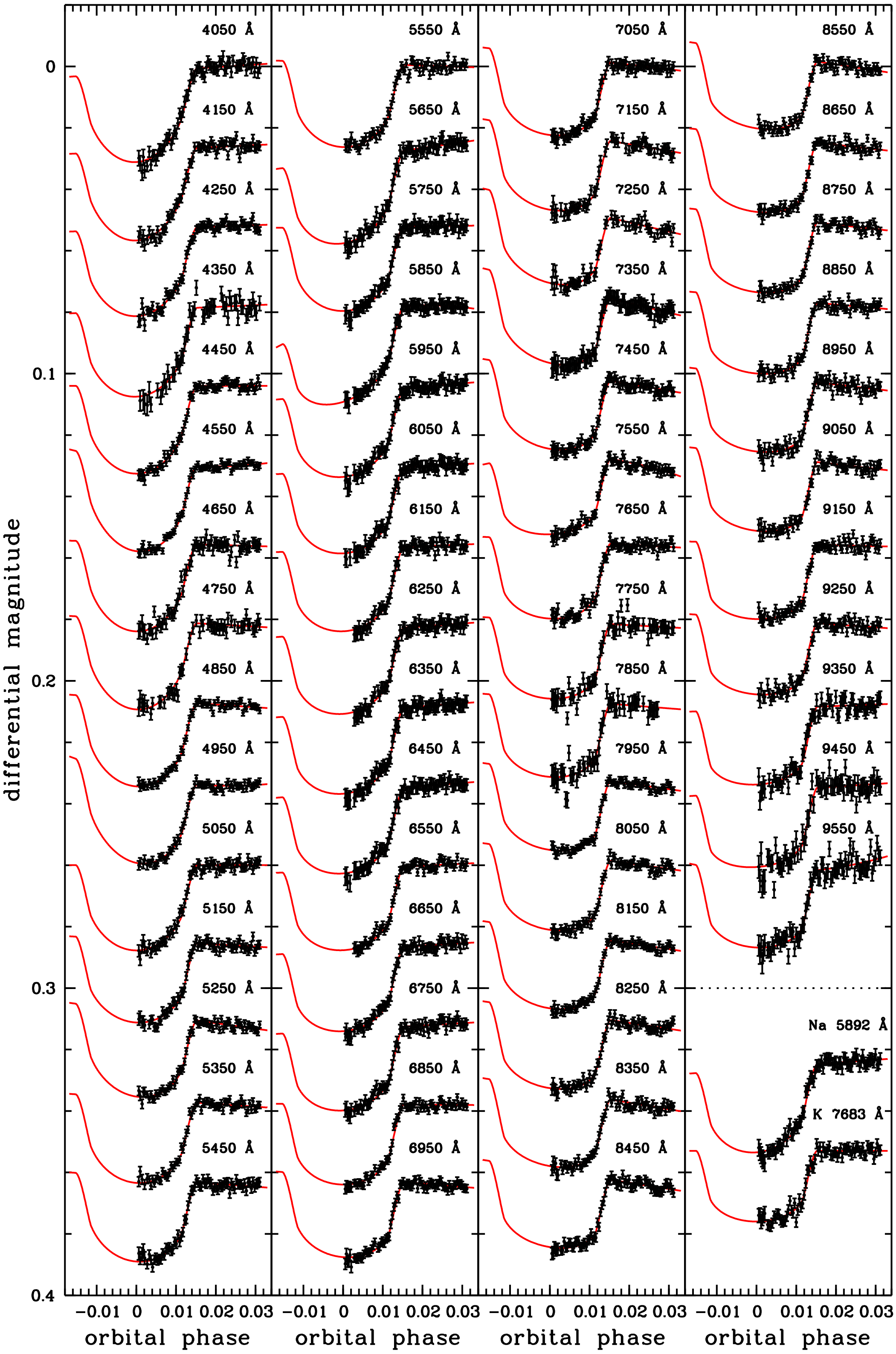

Fig. 5.3. Simultaneously taken transit light curves of HAT-P-12b extracted from the MODS spectra in 100 Å wide wavelength channels. Overplotted in red are the best fit transit models. At the bottom of the right column the light curves centered at the sodium and potassium features are presented. They are extracted in 50 Å wide wavelength channels. Characteristics of all light curves are given in Table 5.1.

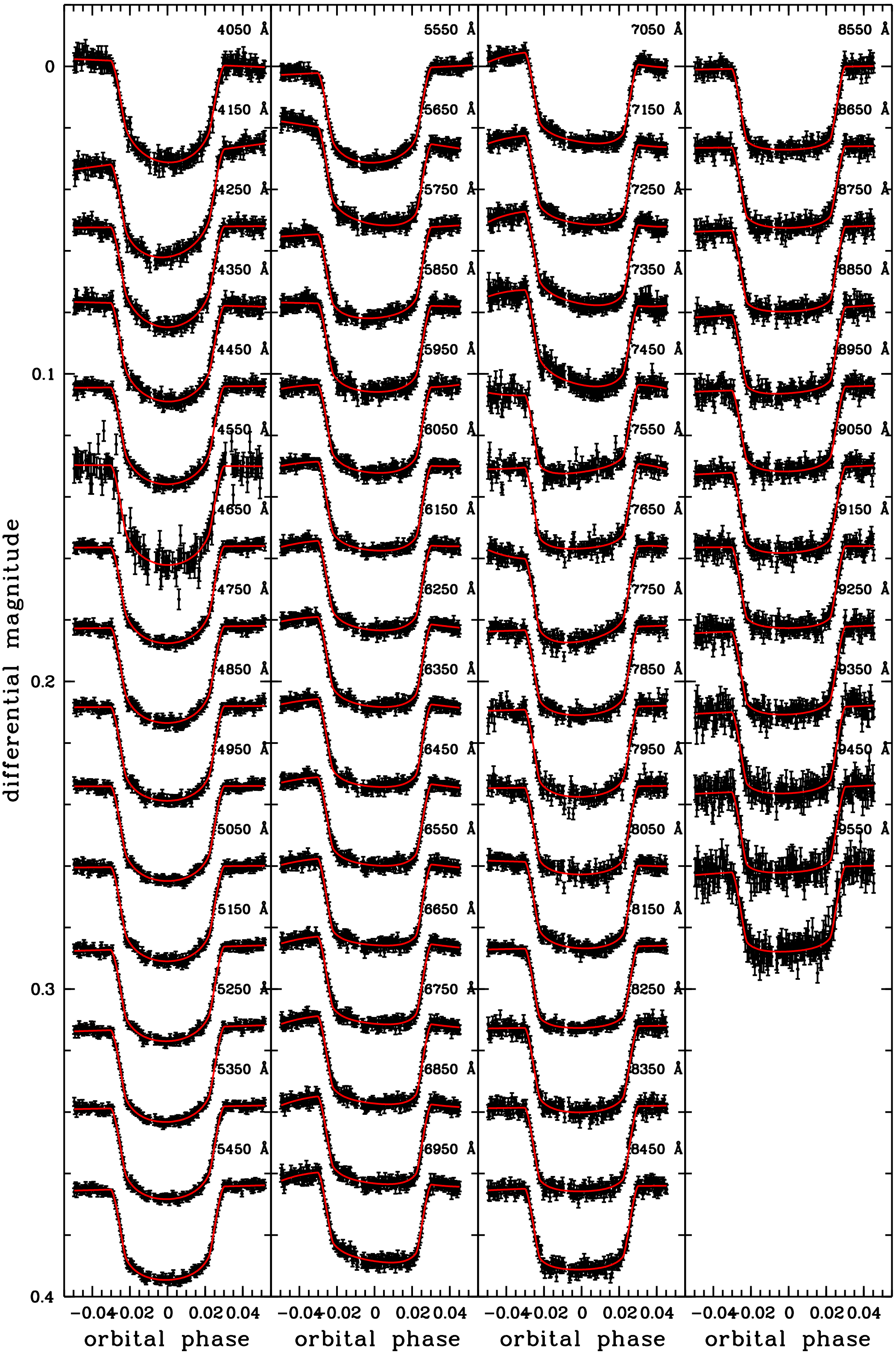

Fig. 5.4. Simultaneously taken transit light curves of HAT-P-32b extracted from the MODS spectra in 100 Å wide wavelength channels. Overplotted in red are the best fit transit models. Characteristics of all light curves are given in Table 5.2.

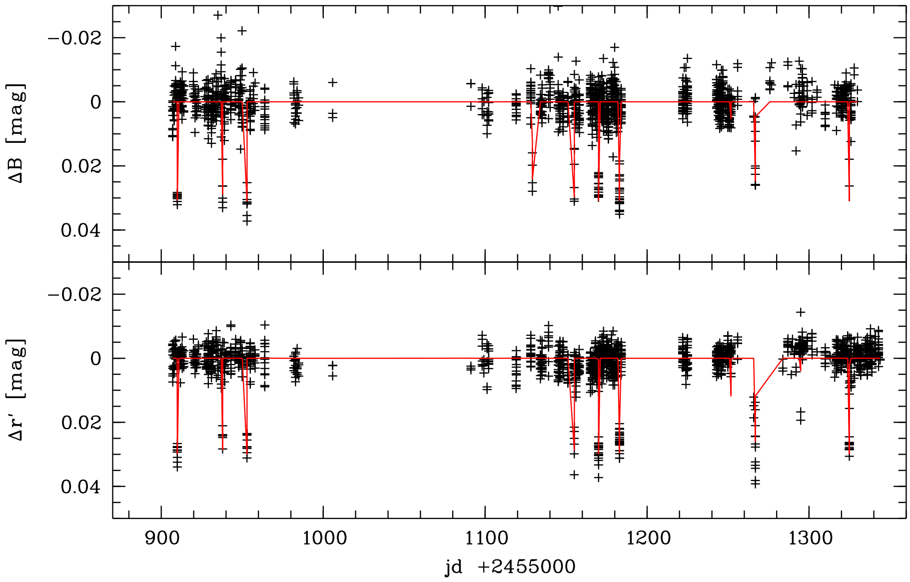

Fig. 5.5. Monitoring light curves of HAT-P-32 in Johnson B and Sloan r' from STELLA/WiFSIP. The in-transit data points observed by chance can easily seen by eye. In red, a transit model using literature transit parameters is overplotted.

5.5 HAT-P-32: Correction for starspots and M dwarf companion

In Section 4.7 we described our monitoring program of HAT-P-12 and concluded, that a spot correction is not needed for the transit parameters of HAT-P-12b. Following the same arguments, we do not apply a spot correction for HAT-P-12b here. In the case of HAT-P-32b, we did not measure a significant photometric variability of the host star either, see Section 5.4 for details. The derived upper limits on photometric amplitudes are most plausible explained by the lack of temperature inhomogeneities large enough to influence our transit parameters significantly.

In a separation of only 2.9 arcseconds to HAT-P-32, Adams et al. (2013) found another object which is fainter in the K band by 3.4 magnitudes. This magnitude difference corresponds to a light contribution of the near-by object (third light) of ∼4.5%. Third light has the opposite effect to unocculted starspots on the transit parameters (which is discussed in Section 2.4) and dilutes the transit depth. We can use Equation 2.18 to correct for it, but we need to know Δf as a function of wavelength. Here, Δf is the amount of third light in relation to the integrated flux. Simply spoken, a third light contribution of 4.5% in the K band would damp the true transit depth by the same amount of 4.5%. Gibson et al. (2013b) integrated their spectral flux in a narrow aperture to avoid the majority of the companion flux. Both spectra could be resolved and the near-by object was identified as a M dwarf (Gibson et al. 2013b). However, we tested many aperture width and found a rather wide aperture of $6.5 \times$ FWHM to give the most stable photometry. Hence, the light of the companion is fully included in our aperture. We approximated the third light contribution Δf with the ratio of the peak intensities of the spectral profiles of both objects. A plot of this intensity ratio over wavelength in steps of ∼40 Å is presented in Figure 5.7. Because the peak of the M dwarf is influenced by the wings of the PSF of HAT-P-32, we removed HAT-P-32 from the spectral profile: The spectral profile was rebinned in spatial direction to move the centroid of a Gaussian

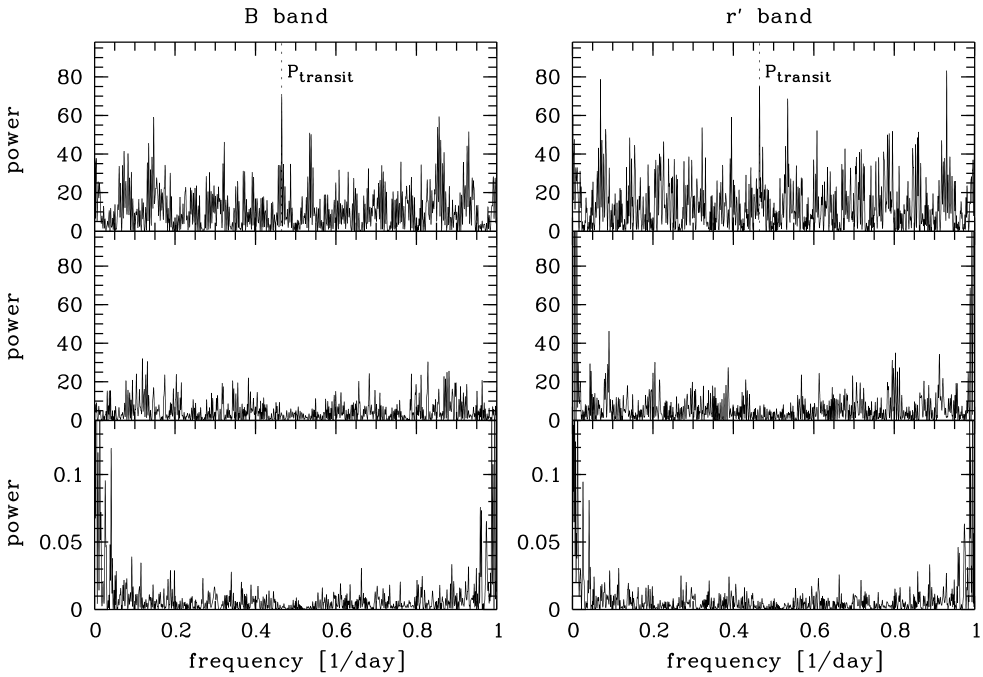

Fig. 5.6. Lomb-Scargle periodogram of the monitoring light curves of HAT-P-32. On the left the B band data are analyzed, on the right the periodogram of the r' band light curve is shown. From top to bottom: The Lomb-Scargle periodogram of the original data sets with a peak clearly visible at the known orbital period of the planet, a periodogram of the data after a transit model subtraction and the window function. No significant periodicity could be identified after the transit model subtraction.

function fitted to HAT-P-32 onto a pixel edge. Then, the side of the profile opposite to the M dwarf got mirrored and subtracted from the side of the profile containing the companion profile. We estimated the third light contribution only on the red MODS data, because at blue wavelengths the influence of the M dwarf is negligible. Our derived values are in very good agreement to previous estimations (Hartman et al. 2011b; Adams et al. 2013; Gibson et al. 2013b), but span a wider wavelength range. At the reddest light curves of our sample, the transit depth needs to be corrected by almost 2%, which is about the size of the transit depth uncertainties.

5.6 Analysis of transit light curves

We observed both objects HAT-P-12 and HAT-P-32 simultaneous to multiple comparison stars. For HAT-P-12, we obtained spectra of two reference stars, together with HAT-P-32 we observed four other stars along the time series. Two of these four stars had flux rates lower by a factor of 4 compared to the target, therefore they are not included in this work. The first step of the transit analysis was to decide which comparison star to use to form differential light curves. Here, we created three versions of each light curve, one per comparison star and a third version with the flux combination of both. Then, the light curves were fitted with a transit model including a second order polynomial over time and the transit parameters fixed to their literature values of Gibson et al. (2013b). We decided for one of the three light curve versions according to the lowest scatter in the residuals. For HAT-P-12, the fainter comparison star was of low photometric quality, the best quality was always achieved with the brighter comparison star alone. For HAT-P-32,

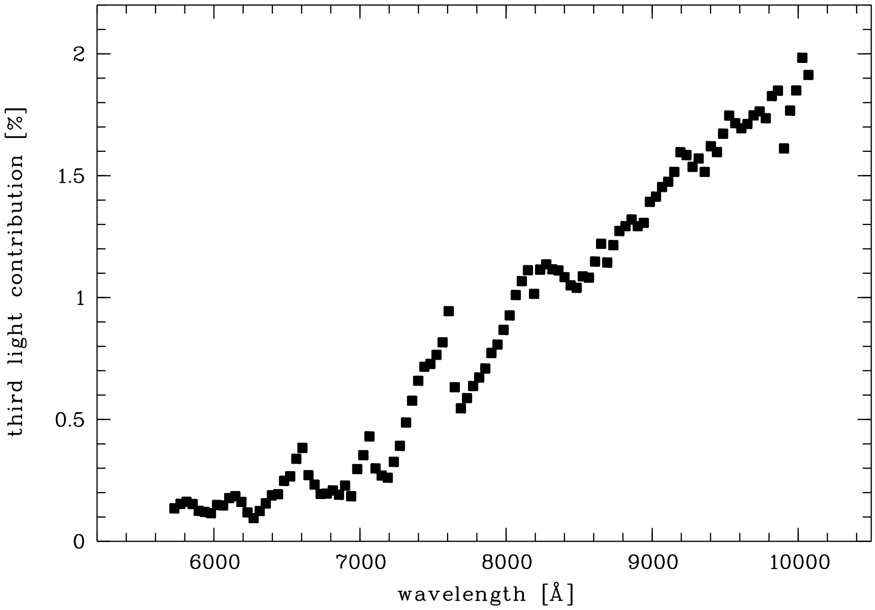

Fig. 5.7. Third light contribution of the M dwarf near-by star to the integrated light of HAT-P-32. Prominent molecular absorption bands of the M dwarf spectrum are visible.

the choice varied and is listed in Table 5.2.

The second step of the transit analysis consisted of the choice of the detrending function. As done in Section 3.3.1 for HAT-P-19 and in Section 4.6.1 for HAT-P-12, we tested if a decorrelation with external parameters like time, airmass, FWHM, detector position or rotation angle could significantly decrease the rms of the light curves. The best results were obtained with a correlation over time. We used the Bayesian Information Criterion, Equation 3.2, to decide for the most appropriate order of a low-order detrending polynomial with time as independent parameter. For the majority of the partial HAT-P-12b light curves, a linear function was sufficient. In case of the HAT-P-32 light curves, detrending polynomials of order one to three were used. The orders of the applied detrending functions are listed in Table 5.1 for HAT-P-12b and Table 5.2 for HAT-P-32b.

The transit modeling was executed with JKTEBOP as in the previous analyses of HAT-P-19b and HAT-P-12b. After an initial transit fit, we applied a 3 sigma clipping to remove significant outliers. Following, the photometric errors were increased by a common factor to yield a χ^2_{red} of unity. We calculated the β factor with Equation 2.12 as described in Section 2.2 and inflated the photometric errors further by this factor to account for correlated noise in the light curves. Unfortunately, we noticed a substantial, but varying amount of correlated noise in the HAT-P-32 light curves at the 1 to 3 mmag level. Correspondingly, the β factors for HAT-P-32 are larger than for HAT-P-12 or HAT-P-19 in Section 3.3.

For the HAT-P-12b MODS light curves, the free fit parameters were the fractional planetary radius r_p, the vertical offset c_0 and the coefficients of the detrending polynomial c_1 and c_2 depending on the order of the function. The inclination i and the fractional stellar radius $r_\star$ were fixed to the values of Table 4.3, the transit midtime T_0 was fixed to the ephemeris of Equation 4.1. In contrast to our treatment of the coefficients of the quadratic limb darkening law in previous chapters, we did not fit for the linear coefficient u because it is not well constrained by the incomplete transit light curves. Our experience of Section 4.6 showed that the measurements generally agreed with the calculated LDC, therefore both u and v were fixed to theoretical values. We obtained these calculated LDC from Antonio Claret in high spectral resolution (Claret et al. 2012) and formed an average over the 100 Å wavelength channels used for the spectrophotometry, weighted with the spectral flux from our mean spectrum. Both LDC u and v were perturbed during the error estimation in an interval of 0.1 to account for potential systematic uncertainties of the theoretical LDC. The transit parameter uncertainties were estimated with a Monte Carlo simulation of 3000 steps and a residual-permutation algorithm as explained in detail in Section 2.2. The higher value of both methods was adopted as the final $1\,\sigma$ uncertainty given in Table 5.1.

The free parameters in case of the HAT-P-32b light curves were r_p, c_0, c_1 and if used c_2 and c_3, and the linear LDC u. The values for i and $r_\star$ were taken from Gibson et al. (2013b), T_0 was calculated according to the ephemeris given by Seeliger et al. (2014). Theoretical values for v in high spectral resolution were again supplied by Antonio Claret based on the calculation presented in Claret et al. (2013b).

5.7 Discussion

5.7.1 Transmission spectrum of HAT-P-12b

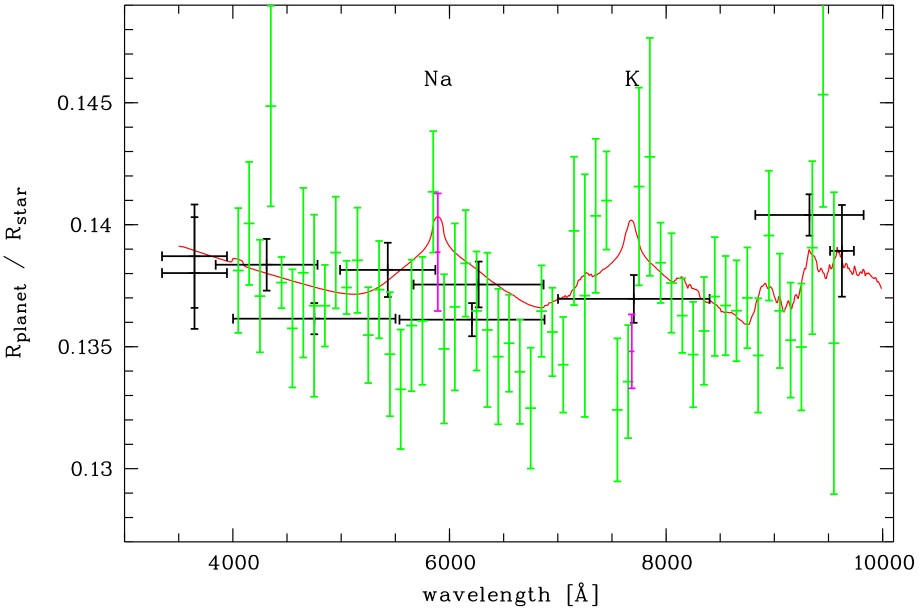

Fig. 5.8. Transmission spectrum of HAT-P-12b derived from the MODS transit measurement. In green the derived k values per 100 Å wide wavelength channel are shown. The k measurements in 50 Å wide channels centered on the sodium and potassium features are overplotted in magenta. For comparison the broad-band values derived in Chapter 4 are presented in black together with the cloud-free atmosphere model from Fortney et al. (2010) as red solid line. The vertical bars denote the $1\,\sigma$ uncertainties, the horizontal bars mark the wavelength width of the spectral channels and broad-band filters.

The derived transmission spectrum of the partial MODS transit in combination with the broad-band data points from Chapter 4 are presented in Figure 5.8. We computed the χ^2 value for the 100 Å data points in relation to a solar-composition, cloud-free atmosphere model computed by Jonathan Fortney for the planetary parameters of HAT-P-12b, and a flat line. For the Fortney model we found $\chi^2 = 46.4$ and for the flat model $\chi^2 = 48.5$. Hence, with the degrees of freedom equaling the number of data points minus one, 56 - 1, both models yield a $\chi^2_{\rm red}$ of below unity. We can conclude that the accuracy of the partial transit observation is not sufficient to constrain the models of HAT-P-12b's atmosphere. The disagreement between the measurement in the 50 Å wavelength channel centered at the potassium line with the cloud-free model by about $2.5\,\sigma$ should not be over-interpreted, since the scatter of the 100 Å measurements to both sides of the potassium feature is rather large.

The derived error bars confirm our experience gained in Section 4.6.2 that a need for a detrending function adds significant uncertainty in the fit of a partial transit. The three transits for which the BIC value suggested no detrending (100 Å at 4450 and 5050 Å as well as the 50 Å channel centered at K) have error bars about half in size than the detrended light curves.

5.7.2 Transmission spectrum of HAT-P-32b

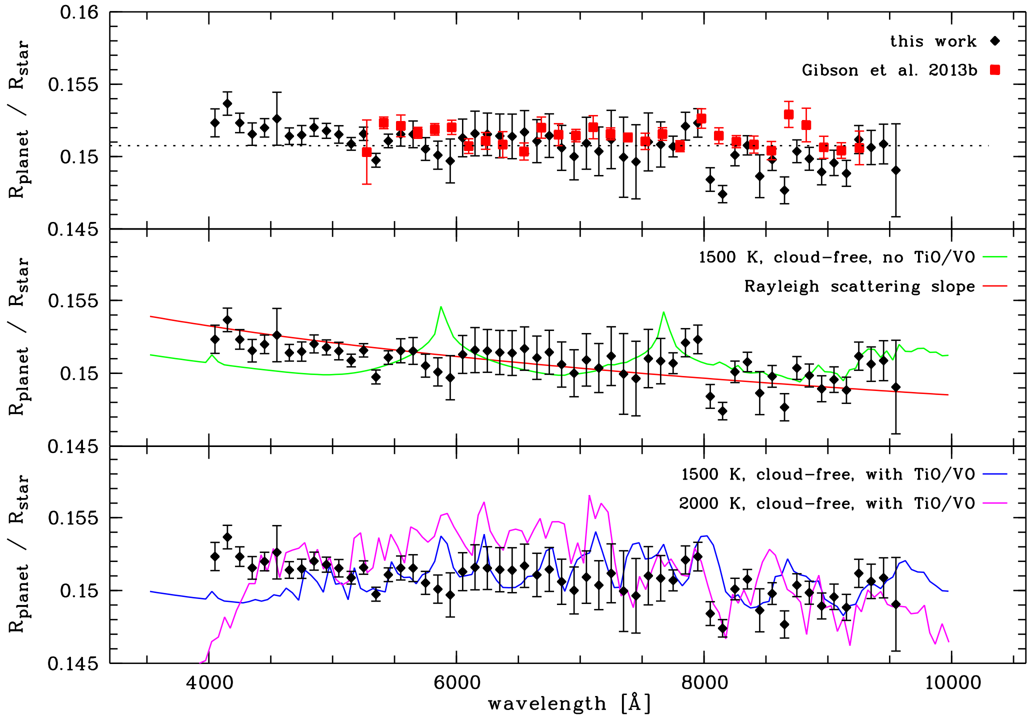

Fig. 5.9. Transmission spectrum of HAT-P-32b derived from the MODS transit measurement. Upper panel: The transmission spectrum of this work (black) is compared to the derived spectrum of Gibson et al. (2013b). Middle panel: The spectrum is overplotted with a cloud-free solar-composition model of T = 1500 K without TiO/VO (Fortney et al. 2010) and a model presenting a Rayleigh slope scaled by the estimated scale height of HAT-P-32b. Lower panel: The spectrum is overplotted with a cloud-free model of T = 1500 K and a cloud-free model of T = 2000 K. Both include the absorption of TiO and VO at solar composition. Note that HAT-P-32b has an equilibrium temperature of about 1800 K.

Figure 5.9 shows our resulting transmission spectrum of the MODS transit observation in comparison to the spectrum derived by Gibson et al. (2013b), models from Fortney et al. (2010) and a Rayleigh-scattering slope of $dR_p/d\ln\lambda = -4H$ similar to the observed spectrum of HD189733b (Lecavelier Des Etangs et al. 2008a). The estimated scale height H of HAT-P-32b is about 1100 km. The isothermal model atmospheres calculated by Fortney et al. (2010) provide temperatures of 1500 and 2000 K, surrounding the estimated equilibrium temperature of HAT-P-32b of ~ 1800 K. Furthermore, the models assumed solar-composition including TiO and VO, in another version TiO/VO are removed.

We refrain from a quantitative comparison of the derived transmission spectrum with the models because of two uncertainties whose analyses are not yet finally completed: The measurements of the planet-star radius ratio k show a dependence on the choice of the order of the detrending function and on the comparison star. If we detrend the entire data set from 4000 to 9600 Å homogeneously with a first order polynomial, individual data points change by up to $2\,\sigma$. In relation to the uncertainty, the change is less if we use a third order polynomial for all light curves, but since the higher number of free parameters increase the error bars on k, an exclusion of possible atmosphere models is more difficult. Light curves in the range of 5900 to 7400 Å show correlated noise features of up to 5 mmag, making a higher order of detrending necessary. However, the noise features look very similar for all these light curves, which might be the reason why the scatter of k among these light curves is smaller than their mean error bars. It is work in progress to test if a correction for "common mode residuals" can clean these light curves better than our current detrending technique. Such approach can be found in the literature for example in Sing et al. (2012), Gibson et al. (2013a) and Gibson et al. (2013b). However, in Section 3.4.2 we made the experience that a detrending not individual to each light curve channel, but with the detrending function linked among adjacent channels can produce features in the transmission spectrum that have not been found otherwise. Hence, exhaustive tests need to be performed before we can claim a final result.

The dependence of the transmission spectrum on the choice of the comparison stars is also related to correlated noise. We found that the different reference stars show very different noise features in the same wavelength channels. The current analysis includes only the two brightest of the four observed stars, and according to a test which comparison star (or their flux combination) delivers the least scatter in the light curves, they are used or discarded. In the near future, we plan to use all four comparison stars throughout the wavelength channels and combine them in a weighted average. The scatter in the light curves should be applied as the inverse weighting factor. This technique is similar to the creation of an artificial reference star as described in Broeg et al. (2005). The scatter is a better indicator of the quality of the light curve than the flux rate, since it also includes correlated noise features. Furthermore, we expect that the amount of correlated noise contributed to the differential light curves by the reference stars decreases because it averages out to some extent.

A comparison of the current transmission spectrum with the one of Gibson et al. (2013b) shows broad consistency, see the upper panel of Figure 5.9. We notice that the measurements of Gibson et al. (2013b) are in average higher by about 0.0006 than the average of this work. The offset can be explained by a systematic difference in the LDC of the quadratic limb darkening law used in both analyses. Gibson et al. (2013b) derived their LDC from the transit fit and found values for the quadratic coefficient v systematically larger by ~ 0.1 than the theoretical values used here.

The most robust result of the MODS transmission spectroscopy of HAT-P-32b is the exclusion of significant absorption by TiO and VO in the planetary atmosphere. Both models including TiO/VO of 1500 and 2000 K predict a higher planet-star radius ratio in the mid optical region than at the blue end. Since our blue light curves from 4000 to 5500 Å show the least rms values and least correlated noise, we can significantly rule out a smaller transit depth independent of the choice of comparison stars and detrending polynomials. The current set of achieved results also disfavors wide absorption features of sodium and potassium, confirming the result of Gibson et al. (2013b) of a featureless spectrum at the corresponding wavelengths. However, the slight rise in the radius ratio at the blue end of the spectrum can be interpreted as Rayleigh scattering in the atmosphere.

It could either be caused by a haze layer, which would explain the lack of prominent alkali metal absorption, or by hydrogen molecules in a clear atmosphere. The lack of sodium and potassium absorption in a clear atmosphere could result from photo-ionization or from depletion of Na and K at the terminator by condensation of for example Na_2S on the colder night-side of the planet.

In summary, we find no absorption feature by Na, K or TiO/VO in the transmission spectrum of HAT-P-32, ruling out either a solar-abundance of these chemical species or a clear, cloud-free atmosphere. Towards the blue end of the spectrum we see an upward trend in the planet-star radius ratio, explainable by Rayleigh scattering by either a haze layer of condensates or hydrogen molecules. Further tests on the robustness of our results are work in progress.

Table 5.1.: Characteristics of the extracted transit light curves of HAT-P-12b.

Wavelength (Å)	N_{data}	rms (mmag)	β	order polynomial	u theor.	v theor.	$k = r_p/r_\star$
4000 - 4100	72	1.47	1.20	1	0.9733	-0.1406	0.1381 ± 0.0025
4100 - 4200	72	1.40	1.00	1	0.9974	-0.1824	0.1400 ± 0.0025
4200 - 4300	73	1.36	1.00	1	0.8862	-0.1113	0.1370 ± 0.0023
4300 - 4400	57	2.03	1.35	1	0.8267	-0.0301	0.1448 ± 0.0041
4400 - 4500	73	1.10	1.00	0	0.8867	-0.0660	0.1376 ± 0.0010
4500 - 4600	72	0.94	1.00	2	0.9198	-0.0617	0.1357 ± 0.0024
4600 - 4700	71	1.90	1.00	1	0.8966	-0.0383	0.1380 ± 0.0034
4700 - 4800	57	1.88	1.00	1	0.9448	-0.0884	0.1366 ± 0.0037
4800 - 4900	70	0.93	1.00	1	0.8412	-0.0106	0.1366 ± 0.0016
4900 - 5000	71	0.86	1.21	2	0.8514	-0.0360	0.1388 ± 0.0022
5000 - 5100	73	1.23	1.12	0	0.8222	-0.0642	0.1374 ± 0.0010
5100 - 5200	71	1.20	1.11	1	0.7191	-0.0215	0.1385 ± 0.0021
5200 - 5300	73	1.09	1.00	1	0.7528	0.0198	0.1354 ± 0.0019
5300 - 5400	71	1.08	1.00	1	0.7420	0.0386	0.1373 ± 0.0019
5400 - 5500	73	1.20	1.47	1	0.7258	0.0472	0.1346 ± 0.0025
5500 - 5600	72	1.30	1.00	1	0.7273	0.0544	0.1332 ± 0.0024
5600 - 5700	78	1.34	1.17	1	0.7103	0.0736	0.1358 ± 0.0026
5700 - 5800	76	1.15	1.64	1	0.7086	0.0732	0.1360 ± 0.0026
5800 - 5900	77	0.99	1.12	2	0.6800	0.0805	0.1413 ± 0.0024
5900 - 6000	77	1.34	1.50	1	0.6790	0.0904	0.1349 ± 0.0030
6000 - 6100	77	1.33	1.71	1	0.6640	0.0983	0.1366 ± 0.0034
6100 - 6200	70	1.23	1.39	1	0.6354	0.1007	0.1384 ± 0.0021
6200 - 6300	71	1.18	1.57	1	0.6282	0.1048	0.1364 ± 0.0024
6300 - 6400	78	1.34	1.72	1	0.6194	0.1095	0.1356 ± 0.0031
6400 - 6500	76	1.19	1.59	1	0.6032	0.1122	0.1345 ± 0.0027
6500 - 6600	70	1.10	1.47	1	0.5810	0.1340	0.1351 ± 0.0019
6600 - 6700	77	1.08	1.48	1	0.5896	0.1256	0.1339 ± 0.0021
6700 - 6800	78	1.20	1.42	1	0.5780	0.1277	0.1324 ± 0.0024
6800 - 6900	77	1.01	1.15	1	0.5788	0.1225	0.1364 ± 0.0018
6900 - 7000	77	1.01	1.31	1	0.5706	0.1226	0.1356 ± 0.0018
7000 - 7100	77	1.06	1.43	1	0.5501	0.1332	0.1342 ± 0.0019
7100 - 7200	63	1.48	1.00	1	0.5318	0.1390	0.1397 ± 0.0030
7200 - 7300	64	2.43	1.00	1	0.5277	0.1416	0.1370 ± 0.0049
7300 - 7400	78	1.32	1.58	1	0.5174	0.1415	0.1403 ± 0.0031
7400 - 7500	77	1.14	1.40	1	0.5070	0.1454	0.1409 ± 0.0020
7500 - 7600	75	1.14	1.22	2	0.5015	0.1494	0.1324 ± 0.0029
7600 - 7700	78	1.34	1.00	1	0.4922	0.1515	0.1335 ± 0.0023
7700 - 7800	65	2.24	1.00	1	0.4813	0.1560	0.1415 ± 0.0040
7800 - 7900	59	2.39	1.00	1	0.4823	0.1543	0.1427 ± 0.0048
7900 - 8000	78	0.95	1.01	1	0.4688	0.1556	0.1384 ± 0.0016
8000 - 8100	77	1.13	1.03	1	0.4665	0.1526	0.1376 ± 0.0020
8100 - 8200	78	0.87	1.10	1	0.4599	0.1535	0.1362 ± 0.0015
8200 - 8300	78	1.19	1.06	1	0.4499	0.1579	0.1346 ± 0.0021
8300 - 8400	78	1.24	1.00	1	0.4429	0.1568	0.1356 ± 0.0022
8400 - 8500	77	1.14	1.19	1	0.4411	0.1605	0.1370 ± 0.0024
8500 - 8600	78	1.19	1.00	1	0.4145	0.1660	0.1366 ± 0.0020
8600 - 8700	78	1.20	1.00	1	0.4129	0.1656	0.1364 ± 0.0020
8700 - 8800	75	1.17	1.00	1	0.4207	0.1648	0.1370 ± 0.0020
8800 - 8900	76	1.26	1.00	1	0.4105	0.1664	0.1346 ± 0.0023
8900 - 9000	78	1.55	1.00	1	0.4142	0.1675	0.1395 ± 0.0026
9000 - 9100	76	1.33	1.00	1	0.4016	0.1709	0.1364 ± 0.0023
9100 - 9200	77	1.33	1.00	1	0.4097	0.1632	0.1352 ± 0.0023
9200 - 9300	75	1.47	1.00	1	0.3961	0.1654	0.1349 ± 0.0026

Table 5.1.: continued

Wavelength	N_{data}	rms	β	polynomial	u	v	$k = r_p/r_\star$
9300 - 9400	76	2.02	1.00	1	0.3971	0.1638	0.1390 ± 0.0035
9400 - 9500	76	2.72	1.09	1	0.3892	0.1637	0.1453 ± 0.0046
9500 - 9600	78	2.46	1.00	2	0.3882	0.1675	0.1351 ± 0.0061
5867 - 5917	78	1.46	1.37	1	0.6713	0.0666	0.1388 ± 0.0024
7658 - 7708	78	1.62	1.00	0	0.4841	0.1537	0.1348 ± 0.0015

Table 5.2.: Characteristics of the extracted transit light curves of HAT-P-32b.

Wavelength (Å)	N_{data}	rms (mmag)	β	comp. star	order polynomial	u fitted	v theor.	$k = r_p/r_\star$
4000 - 4100	236	1.69	1.17	1,2	1	0.570	0.135	0.15233 ± 0.00096
4100 - 4200	237	1.46	1.14	1,2	1	0.518	0.194	0.15366 ± 0.00080
4200 - 4300	234	1.35	1.04	1,2	1	0.597	0.129	0.15232 ± 0.00067
4300 - 4400	237	1.36	1.19	1	1	0.552	0.117	0.15155 ± 0.00077
4400 - 4500	237	1.10	1.18	1,2	1	0.503	0.193	0.15198 ± 0.00063
4500 - 4600	159	3.30	1.00	1,2	1	0.549	0.159	0.15261 ± 0.00183
4600 - 4700	237	0.91	1.30	1,2	1	0.481	0.227	0.15140 ± 0.00056
4700 - 4800	238	0.93	1.42	1,2	1	0.460	0.231	0.15148 ± 0.00065
4800 - 4900	236	1.00	1.24	1,2	1	0.391	0.251	0.15201 ± 0.00061
4900 - 5000	235	0.85	1.22	1,2	1	0.429	0.224	0.15177 ± 0.00051
5000 - 5100	237	0.94	1.32	1,2	1	0.432	0.223	0.15152 ± 0.00060
5100 - 5200	234	0.91	1.00	1,2	1	0.416	0.214	0.15087 ± 0.00043
5200 - 5300	237	0.82	1.11	1,2	1	0.402	0.225	0.15157 ± 0.00045
5300 - 5400	238	0.79	1.26	1,2	1	0.415	0.228	0.14974 ± 0.00047
5400 - 5500	237	0.85	1.08	1,2	1	0.371	0.231	0.15108 ± 0.00046
5500 - 5600	236	0.96	1.73	1,2	1	0.366	0.236	0.15154 ± 0.00082
5600 - 5700	237	1.23	1.57	1	1	0.268	0.231	0.15153 ± 0.00092
5700 - 5800	239	1.17	1.38	1	1	0.256	0.236	0.15052 ± 0.00078
5800 - 5900	239	1.24	1.55	1	1	0.267	0.238	0.15009 ± 0.00096
5900 - 6000	239	1.09	1.41	1	3	0.266	0.243	0.14969 ± 0.00151
6000 - 6100	239	0.95	1.32	1	3	0.240	0.242	0.15129 ± 0.00130
6100 - 6200	239	0.98	1.52	1	3	0.263	0.233	0.15159 ± 0.00154
6200 - 6300	239	0.99	1.42	1	3	0.260	0.225	0.15154 ± 0.00146
6300 - 6400	239	1.02	1.42	1	3	0.235	0.237	0.15142 ± 0.00151
6400 - 6500	238	0.98	1.43	1	3	0.232	0.234	0.15139 ± 0.00154
6500 - 6600	239	1.09	1.28	1	3	0.177	0.251	0.15169 ± 0.00148
6600 - 6700	239	1.00	1.42	1	3	0.210	0.235	0.15106 ± 0.00148
6700 - 6800	239	1.03	1.41	1	3	0.206	0.229	0.15144 ± 0.00150
6800 - 6900	238	1.06	1.42	1	3	0.229	0.230	0.15060 ± 0.00155
6900 - 7000	239	1.13	1.42	1	3	0.223	0.233	0.15000 ± 0.00161
7000 - 7100	238	1.09	1.57	1	3	0.243	0.224	0.15091 ± 0.00179
7100 - 7200	240	1.10	1.49	1,2	3	0.241	0.222	0.15036 ± 0.00168
7200 - 7300	237	1.21	1.60	1,2	3	0.278	0.228	0.15118 ± 0.00201
7300 - 7400	236	1.57	1.74	1,2	3	0.317	0.220	0.14995 ± 0.00277
7400 - 7500	200	1.98	1.14	2	3	0.156	0.225	0.14963 ± 0.00255
7500 - 7600	196	1.75	1.00	2	3	0.193	0.223	0.15101 ± 0.00200
7600 - 7700	236	1.53	1.00	2	3	0.231	0.222	0.15083 ± 0.00156
7700 - 7800	231	1.28	1.10	2	1	0.235	0.225	0.15069 ± 0.00071
7800 - 7900	198	1.82	1.00	2	1	0.248	0.221	0.15210 ± 0.00096
7900 - 8000	201	1.57	1.16	2	1	0.201	0.221	0.15232 ± 0.00098

Table 5.2.: continued

Wavelength	N_{data}	rms	β	comp.	polynomial	u	v	$k = r_p/r_\star$
8000 - 8100	238	1.06	1.51	1,2	1	0.252	0.222	0.14841 ± 0.00081
8100 - 8200	235	0.85	1.37	1,2	1	0.153	0.223	0.14740 ± 0.00059
8200 - 8300	237	1.51	1.05	2	1	0.220	0.216	0.15010 ± 0.00073
8300 - 8400	238	1.43	1.00	2	1	0.163	0.218	0.15077 ± 0.00066
8400 - 8500	236	1.43	1.03	2	2	0.183	0.217	0.14864 ± 0.00147
8500 - 8600	236	1.52	1.00	2	1	0.119	0.211	0.14979 ± 0.00074
8600 - 8700	238	1.55	1.20	2	1	0.162	0.214	0.14766 ± 0.00092
8700 - 8800	238	1.68	1.00	2	1	0.126	0.220	0.15036 ± 0.00078
8800 - 8900	237	1.75	1.00	2	1	0.120	0.222	0.14984 ± 0.00079
8900 - 9000	237	1.81	1.04	2	1	0.181	0.213	0.14893 ± 0.00088
9000 - 9100	236	1.70	1.03	2	1	0.162	0.216	0.14956 ± 0.00087
9100 - 9200	237	1.82	1.00	2	1	0.134	0.214	0.14883 ± 0.00089
9200 - 9300	234	2.01	1.00	2	1	0.176	0.220	0.15117 ± 0.00096
9300 - 9400	238	2.57	1.00	2	1	0.155	0.208	0.15062 ± 0.00117
9400 - 9500	233	2.84	1.00	2	1	0.117	0.211	0.15086 ± 0.00137
9500 - 9600	232	2.90	1.09	2	2	0.161	0.228	0.14905 ± 0.00321

6 Conclusions and Outlook

In this work, we presented spectrophotometric transit observations of three inflated Hot Jupiter exoplanets. The scientific motivation was the extension of the sample of Hot Jupiters probed by transmission spectroscopy to advance the comparative exoplanetology. When we started with the work for this thesis in the year 2010, there existed optical transmission measurements for two Hot Jupiter systems, HD189733b and HD209458b. To date, the number of investigated targets rose to about 15. Thus, the sample is now large enough to draw first conclusions whether certain features in transmission spectra of exoplanets are common. Scientists get a first glimpse on how well current theoretical models can explain the measurements and vice versa, how well these measurements can constrain the models. Observers begin to learn if these exoplanets actually reveal some of their atmospheric information or if the majority of them prefers to hide behind clouds.

At about the time of the very first successful attempts of optical transmission spectroscopy, Fortney (2005) predicted that for the majority of exoplanets it might be difficult to characterize atmospheric compositions at the terminator region with this observing technique. Due to the slant viewing angle, the optical path through the exoplanet atmosphere is very long, strongly enhancing the opacity of condensates even at very low concentrations. The atmosphere becomes opaque at wavelengths for which it is transparent at a radial viewing angle. The first years of observational experience seem to confirm this prediction. The detection of pressure-broadened features originating in deeper layers of the atmospheres are the exception, instead rather featureless spectra seem to be the rule.

Here, we extended the sample of targeted Hot Jupiter atmospheres by two objects, HAT-P-19b and HAT-P-12b, and performed an independent measurement of a third one, HAT-P-32b, for which already a transmission study existed. For HAT-P-19b, our achieved accuracy is not sufficient to significantly rule out a pressure-broadened sodium absorption. However, a flat transmission spectrum from 5500 to 7600 Å is favored by the measurement (Chapter 3). No statement could be made about Rayleigh scattering in the atmosphere. For HAT-P-12b, a Rayleigh-slope similar to the textbook-example of HD189733b extending over the entire optical wavelength range could significantly be ruled out by our measurements (Chapter 4). The broad-band transit light curves lack the spectral resolution to search for absorption features of sodium and potassium as predicted by the theory. We tried to target these features with spectroscopic transit observations with MODS, but due to bad weather we only collected data of a partial transit which does not provide sufficient sensitivity to detect/rule out the predicted spectral features (Chapter 5). The spectroscopic transit observation of HAT-P-32 allowed the exclusion of solar-composition models that predict features of Na, K and TiO/VO. The observation favors a featureless spectrum or a flat spectrum with a Rayleigh-slope towards shorter wavelengths (Chapter 5). While the analysis of HAT-P-19b and HAT-P-12b is completed, additional tests on the robustness of the results of HAT-P-32b against details of the analysis are work in progress.

The measurement of the spectrum of HAT-P-19b, our data on HAT-P-12b in combination with NIR measurements of Line et al. (2013) and our current result on HAT-P-32b all favor a flat spectrum. The achieved sensitivities are not sufficient to allow for an unambiguous interpretation. The lack of theoretically predicted absorption features of sodium and potassium could also be explained by a depletion of atomic neutral Na and K by photoionization from high-energy flux of the near-by host stars. A scenario in which wind transported the elements from the day-night terminator to the cooler night-side is also possible, where the alkali metals were bound in condensates. Another possibility for the hotter HAT-P-32b is that the alkalis and TiO/VO are present in such (non-solar) abundances that the TiO/VO absorption is too weak to form a measurable slope of higher absorption towards the longer wavelengths, but strong enough to blend and dilute the otherwise prominent wings of Na and K absorption. Furthermore, our temperature estimations could potentially be wrong because we have no direct temperature measurement from the terminator region probed by our data. If the real temperature is much cooler than assumed, the scale height of an atmosphere and the strength of the Na and K features would be lower than in the models used in this work. For all the three objects a different combination of these explanation might resemble the truth. But maybe the easiest explanation, most straight forward to apply to all three objects, is the suggestion of Fortney (2005) that the atmospheres are not clear. Hazes or clouds formed by condensates of trace species could make them opaque. The high ratio of featureless spectra versus spectra showing broad features, independent of temperature and derived in this work as well as comparable studies, favor this simple explanation. If true, this conclusion would mean that for many exoplanets, probably for their majority, the capability of transmission spectroscopy to determine the atmospheric composition of an exoplanet is limited. In case of clouds/hazes, observations like the ones presented here would not reveal any atmospheric information. Only transmission spectroscopy at much higher spectral resolution ($\mathrm{R} > 20\,000$) could detect spectral signatures.

Additional achievements of this work were the refinement of the transit parameters and ephemeris of HAT-P-19b and HAT-P-12b. Furthermore, we monitored all our targets photometrically to be able to correct our transmission spectra for the influence of unocculted starspots. We found HAT-P-19b to be variable periodically at a level of below 1%. The derived period was interpreted as the so far unknown stellar rotation period, which gave us the chance for a refinement of the age estimate via gyrochronology. For HAT-P-12b and HAT-P-32b, we did not detect periodic variability down to photometric amplitudes of about 2 and 1 mmag, respectively. While for other objects like HD189733b, WASP-19b and GJ1214b, similar studies expressed the need for a starspot correction, our monitoring results proved a correction to be irrelevant for our transit measurements. However, the transit depth of HAT-P-32b had to be corrected for a third light contribution of a near-by M star, which we performed in detail.

One of the main experiences we could draw from our work was the difficulty to significantly constrain the atmospheric models with ground-based measurements even for very favorable targets. The demanded accuracy is well at the limit that can be reached with the biggest telescopes on Earth. The main issue is not photon noise, but correlated noise of often unknown origin. Mostly, it is not intrinsic to the astronomical source, but is caused either by the Earth atmosphere or by the instrument and affects the transit light curves at a level from 0.5 up to 5 mmag. In the majority, it is not repeatable by subsequent measurements and therefore hard to understand and difficult to model. Because the targeted variations in transit depth over wavelength account to $10^{-4} - 10^{-3}$, uncorrected correlated noise at the mmag level can change the derived results significantly. Error estimation algorithms try to account for this in various ways, but our experience of Chapter 4 showed the uncertainties to be underestimated for single transit measurements. We suggest to take advantage of the circumstance that for ground-based observations the correlated noise features are not repeatable. At first, these features average out in the analysis of observations from multiple epochs. At second, the analysis of multiple measurements of the same event (either taken at the same or multiple epochs) allows for more realistic error estimations because differences caused by different correlated noise are better revealed. Together, this gives much more robust results.

For a robust result, we need multiple measurements at the same wavelength and spectral resolution, and to constrain the atmospheric models, we need measurements at different wavelength and different resolution. Therefore, since observing time and manpower are limited, in the future we will rather concentrate on single objects than to extend this kind of measurement to many other objects. We will continue to use small- and medium-sized telescopes for observations at selected broad-band filters because access to these telescopes is comparably easy. Furthermore, their data can be very meaningful especially in combination with transit observations of low-resolution spectroscopy. For example, the indication of an increased transit depth at very blue wavelength regions of HAT-P-32b could be confirmed by 1m-class telescopes in the Johnson B band and 4m-class telescopes in the Johnson U band. Such observations would significantly strengthen the argumentation of Rayleigh scattering in the atmosphere. Indeed, this analysis is work in progress as part of a diploma thesis designed and assisted by the author of this work using observations of the STELLA telescope and the Nordic Optical Telescope. Furthermore, if robust results of transmission spectroscopy at 50 or 100 Å resolution exist, any physical interpretation would greatly benefit from complementary transit measurements at high-spectral resolution. Such measurements are sensitive to the line cores of for example sodium and allow for an atmospheric characterization by the line profile next to the pure line detection. Several successful attempts have proven that these goals can be achieved during a single transit event over a length of about 6 hours telescope time (Snellen et al. 2008; Wood et al. 2011; Zhou & Bayliss 2012). One instrument to perform such observations for our northern targets would be the new PEPSI spectrograph at the LBT built by the AIP (Strassmeier et al. 2008).

We also plan an exhaustive search for unpublished transit observations in publically available archives of ground-based telescopes. Derived from own experience and private communication with many colleagues, there were many more transit observations executed in recent years than appeared in publications. One reason might be that the achieved accuracy is not sufficient for a publication. If such data sets could be combined with others, the combination should reach a higher signal-to-noise and is more sensitive to correlated noise because of multiple independent measurements. The chance of finding multiple data set for a single object in the archives is rather high, since the target selection mostly follows the same criteria. Therefore, all the transmission spectroscopy attempts currently underway concentrate on 12 to 15 objects among more than thousand known transiting planets. With our data reduction tools for photometry and multi-object spectroscopy on hand, we hope to identify promising data sets in a limited amount of time.

Another approach very helpful for the community would be to verify to which extent results depend on details of the analysis. In Section 4.4 we partly found very different error bars when we re-analyzed published data sets. In Section 3.4.2 we learned how much the results can differ if details in the data analysis vary. A re-analysis of published data sets by independent groups could bring the firm insight that the results established so far in the atmospheric characterization of exoplanets are robust against the analysis techniques.

We want to conclude with a citation of Adam Burrows that reflects our gained experience very well (Burrows 2013): “I suggest that the true function of the recent past of exoplanet atmospheric research has been not to constrain planet properties for all time, but to train a new generation of scientists that, by rapid trial and error, is fast establishing a solid future foundation for a robust science of exoplanets.”

Bibliography

Adams, E. R., Dupree, A. K., Kulesa, C., & McCarthy, D. 2013, AJ, 146, 9

Agol, E., Steffen, J., Sari, R., & Clarkson, W. 2005, MNRAS, 359, 567

Aigrain, S., Pont, F., & Zucker, S. 2012, MNRAS, 419, 3147

Albrecht, S., Winn, J. N., Johnson, J. A., et al. 2012, ApJ, 757, 18

Alonso, R., Brown, T. M., Torres, G., et al. 2004, ApJ, 613, L153

Anderson, D. R., Smith, A. M. S., Lanotte, A. A., et al. 2011, MNRAS, 416, 2108

Aumann, H. H. 1984, in Bulletin of the American Astronomical Society, Vol. 16, Bulletin of the American Astronomical Society, 483

Aumann, H. H., Beichman, C. A., Gillett, F. C., et al. 1984, ApJ, 278, L23

Backman, D., Marengo, M., Stapelfeldt, K., et al. 2009, ApJ, 690, 1522

Bakos, G. Á., Noyes, R. W., Kovács, G., et al. 2007a, ApJ, 656, 552

Bakos, G. Á., Noyes, R. W., Kovács, G., et al. 2007b, ApJ, 656, 552

Bakos, G. Á., Torres, G., Pál, A., et al. 2010, ApJ, 710, 1724

Barclay, T., Rowe, J. F., Lissauer, J. J., et al. 2013, Nature, 494, 452

Barman, T. 2007, ApJ, 661, L191

Barman, T. S., Macintosh, B., Konopacky, Q. M., & Marois, C. 2011, ApJ, 733, 65

Barnes, S. A. 2010, ApJ, 722, 222

Barros, S. C. C., Boué, G., Gibson, N. P., et al. 2013, MNRAS, 430, 3032

Baskin, N. J., Knutson, H. A., Burrows, A., et al. 2013, ApJ, 773, 124

Batalha, N. M., Rowe, J. F., Bryson, S. T., et al. 2013, ApJS, 204, 24

Bean, J. L., Désert, J.-M., Kabath, P., et al. 2011, ApJ, 743, 92

Bean, J. L., Miller-Ricci Kempton, E., & Homeier, D. 2010, Nature, 468, 669

Belorizky, D. 1938, L'Astronomie, 52, 359

Benedict, G. F., McArthur, B. E., Gatewood, G., et al. 2006, AJ, 132, 2206

Bennett, D. P. & Rhie, S. H. 1996, ApJ, 472, 660

Bento, J., Wheatley, P. J., Copperwheat, C. M., et al. 2014, MNRAS, 437, 1511

Berdyugina, S. V. 2005, Living Reviews in Solar Physics, 2, 8

Berta, Z. K., Charbonneau, D., Bean, J., et al. 2011, ApJ, 736, 12

Berta, Z. K., Charbonneau, D., Désert, J.-M., et al. 2012, ApJ, 747, 35

Berta, Z. K., Irwin, J., & Charbonneau, D. 2013, ApJ, 775, 91

Bertin, E. & Arnouts, S. 1996, A&AS, 117, 393

Biddle, L. I., Pearson, K. A., Crossfield, I. J. M., et al. 2014, ArXiv e-prints

Biller, B. A., Crossfield, I. J. M., Mancini, L., et al. 2013a, ApJ, 778, L10

Biller, B. A., Liu, M. C., Wahhaj, Z., et al. 2013b, ApJ, 777, 160

Bond, I. A., Abe, F., Dodd, R. J., et al. 2001, MNRAS, 327, 868

Bonfils, X., Delfosse, X., Udry, S., et al. 2013, A&A, 549, A109

Bonfils, X., Gillon, M., Udry, S., et al. 2012, A&A, 546, A27

Borucki, W. J., Koch, D., Basri, G., et al. 2010, Science, 327, 977

Borucki, W. J., Koch, D. G., Basri, G., et al. 2011a, ApJ, 728, 117

Borucki, W. J., Koch, D. G., Basri, G., et al. 2011b, ApJ, 736, 19

Broeg, C., Fernández, M., & Neuhäuser, R. 2005, Astronomische Nachrichten, 326, 134

Broeg, C., Fortier, A., Ehrenreich, D., et al. 2013, in European Physical Journal Web of Conferences, Vol. 47, European Physical Journal Web of Conferences, 3005

Brown, T. M. 2001, ApJ, 553, 1006

Burke, C. J., Bryson, S. T., Mullally, F., et al. 2014, ApJS, 210, 19

Burrows, A. 2013, ArXiv e-prints

Burrows, A., Hubeny, I., Budaj, J., Knutson, H. A., & Charbonneau, D. 2007, ApJ, 668, L171

Burrows, A., Rauscher, E., Spiegel, D. S., & Menou, K. 2010, ApJ, 719, 341

Burrows, A., Sudarsky, D., & Hubeny, I. 2006, ApJ, 650, 1140

Campbell, B., Walker, G. A. H., & Yang, S. 1988, ApJ, 331, 902

Cassan, A., Kubas, D., Beaulieu, J.-P., et al. 2012, Nature, 481, 167

Charbonneau, D., Allen, L. E., Megeath, S. T., et al. 2005, ApJ, 626, 523

Charbonneau, D., Berta, Z. K., Irwin, J., et al. 2009, Nature, 462, 891

Charbonneau, D., Brown, T. M., Latham, D. W., & Mayor, M. 2000, ApJ, 529, L45

Charbonneau, D., Brown, T. M., Noyes, R. W., & Gilliland, R. L. 2002, ApJ, 568, 377

Charbonneau, D., Knutson, H. A., Barman, T., et al. 2008, ApJ, 686, 1341

Chauvin, G., Lagrange, A.-M., Dumas, C., et al. 2004, A&A, 425, L29

Chauvin, G., Thomson, M., Dumas, C., et al. 2003, A&A, 404, 157

Chen, G., van Boekel, R., Wang, H., et al. 2014, A&A, 563, A40

Choi, J., McCarthy, C., Marcy, G. W., et al. 2013, ApJ, 764, 131

Claret, A. 2000, A&A, 363, 1081

Claret, A. 2004, A&A, 428, 1001

Claret, A. 2009, A&A, 506, 1335

Claret, A., Diaz-Cordoves, J., & Gimenez, A. 1995, A&AS, 114, 247

Claret, A. & Hauschildt, P. H. 2003, A&A, 412, 241

Claret, A., Hauschildt, P. H., & Witte, S. 2012, A&A, 546, A14

Claret, A., Hauschildt, P. H., & Witte, S. 2013a, A&A, 552, A16

Claret, A., Hauschildt, P. H., & Witte, S. 2013b, A&A, 552, A16

Collier Cameron, A., Bouchy, F., Hébrard, G., et al. 2007, MNRAS, 375, 951

Colomé, J., Ribas, I., Fernández, D., et al. 2008, in Society of Photo-Optical Instrumentation Engineers (SPIE) Conference Series, Vol. 7019, Society of Photo-Optical Instrumentation Engineers (SPIE) Conference Series

Colón, K. D., Ford, E. B., Redfield, S., et al. 2012, MNRAS, 419, 2233

Copperwheat, C. M., Wheatley, P. J., Southworth, J., et al. 2013, MNRAS, 434, 661

Cowan, N. B. & Agol, E. 2011, ApJ, 729, 54

Croll, B., Albert, L., Jayawardhana, R., et al. 2011, ApJ, 736, 78

Cruz-Saenz de Miera, F., Chavez, M., Bertone, E., & Vega, O. 2014, MNRAS, 437, 391

Csizmadia, S., Pasternacki, T., Dreyer, C., et al. 2013, A&A, 549, A9

Czesla, S., Huber, K. F., Wolter, U., Schröter, S., & Schmitt, J. H. M. M. 2009, A&A, 505, 1277

de Mooij, E. J. W., Brogi, M., de Kok, R. J., et al. 2012, A&A, 538, A46

de Mooij, E. J. W., Brogi, M., de Kok, R. J., et al. 2013, ApJ, 771, 109

Deming, D., Harrington, J., Seager, S., & Richardson, L. J. 2006, ApJ, 644, 560

Deming, D., Seager, S., Richardson, L. J., & Harrington, J. 2005, Nature, 434, 740

Deming, D., Wilkins, A., McCullough, P., et al. 2013, ApJ, 774, 95

Demory, B.-O. & Seager, S. 2011, ApJS, 197, 12

Désert, J.-M., Sing, D., Vidal-Madjar, A., et al. 2011, A&A, 526, A12

Désert, J.-M., Vidal-Madjar, A., Lecavelier Des Etangs, A., et al. 2008, A&A, 492, 585

Dhillon, V. S., Marsh, T. R., Stevenson, M. J., et al. 2007, MNRAS, 378, 825

Diaz-Cordoves, J., Claret, A., & Gimenez, A. 1995, A&AS, 110, 329

Eastman, J., Gaudi, B. S., & Agol, E. 2013, PASP, 125, 83

Eastman, J., Siverd, R., & Gaudi, B. S. 2010, PASP, 122, 935

Ehrenreich, D., Bonfils, X., Lovis, C., et al. 2014, ArXiv e-prints

Ehrenreich, D. & Désert, J.-M. 2011, A&A, 529, A136

Eiroa, C., Marshall, J. P., Mora, A., et al. 2013, A&A, 555, A11

Esteves, L. J., De Mooij, E. J. W., & Jayawardhana, R. 2013, ApJ, 772, 51

Etzel, P. B. 1981, in Photometric and Spectroscopic Binary Systems, ed. E. B. Carling & Z. Kopal, 111

Fortney, J. J. 2005, MNRAS, 364, 649

Fortney, J. J., Lodders, K., Marley, M. S., & Freedman, R. S. 2008, ApJ, 678, 1419

Fortney, J. J., Shabram, M., Showman, A. P., et al. 2010, ApJ, 709, 1396

Fortney, J. J., Sudarsky, D., Hubeny, I., et al. 2003, ApJ, 589, 615

Fressin, F., Torres, G., Charbonneau, D., et al. 2013, ApJ, 766, 81

Fukui, A., Kawashima, Y., Ikoma, M., et al. 2014, ArXiv e-prints

Fukui, A., Narita, N., Kurosaki, K., et al. 2013, ApJ, 770, 95

Gatewood, G. & Eichhorn, H. 1973, AJ, 78, 769

Gazak, J. Z., Johnson, J. A., Tonry, J., et al. 2012, Advances in Astronomy, 2012

Giallongo, E., Ragazzoni, R., Grazian, A., et al. 2008, A&A, 482, 349

Gibson, N. P., Aigrain, S., Barstow, J. K., et al. 2013a, MNRAS, 428, 3680

Gibson, N. P., Aigrain, S., Barstow, J. K., et al. 2013b, ArXiv e-prints

Gibson, N. P., Aigrain, S., Pont, F., et al. 2012, MNRAS, 422, 753

Gibson, N. P., Pont, F., & Aigrain, S. 2011, MNRAS, 411, 2199

Gillon, M., Pont, F., Moutou, C., et al. 2006, A&A, 459, 249

Giménez, A. 2006, A&A, 450, 1231

Gondoin, P. 2008, A&A, 478, 883

Gould, A. & Loeb, A. 1992, ApJ, 396, 104

Gray, R. O. & Corbally, C. J. 1994, AJ, 107, 742

Hartman, J. D., Bakos, G. Á., Sato, B., et al. 2011a, ApJ, 726, 52

Hartman, J. D., Bakos, G. Á., Torres, G., et al. 2014, AJ, 147, 128

Hartman, J. D., Bakos, G. Á., Torres, G., et al. 2009, ApJ, 706, 785

Hartman, J. D., Bakos, G. Á., Torres, G., et al. 2011b, ApJ, 742, 59

Hatzes, A. P., Cochran, W. D., Endl, M., et al. 2003, ApJ, 599, 1383

Hayek, W., Sing, D., Pont, F., & Asplund, M. 2012, A&A, 539, A102

Heller, R. 2012, A&A, 545, L8

Heller, R. 2014, ApJ, 787, 14

Heller, R. & Barnes, R. 2013, Astrobiology, 13, 18

Hellier, C., Anderson, D. R., Collier Cameron, A., et al. 2010, ApJ, 723, L60

Helling, C., Woitke, P., & Thi, W.-F. 2008, A&A, 485, 547

Heng, K. & Demory, B.-O. 2013, ApJ, 777, 100

Heng, K., Hayek, W., Pont, F., & Sing, D. K. 2012, MNRAS, 420, 20

Henry, G. W., Marcy, G. W., Butler, R. P., & Vogt, S. S. 2000, ApJ, 529, L41

Hershey, J. L. 1973, AJ, 78, 421

Hillenbrand, L. A., Carpenter, J. M., Kim, J. S., et al. 2008, ApJ, 677, 630

Hinz, P. M. 2009, in American Institute of Physics Conference Series, Vol. 1158, American Institute of Physics Conference Series, ed. T. Usuda, M. Tamura, & M. Ishii, 313–317

Holland, W. S., Greaves, J. S., Zuckerman, B., et al. 1998, Nature, 392, 788

Horne, K. 1986, PASP, 98, 609

Howard, A. W., Marcy, G. W., Johnson, J. A., et al. 2010, Science, 330, 653

Howard, A. W., Sanchis-Ojeda, R., Marcy, G. W., et al. 2013, Nature, 503, 381

Howell, S. B., Sobeck, C., Haas, M., et al. 2014, PASP, 126, 398

Hubbard, W. B., Fortney, J. J., Lunine, J. I., et al. 2001, ApJ, 560, 413

Huitson, C. M., Sing, D. K., Pont, F., et al. 2013, MNRAS, 434, 3252

Huitson, C. M., Sing, D. K., Vidal-Madjar, A., et al. 2012, MNRAS, 422, 2477

Husnoo, N., Pont, F., Mazeh, T., et al. 2012, MNRAS, 422, 3151

Jenkins, J. M., Caldwell, D. A., & Borucki, W. J. 2002, ApJ, 564, 495

Jensen, A. G., Redfield, S., Endl, M., et al. 2012, ApJ, 751, 86

Jensen, A. G., Redfield, S., Endl, M., et al. 2011, ApJ, 743, 203

Jewitt, D., Moro-Martìn, A., & Lacerda, P. 2009, The Kuiper Belt and Other Debris Disks, ed. H. A. Thronson, M. Stiavelli, & A. Tielens, 53

Johnson, J. A., Aller, K. M., Howard, A. W., & Crepp, J. R. 2010, PASP, 122, 905

Johnson, J. A., Winn, J. N., Narita, N., et al. 2008, ApJ, 686, 649

Jones, H. R. A., Butler, R. P., Tinney, C. G., et al. 2010, MNRAS, 403, 1703

Jordán, A., Espinoza, N., Rabus, M., et al. 2013, ApJ, 778, 184

Kasting, J. 2010, How to Find a Habitable Planet (Princeton University Press)

Kennedy, G. M. & Wyatt, M. C. 2012, MNRAS, 426, 91

Kennedy, G. M. & Wyatt, M. C. 2013, MNRAS, 433, 2334

Kipping, D. M. 2009, MNRAS, 392, 181

Kipping, D. M. & Tinetti, G. 2010, MNRAS, 407, 2589

Knutson, H. A., Benneke, B., Deming, D., & Homeier, D. 2014a, Nature, 505, 66

Knutson, H. A., Charbonneau, D., Allen, L. E., Burrows, A., & Megeath, S. T. 2008, ApJ, 673, 526

Knutson, H. A., Charbonneau, D., Burrows, A., O'Donovan, F. T., & Mandushev, G. 2009, ApJ, 691, 866

Knutson, H. A., Charbonneau, D., Noyes, R. W., Brown, T. M., & Gilliland, R. L. 2007, ApJ, 655, 564

Knutson, H. A., Fulton, B. J., Montet, B. T., et al. 2014b, ApJ, 785, 126

Knutson, H. A., Howard, A. W., & Isaacson, H. 2010, ApJ, 720, 1569

Koch, D. G., Borucki, W. J., Basri, G., et al. 2010, ApJ, 713, L79

Kovács, G., Hodgkin, S., Sipőcz, B., et al. 2013, MNRAS, 433, 889

Kreidberg, L., Bean, J. L., Désert, J.-M., et al. 2014, Nature, 505, 69

Kuzuhara, M., Tamura, M., Kudo, T., et al. 2013, ApJ, 774, 11

Lagrange, A.-M., Backman, D. E., & Artymowicz, P. 2000, Protostars and Planets IV, 639

Lanza, A. F., Pagano, I., Leto, G., et al. 2009, A&A, 493, 193

Laughlin, G., Crismani, M., & Adams, F. C. 2011, ApJ, 729, L7

Law, N. M., Kraus, A. L., Street, R. R., et al. 2011, ArXiv e-prints

Lecavelier Des Etangs, A., Ehrenreich, D., Vidal-Madjar, A., et al. 2010, A&A, 514, A72

Lecavelier Des Etangs, A., Pont, F., Vidal-Madjar, A., & Sing, D. 2008a, A&A, 481, L83

Lecavelier Des Etangs, A., Vidal-Madjar, A., Désert, J.-M., & Sing, D. 2008b, A&A, 485, 865

Lee, J. W., Youn, J.-H., Kim, S.-L., Lee, C.-U., & Hinse, T. C. 2012, AJ, 143, 95

Lendl, M., Gillon, M., Queloz, D., et al. 2013, A&A, 552, A2

Line, M. R., Knutson, H., Deming, D., Wilkins, A., & Desert, J.-M. 2013, ApJ, 778, 183

Lodders, K. 1999, ApJ, 519, 793

López-Morales, M. 2011, in Highlights of Spanish Astrophysics VI, ed. M. R. Zapatero Osorio, J. Gorgas, J. Maíz Apellániz, J. R. Pardo, & A. Gil de Paz, 60–72

Machalek, P., McCullough, P. R., Burke, C. J., et al. 2008, ApJ, 684, 1427

Machalek, P., McCullough, P. R., Burrows, A., et al. 2009, ApJ, 701, 514

Maciejewski, G., Dimitrov, D., Neuhäuser, R., et al. 2011, MNRAS, 411, 1204

Maciejewski, G., Dimitrov, D., Seeliger, M., et al. 2013, A&A, 551, A108

Madhusudhan, N. 2012, ApJ, 758, 36

Madhusudhan, N., Knutson, H., Fortney, J., & Barman, T. 2014, ArXiv e-prints

Madhusudhan, N., Mousis, O., Johnson, T. V., & Lunine, J. I. 2011, ApJ, 743, 191

Mahtani, D. P., Maxted, P. F. L., Anderson, D. R., et al. 2013, MNRAS, 432, 693

Mancini, L., Ciceri, S., Chen, G., et al. 2013a, MNRAS, 436, 2

Mancini, L., Nikolov, N., Southworth, J., et al. 2013b, MNRAS, 430, 2932

Mancini, L., Southworth, J., Ciceri, S., et al. 2014a, ArXiv e-prints

Mancini, L., Southworth, J., Ciceri, S., et al. 2014b, A&A, 562, A126

Marois, C., Zuckerman, B., Konopacky, Q. M., Macintosh, B., & Barman, T. 2010, Nature, 468, 1080

Mayor, M., Marmier, M., Lovis, C., et al. 2011, ArXiv e-prints

Mayor, M. & Queloz, D. 1995, Nature, 378, 355

McCullough, P. R., Crouzet, N., Deming, D., & Madhusudhan, N. 2014, ApJ, 791, 55

Miller-Ricci, E. & Fortney, J. J. 2010, ApJ, 716, L74

Morton, T. D. & Johnson, J. A. 2011, ApJ, 738, 170

Müller, H. M., Huber, K. F., Czesla, S., Wolter, U., & Schmitt, J. H. M. M. 2013, A&A, 560, A112

Murgas, F., Palle, E., Zapatero Osorio, M. R., et al. 2014, ArXiv e-prints

Narita, N., Suto, Y., Winn, J. N., et al. 2005, PASJ, 57, 471

Nascimbeni, V., Cunial, A., Murabito, S., et al. 2013a, A&A, 549, A30

Nascimbeni, V., Piotto, G., Pagano, I., et al. 2013b, A&A, 559, A32

Nelson, B. & Davis, W. D. 1972, ApJ, 174, 617

Nettelmann, N., Fortney, J. J., Kramm, U., & Redmer, R. 2011, ApJ, 733, 2

Nikolov, N., Chen, G., Fortney, J. J., et al. 2013, A&A, 553, A26

Nikolov, N., Sing, D. K., Pont, F., et al. 2014, MNRAS, 437, 46

Oppenheimer, B. R., Baranec, C., Beichman, C., et al. 2013, ApJ, 768, 24

Patel, R. I., Metchev, S. A., & Heinze, A. 2014, ApJS, 212, 10

Pepe, F., Cameron, A. C., Latham, D. W., et al. 2013, Nature, 503, 377

Petigura, E. A., Howard, A. W., & Marcy, G. W. 2013a, Proceedings of the National Academy of Science, 110, 19273

Petigura, E. A., Marcy, G. W., & Howard, A. W. 2013b, ApJ, 770, 69

Pogge, R. W., Atwood, B., Brewer, D. F., et al. 2010, in Society of Photo-Optical Instrumentation Engineers (SPIE) Conference Series, Vol. 7735, Society of Photo-Optical Instrumentation Engineers (SPIE) Conference Series

Pont, F. 2009, MNRAS, 396, 1789

Pont, F., Knutson, H., Gilliland, R. L., Moutou, C., & Charbonneau, D. 2008, MNRAS, 385, 109

Pont, F., Sing, D. K., Gibson, N. P., et al. 2013, MNRAS, 432, 2917

Pont, F., Zucker, S., & Queloz, D. 2006, MNRAS, 373, 231

Poppenhaeger, K. & Wolk, S. J. 2014, A&A, 565, L1

Popper, D. M. & Etzel, P. B. 1981, AJ, 86, 102

Press, W. H., Teukolsky, S. A., Vetterling, W. T., & Flannery, B. P. 1992, Numerical recipes in FORTRAN. The art of scientific computing

Redfield, S., Endl, M., Cochran, W. D., & Koesterke, L. 2008, ApJ, 673, L87

Reed, B. C. 1998, JRASC, 92, 36

Robertson, P., Endl, M., Cochran, W. D., et al. 2012, ApJ, 749, 39

Rogers, L. A. & Seager, S. 2010, ApJ, 716, 1208

Rowe, J. F., Bryson, S. T., Marcy, G. W., et al. 2014, ApJ, 784, 45

Sada, P. V., Deming, D., Jennings, D. E., et al. 2012, PASP, 124, 212

Sartoretti, P. & Schneider, J. 1999, A&AS, 134, 553

Schneider, J., Dedieu, C., Le Sidaner, P., Savalle, R., & Zolotukhin, I. 2011, A&A, 532, A79

Schwarz, G. 1978, Annals of Statistics, 6, 461

Seager, S. & Deming, D. 2010, ARA&A, 48, 631

Seager, S. & Mallén-Ornelas, G. 2003, ApJ, 585, 1038

Seager, S. & Sasselov, D. D. 1998, ApJ, 502, L157

Seager, S. & Sasselov, D. D. 2000, ApJ, 537, 916

Seeliger, M., Dimitrov, D., Kjurkchieva, D., et al. 2014, MNRAS, 441, 304

Sing, D. K. 2010, A&A, 510, A21

Sing, D. K., Désert, J.-M., Fortney, J. J., et al. 2011a, A&A, 527, A73

Sing, D. K., Désert, J.-M., Lecavelier Des Etangs, A., et al. 2009, A&A, 505, 891

Sing, D. K., Huitson, C. M., Lopez-Morales, M., et al. 2012, MNRAS, 426, 1663

Sing, D. K., Lecavelier des Etangs, A., Fortney, J. J., et al. 2013, ArXiv e-prints

Sing, D. K., Pont, F., Aigrain, S., et al. 2011b, MNRAS, 416, 1443

Sing, D. K., Vidal-Madjar, A., Désert, J.-M., Lecavelier des Etangs, A., & Ballester, G. 2008a, ApJ, 686, 658

Sing, D. K., Vidal-Madjar, A., Lecavelier des Etangs, A., et al. 2008b, ApJ, 686, 667

Smith, B. A. & Terrile, R. J. 1984, Science, 226, 1421

Snellen, I. A. G., Albrecht, S., de Mooij, E. J. W., & Le Poole, R. S. 2008, A&A, 487, 357

Snellen, I. A. G., de Kok, R. J., de Mooij, E. J. W., & Albrecht, S. 2010, Nature, 465, 1049

Southworth, J. 2008, MNRAS, 386, 1644

Southworth, J. 2012, MNRAS, 426, 1291

Southworth, J., Bruni, I., Mancini, L., & Gregorio, J. 2012a, MNRAS, 420, 2580

Southworth, J., Bruntt, H., & Buzasi, D. L. 2007a, A&A, 467, 1215

Southworth, J., Hinse, T. C., Jørgensen, U. G., et al. 2009, MNRAS, 396, 1023

Southworth, J., Mancini, L., Browne, P., et al. 2013, MNRAS, 434, 1300

Southworth, J., Mancini, L., Maxted, P. F. L., et al. 2012b, MNRAS, 422, 3099

Southworth, J., Maxted, P. F. L., & Smalley, B. 2004, MNRAS, 349, 547

Southworth, J., Wheatley, P. J., & Sams, G. 2007b, MNRAS, 379, L11

Spiegel, D. S. & Burrows, A. 2013, ApJ, 772, 76

Spiegel, D. S., Silverio, K., & Burrows, A. 2009, ApJ, 699, 1487

Steffen, J. H., Ragozzine, D., Fabrycky, D. C., et al. 2012, Proceedings of the National Academy of Science, 109, 7982

Stevenson, K. B., Bean, J. L., Seifahrt, A., et al. 2013, ArXiv e-prints

Strassmeier, K. G. 2009, A&A Rev., 17, 251

Strassmeier, K. G., Granzer, T., Weber, M., et al. 2004, Astronomische Nachrichten, 325, 527

Strassmeier, K. G., Woche, M., Ilyin, I., et al. 2008, in Society of Photo-Optical Instrumentation Engineers (SPIE) Conference Series, Vol. 7014, Society of Photo-Optical Instrumentation Engineers (SPIE) Conference Series

Struve, O. 1952, The Observatory, 72, 199

Su, K. Y. L., Rieke, G. H., Stansberry, J. A., et al. 2006, ApJ, 653, 675

Su, K. Y. L., Rieke, G. H., Stapelfeldt, K. R., et al. 2009, ApJ, 705, 314

Sudarsky, D., Burrows, A., & Hubeny, I. 2003, ApJ, 588, 1121

Swain, M. R., Vasisht, G., & Tinetti, G. 2008, Nature, 452, 329

Swain, M. R., Vasisht, G., Tinetti, G., et al. 2009, ApJ, 690, L114

Szabó, R., Szabó, G. M., Dálya, G., et al. 2013, A&A, 553, A17

Teske, J. K., Turner, J. D., Mueller, M., & Griffith, C. A. 2013, MNRAS, 431, 1669

Tinetti, G., Vidal-Madjar, A., Liang, M.-C., et al. 2007, Nature, 448, 169

Todorov, K., Deming, D., Harrington, J., et al. 2010, ApJ, 708, 498

Todorov, K. O., Deming, D., Knutson, H. A., et al. 2013, ApJ, 770, 102

Todorov, K. O., Deming, D., Knutson, H. A., et al. 2012, ApJ, 746, 111

Tregloan-Reed, J., Southworth, J., & Tappert, C. 2013, MNRAS, 428, 3671

Trilling, D. E., Bryden, G., Beichman, C. A., et al. 2008, ApJ, 674, 1086

Udalski, A., Szymanski, M., Kaluzny, J., et al. 1993, MNRAS, 43, 289

van de Kamp, P. 1963, AJ, 68, 515

van de Kamp, P. 1969, AJ, 74, 238

van de Kamp, P. 1982, Vistas in Astronomy, 26, 141

van Hamme, W. 1993, AJ, 106, 2096

Vidal-Madjar, A., Lecavelier des Etangs, A., Désert, J.-M., et al. 2003, Nature, 422, 143

Vidal-Madjar, A., Sing, D. K., Lecavelier Des Etangs, A., et al. 2011, A&A, 527, A110

von Essen, C., Schröter, S., Agol, E., & Schmitt, J. H. M. M. 2013, A&A, 555, A92

Walkowicz, L. M. & Basri, G. S. 2013, MNRAS

Weber, M., Granzer, T., & Strassmeier, K. G. 2012, in Society of Photo-Optical Instrumentation Engineers (SPIE) Conference Series, Vol. 8451, Society of Photo-Optical Instrumentation Engineers (SPIE) Conference Series

Winn, J. N. 2010, ArXiv e-prints

Winn, J. N., Holman, M. J., Torres, G., et al. 2008, ApJ, 683, 1076

Woitke, P. & Helling, C. 2003, A&A, 399, 297

Wolszczan, A. & Frail, D. A. 1992, Nature, 355, 145

Wood, P. L., Maxted, P. F. L., Smalley, B., & Iro, N. 2011, MNRAS, 412, 2376

Wright, J. T., Marcy, G. W., Butler, R. P., et al. 2008, ApJ, 683, L63

Wu, Y. & Murray, N. 2003, ApJ, 589, 605

Zhou, G., Bayliss, D., Penev, K., et al. 2014, AJ, 147, 144

Zhou, G. & Bayliss, D. D. R. 2012, MNRAS, 426, 2483

Acknowledgements

I want to thank Klaus Strassmeier for providing me the opportunity to work on the fascinating topic of exoplanets, for giving me advice, freedom to develop my own thoughts and financial support for conferences, workshops and observing campaigns.

I am grateful for the support, advice and helpful discussions of all members of the stellar activity group with special thanks to Jörg Weingrill, Thorsten Carroll and Michael Weber. I am immensely grateful to my colleague and friend Andreas Künstler, with whom I could share all the joys and troubles of being a PhD student.

I thank Thomas Granzer and Klaus Strassmeier for granting me spontaneous and extensive access to the STELLA telescope, which helped my science projects a lot! I am grateful to all the instrument teams for the technical support I received at the numerous observatories. Special thanks goes to Thomas Granzer for STELLA support and Olga Kuhn and David Thompson for endless email discussions about the preparation of LBT observations. I thank Barry Rothberg for the successful performance of observations at the LBT.

I thank all my colleagues outside my own institution who worked with me on these fascinating projects. Special thanks goes to Carolina von Essen, Valerio Nascimbeni, Johanna Teske, Enrique Herrero, Ignasi Ribas, Juan Cabrera and Petr Kabath, I learned a lot from you!

And finally, deepest thanks goes to my family, my wife and my kids. You always showed me on which planet in the Universe I can find my home.